INTRAMOLECULAR INHIBITION OF THE PTB DOMAIN IN THE AIDA1 NEURONAL SCAFFOLDING PROTEIN

by
TANVIR CHAKKAL

A THESIS SUBMITTED TO THE FACULTY OF GRADUATE STUDIES IN PARTIAL FULFILLMENT OF THE REQUIREMENTS
FOR THE DEGREE OF
MASTER OF SCIENCE
GRADUATE PROGRAM IN BIOLOGY
YORK UNIVERSITY
TORONTO, ONTARIO
JULY 2023

ABSTRACT

Scaffolding proteins serve key functions in signalling cascades through mediating protein-protein interactions. A prominent member of the neuronal post-synaptic density is AIDA1, which is known to bind amyloid precursor protein (APP), a contributor to Alzheimer's Disease (AD) development. Among the isoforms of AIDA1, AIDA1b is the largest and is unique in that its phosphotyrosine binding (PTB) domain is autoinhibited; thus, it cannot bind APP until this inhibition is relieved. This thesis presents structural and functional studies on AIDA1b. Fluorescence anisotropy and biolayer interferometry assays confirmed that the deletion of Exon 14 relieves the autoinhibition of the PTB domain, allowing AIDA1b to bind APP. However, Exon 14's removal does not significantly impact the thermostability of AIDA1b. Moreover, Exon 14 contributes an alpha helical structural, with 3D bead models exhibiting potential domain reorganization upon Exon 14's removal. The predicted structure of Exon 14 is an amphipathic alpha helix that presumably contacts the PTB domain in cooperation with other intervening sequences. Overall, AIDA1b can play a potential role in AD pathogenesis, with potential for contribution to novel therapeutic development.

DEDICATION

I would like to dedicate this thesis to

My late grandmother, Mohinder Kaur Chakkal

Though you won't be able to read this, you exist in every word

ACKNOWLEDGMENTS

There are countless people for whom I am grateful for throughout the journey of my Master's – without you, I would not be where I am today.

Firstly, I would like to thank my supervisor, Dr. Logan Donaldson, for giving me the opportunity to join his lab and conduct research that has culminated in this thesis. I have the utmost gratitude for your mentorship, and for inspiring me to always strive for excellence. My committee member, Dr. Yi Sheng, your positive feedback, support, and kindness is something I will remember for the duration of my future career – wherever I go. Thank you to Dr. Georg Zoidl and Dr. Philip Johnson for readily joining my defense committee and helping me conclude two years of work.

There are also countless labs, colleagues, and friends whom I would like to thank for their collaboration, discussions, patient teaching, and encouragement – Dr. Gerald Audette, Nick, Alice, Emily, Meghan, Angelo, Gaby, Saptarshi, Farnaz, Cristina, Esther, Vimanda, Riya, Fatema, Sarah, Christiane, Mazda and Tavawn.

I would also like to specially appreciate some of my most cherished friends. Alessia and Arnold – your spontaneity, amiability, everlasting support, and laughs have given me invaluable memories – for that, I will always be grateful. Our friendship has allowed me to flourish and grow, I will dearly miss your daily presence by my side. Christina – whom I consider my lab mother, thank you for all the fun times we had and for giving me reality checks when I was beginning to lose track. For my oldest friends, Khushman, Amarjot, Jassy, and Sandeep – our decade of friendship means the world to me.

To my parents and grandfather – thank you for your support which allowed me to pursue my dreams; I am unable to put my gratitude and love into words for your sacrifice. Your dedication, work ethic, and perseverance as immigrants allowed me to succeed as a first-generation bachelor's graduate, master's graduate, and future medical doctor. To my younger brother – raising you has been one of the hardest, yet most rewarding parts of my life. Thank you for always being my unwavering pillar of support, you bring me joy like no other.

I am so grateful for each and every one of you, your contribution to this thesis cannot be overstated.

TABLE OF CONTENTS

LIST OF FIGURES

LIST OF TABLES

LIST OF ABBREVIATIONS

Abbreviation	Definition
ε	Molar absorption coefficient
5-HT2A	5-hydroxytryptamine
aa	Amino acid
Aβ	Beta-amyloid
AβPP	Amyloid-β Protein Precursor
AD	Alzheimer's disease
AIDA1	Amyloid-ß protein precursor intracellular domain-associated protein-1
AICD	APP Intracellular Domain
Amp	Ampicillin
ANK	Ankryin
ANKS1B	Ankyrin Repeat and Sterile Alpha Motif Domain Containing 1B
APP	Amyloid precursor protein
AR	Ankryin Repeat
ARR	Ankryin Repeat Region
ASD	Austism Spectrum Disorder
BLI	Biolayer Interferometry
Bp	Base pairs
BSA	Bovine Serum Albumin
ccRCC	Clear cell renal cell carcinoma
CD	Circular Dichroism
CNS	Central Nervous System
Da	Dalton
Dab	Disabled
DNA	Deoxyribonucleic acid
D_{max}	Determination of protein radius
DSC	Differential Scanning Calorimetry
DSF	Differential Scanning Fluorimetry
EL	End-loop
EM	Electron Microscopy
EtBr	Ethidium Bromide
FA	Fluorescence Anisotropy
FPLC	Fast Protein Liquid Chromatography
GE	General Electric
GK	Guanylate Kinase
Glu	Glutamate
GST	Glutathione-S-Transferase
GTP	Guanosine triphosphate
HEPES	4-(2-hydroxyethyl)-1- piperazineethanesulfonic acid
IDT	Integrated DNA Technologies
Imid	Imidazole
IMAC	Immobilized metal-affinity chromatography
IPTG	Isopropyl-β-D-thiogalactoside
IRS	Insulin receptor substrate-1

ITC	Isothermal Titration Calorimetry
Km	Kanamycin
LB	Luria Bertani
LTP	Long-term Potentiation
MAGUK	Membrane-associated Guanylate Kinase
MALS	Multi-Angle Light Scattering
MES	2-ethanesulfonic acid
mGLUR	Metabotropic glutamate receptors
ML	Mid-loop
MOPS	3-(N-morpholino)propanesulfonic acid
MS	Mass Spectrometry
MWCO	Molecular Weight Cut-Off
NEB	New England Biolabs
NLS	Nuclear Localization Sequence
NMDAR	N-methyl D-aspartate Receptor
NMR	Nuclear Magnetic Resonance
OD	Optical Density
ORF	Open Reading Frame
PAGE	Polyacrylamide gel electrophoresis
PBS	Phosphate Buffered Saline
PBD	Polypeptide Binding Domain
PCR	Polymerase Chain Reaction
PD	Parkinson's Disease
PDB	Protein Databank
PDZ	PSD-95/Discs-large/Zona Occluden
PH	Pleckstrin Homology
PI	Isoelectric point
PKD	Polycystic Kidney Disease
PMSF	Phenylmethylsulfonyl fluoride
PPI	Prepulse Inhibition
PSD	Post-synaptic Density
PSD-95	Post-synaptic Density Protein 95
PTB	Phosphotyrosine Binding Domain
PTP	Protein Tyrosine Phosphatase Domain
R_g	Radius of gyration
RNA	Ribonucleic acid
Rpm	Rotations per minute
SAM	Sterile Alpha Motif
SAXS	Small-Angle X-ray Scattering
SDS	Sodium Dodecyl Sulfate
SEC	Size Exclusion Chromatography
SH2	Src Homology-2
SH3	Src Homology-3
SPR	Surface Plasma Resonance
Tm	Melting Temperature

Tris	Tris(hydroxymethyl)aminomethane
UV	Ultraviolet

CHAPTER 1: INTRODUCTION

1.1 The Post-Synaptic Density

1.1.1 An Introduction to the PSD

Neurons send and receive signals through electrical or chemical events across a specialized junction called a synapse (Boeckers, 2006). Synapses are formed using dendrites on the pre-synaptic axon terminal spines with post-synaptic dendritic spines (Kennedy, 2000). These protrusions in neurons allow for the release of chemical messengers, such as neurotransmitters, that are uptaken by the post-synaptic neuron and later processed (Sheng & Kim, 2011). A majority of the processing and downstream transduction is completed at a thickened intracellular portion of the post-synaptic dendritic membrane called the post-synaptic density (PSD) (Kennedy, 2000).

1.1.2 PSD Structure

The PSD can be separated into two main regions: PSD core and PSD pallium (Dosemeci et al., 2016). The PSD core briefly extends from the post-synaptic membrane to include transmembrane proteins and their associated partners for signal processing (Dosemeci et al., 2016). On the other hand, the dynamic PSD pallium has a functional role in downstream signalling with changeable protein composition depending on the acquired signal (Dosemeci et al., 2016). Morphological changes in this region include an increase in electron density upon activation of scaffolding proteins and excitatory receptors, visualized using electron microscopy (Dosemeci et al., 2001).

1.1.3 Protein Composition of the PSD

Expanding on the PSD core and pallium, these regions contain a variety of essential proteins for neuronal signalling and processing, with various cellular implications. Cytoskeletal actin appears to be a major component of PSD fractions, followed by kinases/phosphatases, and GTPases (Peng et al., 2004). This data would suggest that the PSD is largely involved in signal receival, processing, and downstream transduction, most notably applicable to receptors that exist in an on/off configuration. Other quantified protein classifications include cell adhesion proteins, receptors/channels, scaffolders, translators, trafficking proteins, chaperones, and mitochondrial proteins (Peng et al., 2004).

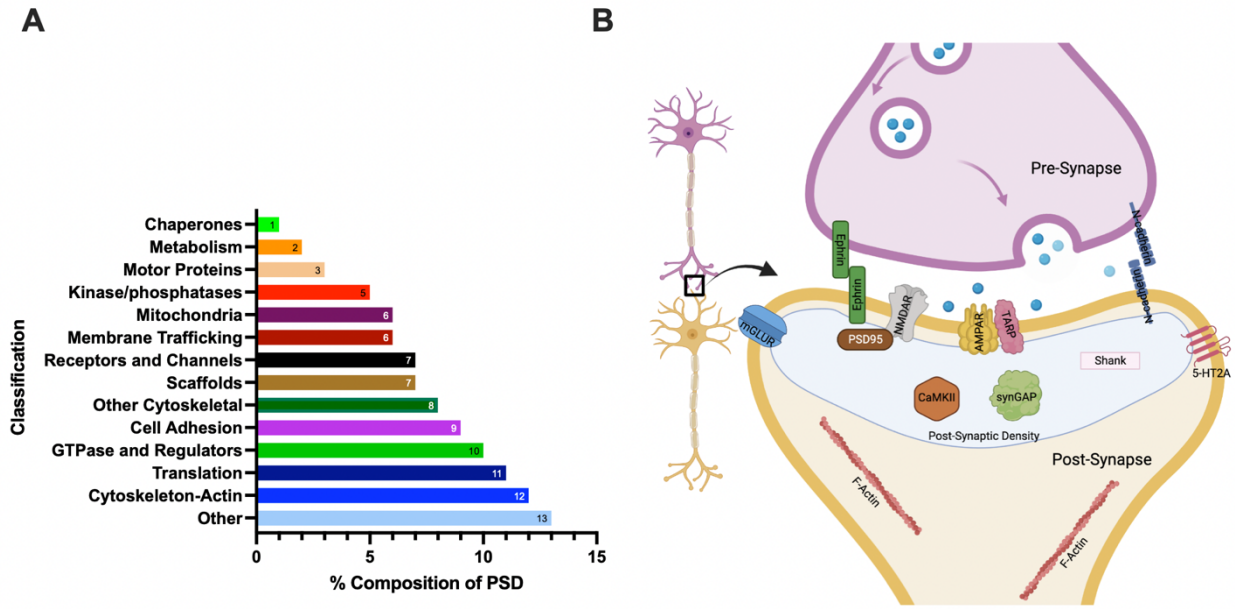

Figure 1.1. Protein Composition of the PSD. Classification of proteins found in the PSD of forebrains. Data from (Peng et al., 2004). (B) Visual representation of proteins found in the PSD of glutaminergic synapses. Key proteins include NMDAR, AMPAR, TARP, synGAP, Shank, CaMKII, 5-HT2A, PSD95, Ephrin, and mGLUR (Feng & Zhang, 2009). Figure created using BioRender.

1.2 Alzheimer's Disease

1.2.1 An Introduction to Alzheimer's Disease

Alzheimer's disease (AD) is a neurodegenerative condition that accounts for approximately 80% of global dementia cases (McGirr et al., 2020). The characteristic clinical presentation includes gradual motor cognitive decline, such as poor decision making and emotional instability, with impairment of working and long-term (i.e. episodic) memory (Blennow et al., 2006; McGirr et al., 2020). With a prognosis of approximately 8 years, the disease gradually progresses from short-term memory dysfunction to psychosis, eating disorders and apathy to name a few symptoms (Golde, 2022).

The pathophysiological characterization of AD includes plaques and neurofibrillary tangles due to the accumulation of amyloid-beta peptide's (Aβ) (Breijyeh & Karaman, 2020). This commonly occurs in the medial temporal lobe and neocortical structures which are responsible for cognition, learning, and memory (Querfurth & LaFerla, 2010). The physiological structure of an Alzheimer's diseased brain often shows enlarged ventricles with shrinkage of the hippocampus and cerebral cortex, regions that are responsible for higher cognitive function (Breijyeh & Karaman, 2020).

Since the exact cause of AD development is unknown, there are several hypotheses presented by literature based on modern research. This includes the amyloid hypothesis, cholinergic hypothesis, Tau propagation hypothesis, mitochondrial cascade hypothesis, and the neurovascular hypothesis (Liu et al., 2019). The cholinergic hypothesis focuses on the reduced acetylcholine uptake by aged neurons, whereas the mitochondrial cascade hypothesis discusses mitochondrial dysfunction (Liu et al., 2019). On the other hand, the neurovascular hypothesis presents blood brain barrier breakdown as the potential cause for toxic molecule buildup in AD

(Liu et al., 2019). Important to this thesis, is the amyloid precursor hypothesis of AD, which will be discussed below.

1.2.2 The Amyloid Precursor Protein

Amyloid precursor protein (APP) is a single-pass transmembrane protein present in mammals. Although the exact function of APP is unknown, research has shown it plays a role in cell growth, survival, motility and transcription regulation based on the extracellular or intracellular peptide post-cleavage (Oh et al., 2009).

In a healthy brain, APP is cleaved by α-secretase into a extracellular C-terminal fragment called sAPPα and a membrane-bound N-terminal fragment called C83 (Nunan & Small, 2000). The C83 refers to the fact that the peptide is composed of 83 residues (Nunan & Small, 2000). The membrane-bound peptide is then futher cleaved to an extracellular peptide called p3, and an intracellular portion called APP intracellular domain (AICD) by γ-secretase (Nunan & Small, 2000).

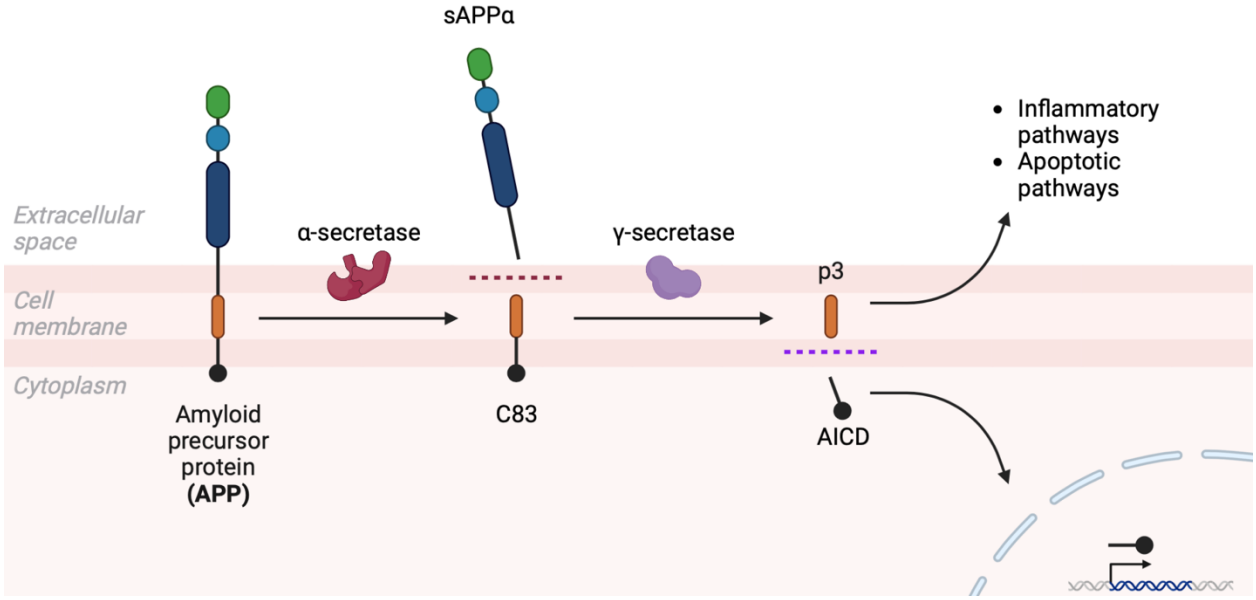

Figure 1.2 Non-amyloidogenic pathway processing of amyloid precursor protein. Amyloid precursor protein is cleaved to C83 and sAPPα by α-secretase, after which C83 is further cleaved by γ-secretase to p3, which moves to the extracellular space, and AICD, which translocates to the nucleus. Figure adapted from (Biorender, 2022) and created using BioRender.

Specifically, recent studies found that injections of ectodermal APP improved synaptic plasticity, rescued neuronal migration, and improved cognitive function (Young-Pearse et al., 2007). However, the loss of extracellular APP (sAPPα), studied through deletions in mice, was not deterimental to their survivability (Herms et al., 2004). On the other hand, the AICD peptide translocates to the nucleus, where it functions as a transcriptional regulator and protein binder. Firstly, as a transcriptional regualtor, AICD is known to regulate genes like *LRP1*, *KAI1*, *GSK-3β*, *neprilysin* and *EGFR* which are predicted to be involved in tumorigenesis, glycogen metabolism and protein synthesis (Shu et al., 2015). As a protein binder, the YENPTY motif in AICD can bind a variety of proteins, by which it can regulate its own metabolism (O'Brien & Wong, 2011).

1.2.3 Amyloid Precursor Protein Structure

The *APP* gene has 19 exons that are transcribed into a protein of up to 770 amino acids, which is yet to be structurally solved (Gralle & Ferreira, 2007). As mentioned above, the AICD domain is vital for protein-protein interactions, and has been crystallized in complex with a number of protein partners, such as Fe65 (Radzimanowski et al., 2008). The N-terminal end begins with an E1 domain, that could possibly be involved in metal, ligand, or protein binding (Dawkins & Small, 2014). After a disordered region, the KPI domain has shown to have protease inhibitor activity (Dawkins & Small, 2014). Next, the E2 domain is also predicted to partake in protein-protein binding and heparin binding (Dawkins & Small, 2014). The transmembrane domain (TMD), is associated with dimerization and lipid binding (Barrett et al., 2012). Lastly, the intracellular domain plays a role in intracellular signalling and transcriptional regulation (Kerr & Small, 2005).

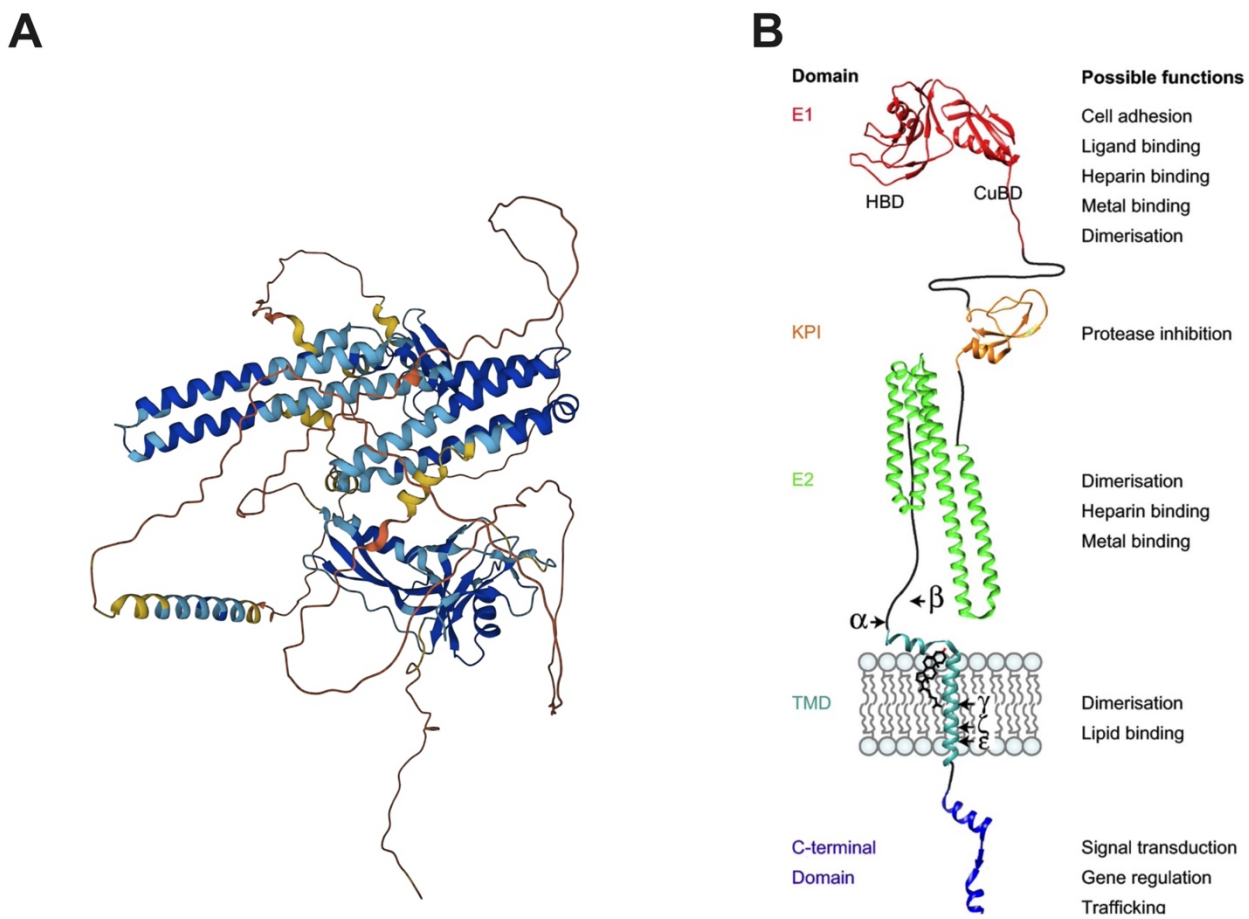

Figure 1.3 Predicted structure and functional characterization of amyloid precursor protein. (A) AlphaFold prediction of APP structure. Confidence: dark blue = very high (pLDDT > 90), light blue = confident (90> pLDDT > 70), yellow = low (70> pLDDT > 50), orange = very low(pLDDT < 50) (Jumper et al., 2021; Varadi et al., 2022). **(B)** Predicted functional characterization of APP domains: E1 domain (PDB: 3KTM), Kunitz protease inhibitor (KPI) domain (PDB: 1ZJD), E2 domain (PDB: 3UMK), transmembrane domain (TMD) (PDB: 2LLM) and intracellular domain (PDB: 3DXC). A cholesterol molecule, in black, is shown in the TMD. Figure adapted from (Dawkins & Small, 2014) and created in GraphPad PRISM.

1.2.4 Amyloid Hypothesis of Alzheimer's Disease

The foundation of the amyloid hypothesis of AD is that the deposition of amyloid plaques from Aβ peptide cleavage negatively impacts higher cognitive function due to their neurotoxicity (Liu et al., 2019). In an Alzheimer's diseased brain, there is abnormal cleavage of APP, which leads to the deposition of amyloid plaques. This is because, a β-secretase called β-site APP

Cleaving Enzyme (BACE1), competes with α-secretase for APP as a substrate (MacLeod et al., 2015). As a result, the overactivity of BACE1 leads to the abnormal cleavage of APP into sAPPβ and C99 (MacLeod et al., 2015). Although transmembrane C99 can be further cleaved to AICD by γ-secretase, the remaining portion is classified as Aβ40/42 based on the number of residues (MacLeod et al., 2015) by. The overproduction of Aβ40/42 leads to their crosslinking, which eventual forms fibril tangles that are neurotoxic (Bitan et al., 2003). The abnormal hyperactivity of BACE1 is predicted to be due to APP mutations, whereas hyperactivity of the γ-secretase complex is due to mutations in a vital genes *PSEN1* and *PSEN2*, required for protease activity (De Strooper et al., 2012).

The amyloid plaques can block signalling at neuronal synapses, cause an inflammatory immune response, neuronal breakdown which leads to brain region shrinkage (Nunan & Small, 2000).

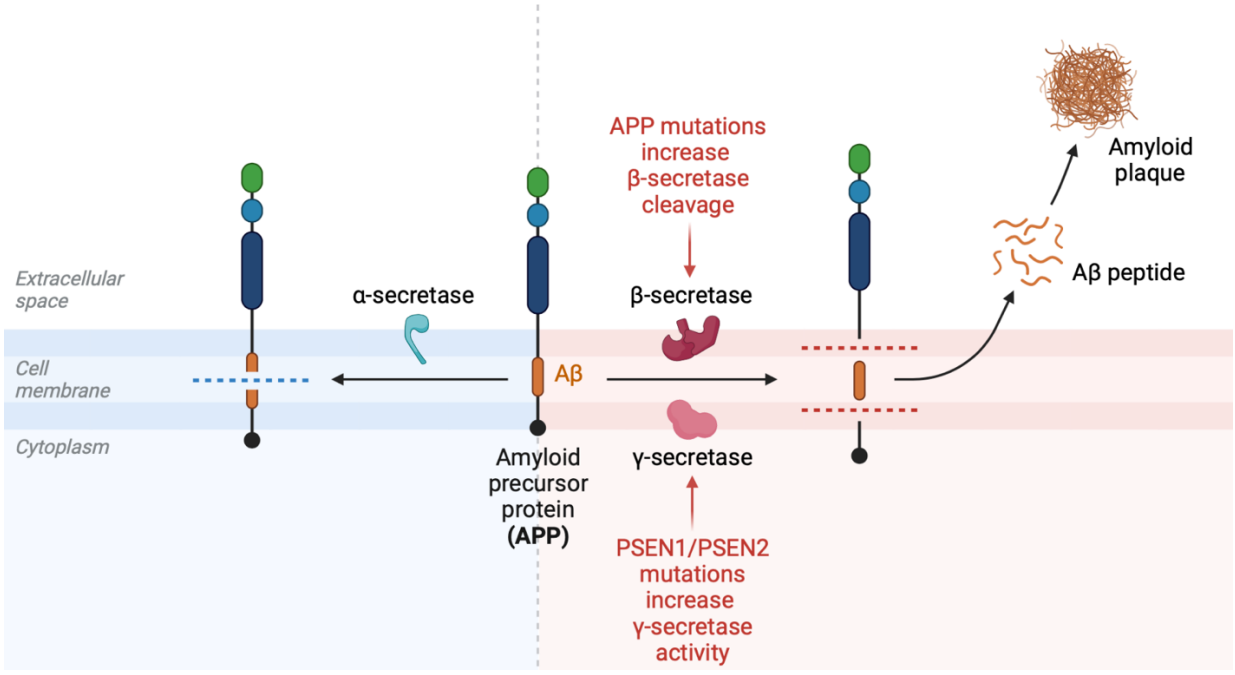

Figure 1.4. Cleavage of APP in normal and diseased patients. The left panel displays normal cleave of APP with α-secretase. The intracellular portion is C83 and the extracellular portion is aAPPα. The right panel displays abnormal cleave of APP due to PSEN1/PSEN2 and APP mutations that increase β- and γ-secretase activity to deposit amyloid plaques formed of Aβ

peptides. The intracellular black peptide is AICD, the transmembrane orange peptide is A β40/42, and the extracellular region is sAPPβ. Figured adapted from (BioRender, 2022) and created using BioRender.

1.3 AIDA1

1.3.1 The ANKS1B gene

The Ankyrin Repeat and Sterile Alpha Motif Domain-containing 1B (ANKS1B) gene is typically found expressed in the CNS (Sayers et al., 2022). Located on chromosome 12, its specific cytogenic band is 12q23.1 with 29 exons (Stelzer et al., 2016). It is approximately 1.2 megabases (Mb) and oriented in the "minus" or "antisense" orientation (Stelzer et al., 2016). This gene encodes for a multidomain protein, AIDA1 (or ANKS1B protein), that is predicted to play a role in the implication of several human diseases. The *ANKS1B* gene is conserved across homosapiens, zebrafish, rat, Rhesus monkey, chicken dog, and mouse (Sayers et al., 2022). Specifically, there are 464 orthologs found for the ANKS1B gene in human (Sayers et al., 2022).

1.3.2 The neuronal scaffolder – AIDA1

Amyloid-β Protein Precursor (AβPP) Intracellular Domain-associated Protein-1 (AIDA1) is a member of the PSD in excitatory neurons. Encoded by the ANKS1B gene, as mentioned above, it is composed of 1248 residues in human. It was originally discovered as a novel interactor of APP using a yeast two-hybrid assay (Ghersi et al., 2004).

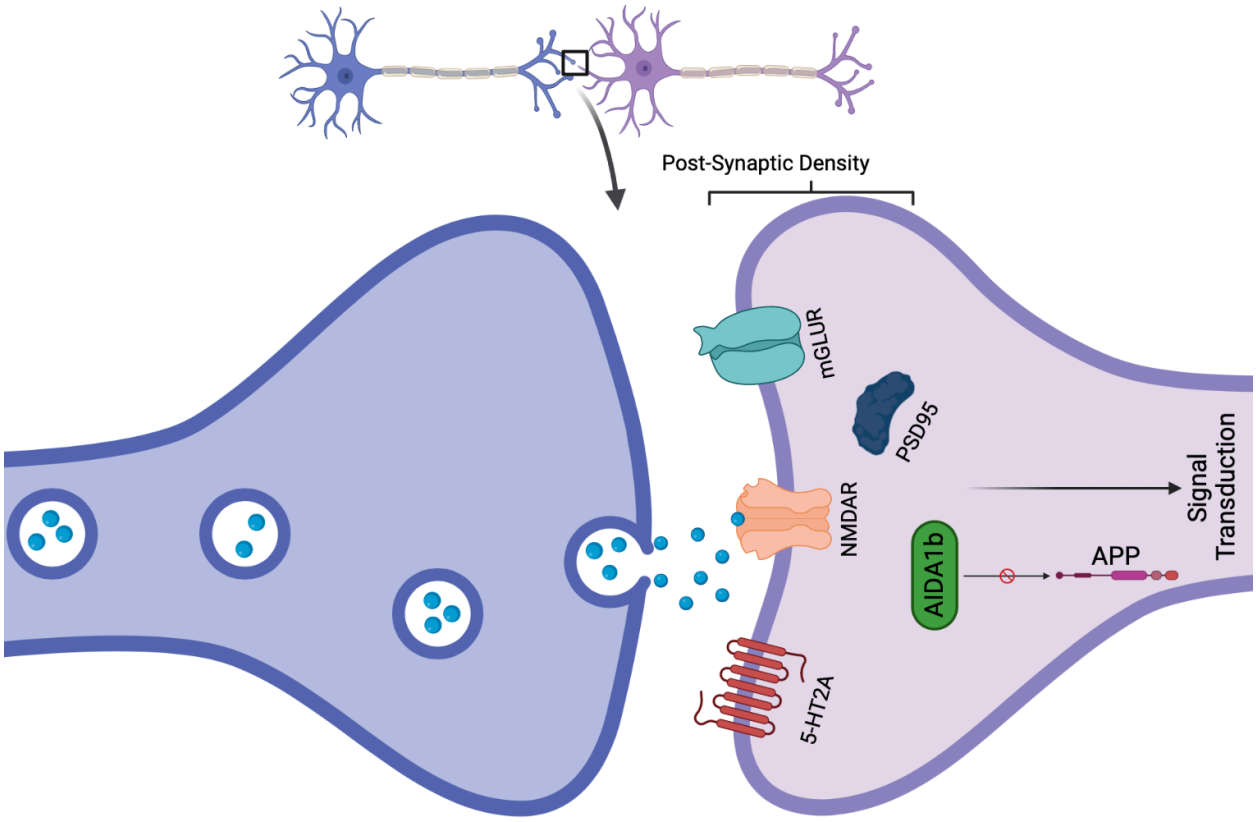

Figure 1.5. PSD of glutaminergic neurons with AIDA1b and binding partners. The molecular organization of PSDs only with proven binding partners of AIDA1b. AIDA1b has shown not to bind APP, however, interactions with mGLUR, NMDAR, 5-HT2A or PSD95 has shown to have downstream signalling effects. Figure created using BioRender.

1.4 AIDA1 Structure

1.4.1 Overview of AIDA1 Structure

There are five different isoforms, due to alternative splicing, for AIDA1: AIDA1a, AIDA1b, AIDA1c, AIDA1d, and AIDA1e. The smallest isoform is AIDA1c, composed of 426 residues and a molecular weight of 48kDa. The next largest isoforms are AIDA1a/d/e with identical structural characteristics. They are composed of 460 residues, with a molecular weight of 52kDa. All four isoforms have 2 SAM domains (SAM1, SAM2) at the N-terminus and a PTB domain close to the C-terminus (Kurabi et al., 2009). The largest isoform would be AIDA1b, at 1248 residues with a molecular weight of 138kDa. While this protein also has the 2 SAM

domains and PTB domain, it also has an ARR at the N-terminus, compose of six ARs. Due to its relevance to this thesis, AIDA1b will be further discussed.

The AlphaFold prediction of AIDA1b shows a globular protein, with several disordered linker regions between the structurally solved domains. The ARR is predicted to play a role in protein-protein interactions, however, there is little research done on this region. On the contrary, the structure of the 2 SAM domains and PTB domain has been solved by the Donaldson lab using NMR methods (Kurabi et al., 2009; Smirnova et al., 2013).

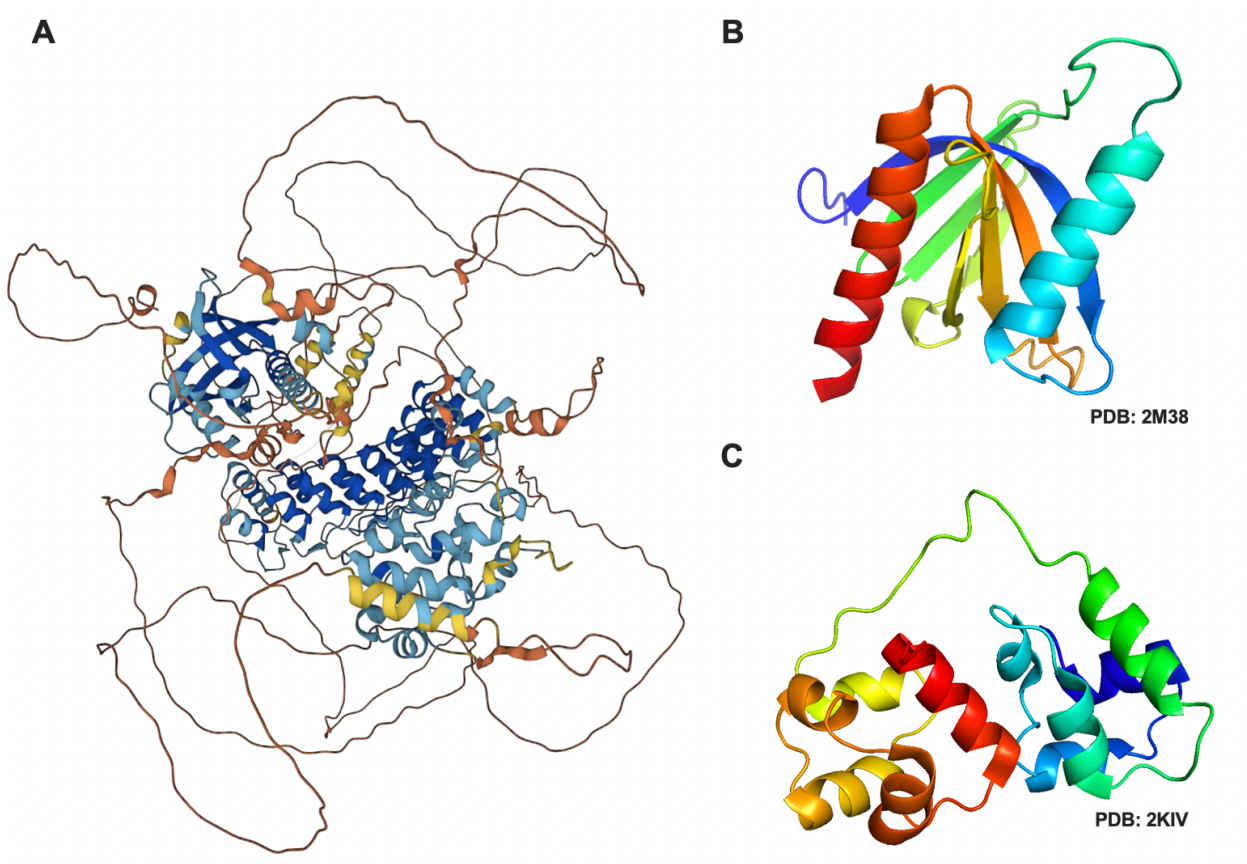

Figure 1.6. Predicted and solution structures of AIDA1b and internal domains. (A) AlphaFold prediction of AIDA1b structure. Confidence: dark blue = very high (pLDDT > 90), light blue = confident (90> pLDDT > 70), yellow = low (70> pLDDT > 50), orange = very low(pLDDT < 50) (Jumper et al., 2021; Varadi et al., 2022). **(B)** NMR solution structure of PTB domain in AIDA1b, displayed using pyMOL with colour scheme rainbow (C-terminal to N-terminal) (PDB: 2M38) (Smirnova et al., 2013). **(C)** NMR solution structure of SAM1SAM2 domain tandem, displayed using pyMOL with colour scheme rainbow (C-terminal to N-terminal) (PDB: 2KIV) (Kurabi et al., 2009).

1.4.2 The ARR Domain

Ankyrin repeat regions (ARR) are a specific classification of amino acid motifs composed of the 30-34 residue ankyrin repeats (ARs) (Breeden & Nasmyth, 1987). In most proteins, ARs are repeated four to six times, varying across all three kingdoms – bacteria, archaea and eukarya (Mosavi et al., 2004). Each repeat starts with a β-turn, two anti-parallel alpha-helices, and a loop that connects to the next AR (Gorina & Pavletich, 1996). The stacked loops then form a right-handed coil structure, with a hydrophobic core and hydrophilic surface that aids in protein-protein interactions (Kobe & Kajava, 2000). As the number of ARs increases, the overall structure becomes more compact and concave (Michaely, 2002; Mosavi et al., 2004). This happens due to the consecutive 2-3° clockwise turn following each AR (Michaely, 2002; Mosavi et al., 2004). A β-turn is held together by 5 hydrogen bonds, followed by a TPLH motif that initiates the first alpha-helix (Sedgwick & Smerdon, 1999). Overall, the structure resembles a hairpin: a helix-turn-helix conformation, where the turn is 90° (Li et al., 2006). The helices are then terminated by G_{13} and G_{25} which allows for loop formation (Sedgwick & Smerdon, 1999). Terminal or "capping" ARRs protect the hydrophobic regions from solvent exposure by specialized folding at the C- or N-terminus (Forrer et al., 2004). Folding studies of various ARR-containing proteins has shown a two-state transition between folded and unfolded states (Zeeb et al., 2002; Zweifel & Barrick, 2001).

1.4.3 The SAM Domains.

SAMs display wide diversity in subcellular localization, function, and binding partners. However, the general consensus structure is approximately five alpha helices (Kim, 2003). Since they have such diverse properties, it is difficult to pinpoint the function of a SAM domain in a

multidomain structure, rather it provides a list of possible functions. Composed of approximately 70-80 residues, they can exhibit a wide array of oligomeric forms, such as heteropolymers or closed oligomers (Knight et al., 2011). These polymers are known to be left-handed structures, with each subunit connected using Mid-Loop (ML) and End-Helix (EH) surfaces (Meruelo & Bowie, 2009). Structural studies have shown each domain to be composed of five or six alpha helices involved in self-association, SAM-SAM binding, and forming complexes with non-SAM containing proteins (Thanos et al., 1999).

In AIDA1, the structures of the SAM1 domain and the SAM1SAM2 domain tandem has been solved. There are two basic sequences in AIDA1 that could act as nuclear localization sequences (NLS). The first is located in α5-helix of SAM2, HKRK, whereby its deletion results in impaired nuclear importation for the protein (Jordan et al., 2007). The second is RRRR, which is located on exon 19, and its mutation resulted in constant nuclear localization (Kurabi et al., 2009). Next, after looking at the thermal stability of SAM1 and SAM2, it was predicted that SAM1 is the more stable partner. This is because CD studies revealed SAM2 was highly unstable without SAM1, and prone to aggregation (Kurabi et al., 2009). Furthermore, the stable nature of SAM1 also supports the theory that SAM1 is preconfigured to accept SAM2 into a complex. Overall, these two SAM domains likely play a role in the nuclear import and binding interactions to small molecules for the AIDA1 isoforms.

1.4.4 The PTB Domain.

Although PTB domain functions vary, they are most commonly implicated in cell-cell adhesion, immune response, cellular growth and signalling network organization (Uhlik et al., 2005). PTB domains can be classified into three categories: Shc-like, IRS-like, and Dab-like

based on their structure and function (Smith et al., 2006). Shc-like and IRS-like domains act in a phosphorylation-dependent manner, although the latter is specifically for insulin receptor substrates (Uhlik et al., 2005). On the other hand, Dab-like domains account for a majority of PTB domains, which bind targets in a phosphoindependent manner (Uhlik et al., 2005). The general consensus structure across all three classifications is referred to as a "superfold": two β-sheets in orthogonal "sandwich" against two α-helices (Li et al., 1998). This superfold is representative of the pleckstrin-homology (PH) domain, however, there is little genetic similarity between both (Uhlik et al., 2005). Unique to Shc- and Dab-like domains is an additional C-terminal α-helix, whereas IRS-like have a truncated α2-helix instead (Yun et al., 2003; Zhou et al., 1996). There is also a binding pocket formed by β5-strand and C-terminal α-helix, and an N-terminal lipid binding site that is highly basic (Dinitto & Lambright, 2006). In terms of size, on average these domains range from 100-170 residues long (Yan et al., 2002).

PTB domains are known to bind a canonical sequence of NPXY (X = any amino acid), where the tyrosine is phosphorylated or not based on domain classification (Smith et al., 2006). Dab-like domains can also bind a sequence of NPXF, where the tyrosine is replaced by a phenylalanine (Wagner et al., 2013). Ligand docking usually occurs with N-terminal residues that form a β-strand and β-turn, however, the specific mechanism can differ between each class (Kaneko et al., 2012). Phospholipid binding has been shown by X11, IRS-1, Shc, Dab1, Dab2, Numb and Talin proteins (Uhlik et al., 2005).

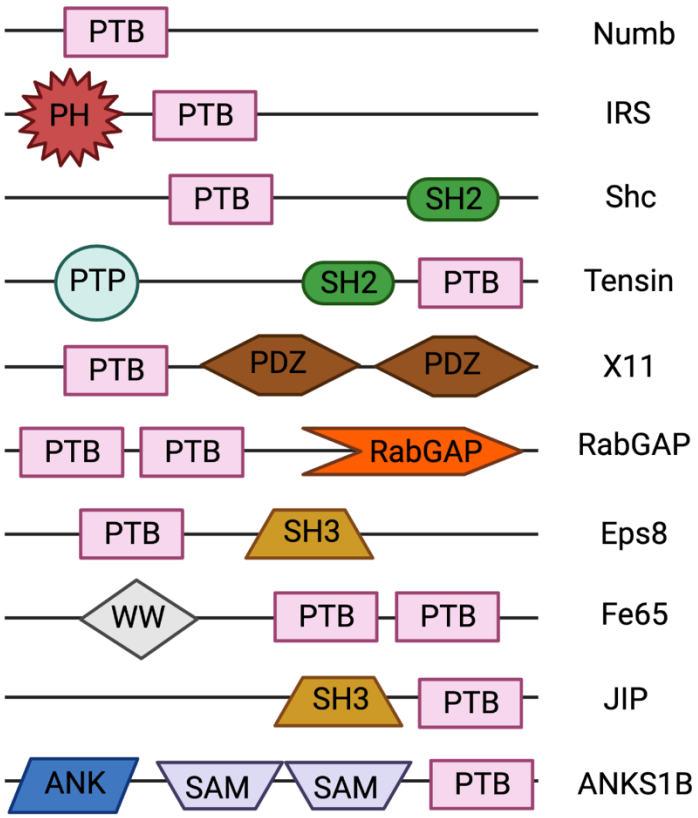

Figure 1.7. Structural characterization of PTB domain containing proteins. The name of each respective protein is listed beside the domain architecture. Domain annotations are as follows: PH - pleckstrin homology domain; SH2 - Src homology 2 domain; PTP - protein tyrosine phosphatase domain; PDZ - PSD-95/discs large/ZO-1 domain; SH3 - Src homology 3 domain; WW - domain with two conserved tryptophans; ANK - ankyrin repeat domain; SAM - sterile alpha motif. Figured created using BioRender and adapted from (Uhlik et al., 2005).

This 153 amino acid domain in AIDA1b has been solved by NMR methods (PDB: 2M38). While the wild-type domain is unstable and prone to aggregation, substitution of surface-exposed aromatic residues greatly improved its solubility (Smirnova et al., 2013). The AIDA1 PTB domain belongs to the Dab-like family, where it binds to targets in a phospho-independent manner (Smirnova et al., 2013). Moreover, a well-known binding partner of the PTB domain is APP, which is discussed further below.

1.4 Implications of ANKS1B and AIDA1 Mutation and Dysfunction

Monogenic deletions in *ANKS1B* led to the development of a disorder that was characteristic of ASD. A mouse model had characteristics of intellectual disability, motor dysfunction and social deficiencies (Carbonell et al., 2019). A genomic interaction analysis of AIDA1 showed that it is involved in synaptic signalling pathways and pathways commonly attributed to neurodevelopmental diseases (Carbonell et al., 2019).

An AIDA1 knock out (KO) is partially lethal in newborn mice. AIDA1 KO mice also displayed prepulse inhibition (PPI) deficits and stereotypy, which refers to constant repetition of a specific action (Enga et al., 2017). This shows that the *ANKS1B* gene is partly implicated in pathways that are responsible for the startle response. Lastly, treatment with an NMDAR antagonist showed altered response, such that it aggravated motor activity in comparison to the control (Enga et al., 2017). Again, this implicates the *ANKS1B* gene in motor pathways. These symptoms shown in murine models are also representative of schizophrenia, another possible relation to human disease for the AIDA1/*ANKS1B* gene.

1.5 AIDA1 in Alzheimer's Disease

1.5.1 AIDA1 Association with APP

Literature has shown that AIDA1 isoforms are known to bind AICD using their PTB domain (Smirnova, 2017). The domain recognizes a YENPTY motif on AICD for binding cleft accommodation. Other proteins that also bind AICD with a PTB domain are Fe65 and Mint1/X11 proteins. The effect of Mint1/X11 and APP binding are previously discussed above. Fe65 is a neuronal adaptor protein that has been shown to bind AICD, with contradictory downstream implications as it has been described as both an enhancer and suppressor of Aβ-peptide secretion (Ando et al., 2001; Sabo et al., 1999).

AIDA1a binds the cytoplasmic tail of APP, referred to as the AICD, at a characteristic YENPTY motif. Co-transfection of AIDA1a with AICD caused colocalization to the cytoplasm, whereas unbound AIDA1a is found uniformly in the cell, including the nucleus (Ghersi et al., 2004). Similarly, AIDA1c/d/e isoforms are also capable of binding APP, with similar localization to the nucleus (Ghersi et al., 2004). However, the AIDA1b isoform is unable to bind AICD (Ghersi et al., 2004).

1.5.2 PTB Domain Auto-Inhibition with APP

As discussed above, PTB-domains are predicted to play a role in the progression of AD due to their APP binding capabilities. However, another key feature of several PTB domains is their auto-inhibition. For instance, X11/Mint1 and Fe65 are structurally autoinhibited from binding APP and will be discussed further. Firstly, the adaptor X11 is predicted to play a role in APP processing, however, there are instances where APP is prevented from attaching to the binding cleft (Matos et al., 2012). X-ray crystallography studies have shown an ⟨-helical linker region at the C-terminus folds back into the PTB domain (Matos et al., 2012). This structure blocks the β2-strand, α1-helix and α2-helix which form the binding cleft for APP (Matos et al., 2012). The main residues involved in this interaction are hydrophobic interactions between Y_{633}, L_{636}, and L_{637} of the inhibitory helix and F_{610}, Y_{614} and F_{617} of the α2-helix (Matos et al., 2012). This leads to a closed conformation of Mint1/X11. Lastly, Fe65 is neuronal adaptor protein that has shown to bind APP in eukaryotes (Russo et al., 1998). Using NMR and X-ray crystallography, the solution structure of Fe65 was found to exist in dimer conformation, although there was monomers and trimers present as well (Feilen et al., 2017). The autoinhibition was found to have been caused by dimerization of the Fe65-PTB monomers that

mimicked the AICD interaction (Feilen et al., 2017). Specifically, the α2-helix of the PTB2 domain unwinds and mimics AICD in the binding cleft forming an identical intramolecular salt bridge (Feilen et al., 2017). Overall, there are diverse mechanisms of PTB domain autoinhibition, ranging from binding cleft imitation to physical blocking from other protein domains.

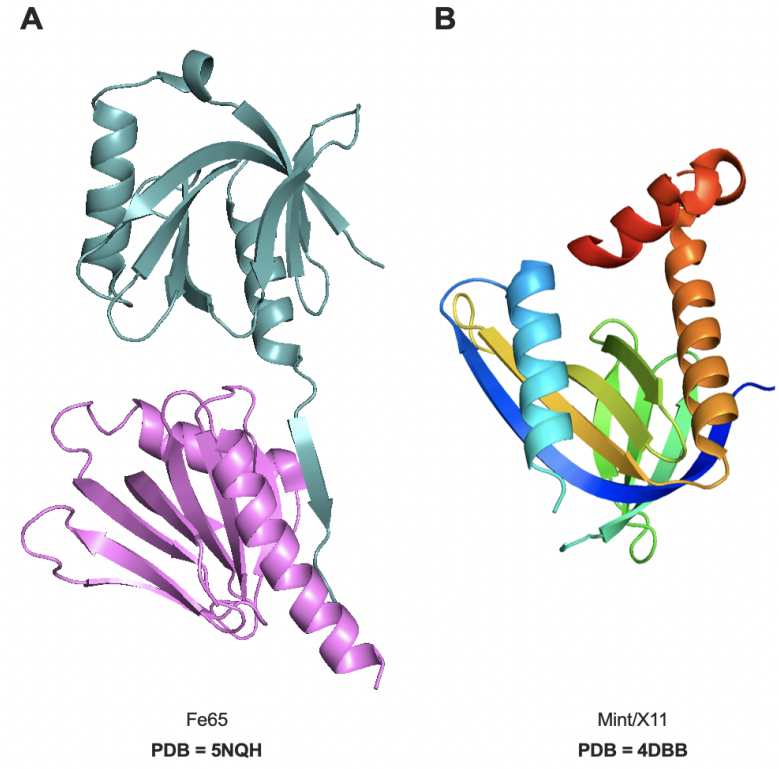

Figure 1.8. PDB structures of various autoinhibited PTB domains. (A) X-ray crystallography structure of homodimer Fe65 which autoinhibits the PTB domain from binding APP (PDB: 5NQH) (Feilen et al., 2017). **(B)** X-ray crystallography structure of autoinhibited Mint/X11 due to C-terminal ⟨-helical (red) folding which prevents APP binding (PDB: 4DBB) (Matos et al., 2012).

1.5.3 AIDA1b Auto-Inhibition

Notably, AIDA1b is the sole isoform unable to bind the AICD peptide using it's PTB domain (Ghersi et al., 2004). This autoinhibition has been shown to be caused by Exon 14, a 25 residue region preceding the SAM1SAM2 domain tandem (Ghersi et al., 2004). The most

obvious explanation for autoinhibition would be that Exon 14 occludes the binding cleft. Although the Exon 14 sequence lacks the typical YENPTY motif, it is plausible that structural similarities or interactions with other aspects of AIDA1b are causing the inhibition.

1.6 Topic of Research: Structural and Functional Studies of AIDA1b

The main hypothesis of the project described is that removal of Exon 14 will result in absence of AIDA1b autoinhibition, increased thermal stability, and altered secondary and 3D structure. AIDA1b is the only isoform that is unable to bind APP due to the presence of Exon 14 in this splice variant. To date, autoinhibition of the AIDA1 PTB domain has only been shown using pull downs from crude lysates. The objective of my thesis is to demonstrate autoinhibition using pure proteins and complementarily biophysical methods. Furthermore, there is also a lack of research regarding AIDA1b's functional and structural characteristics. For example, insight to thermal stability, domain characterization, and secondary structure provides a better understanding of its working capacity. Moreover, comparing wild-type and deletion mutants of AIDA1b can isolate which regions of the protein contribute more to its stability or structure. These properties were measured using DSF, CD and DSC. Using the same set of purified proteins, qualities of the quaternary structure of AIDA1b were determined using SAXS.

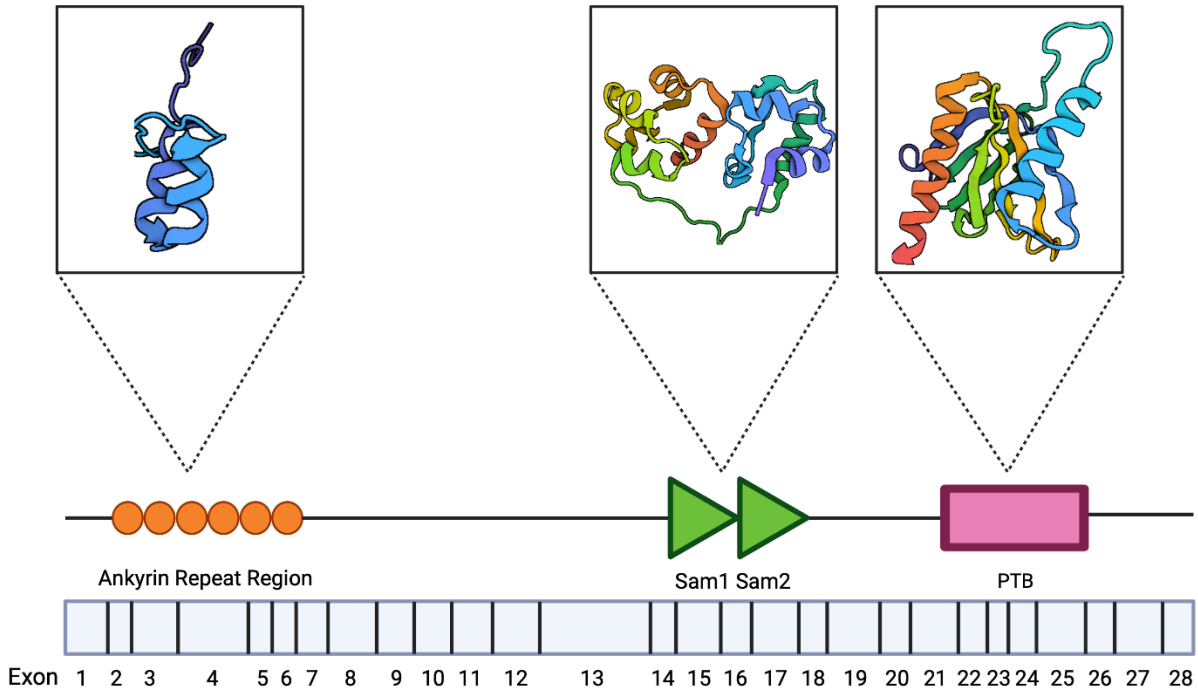

Figure 1.9. Domain, genomic and structural characterization of AIDA1b. Exon organization of AIDA1b shows 28 total exons, with each encoded domain shown above. The ankyrin repeat region (~exons 2-7) is structurally unsolved, thus a similar ankyrin repeat has been shown (PDB: 1AP7). SAM1SAM2 (green) domains (~exons 14-18) with cartoon structure (PDB: 2KIV) and PTB (pink) domain (~exons 21-26) with cartoon structure (PDB: 2M38) are also shown. Figure created using BioRender.

CHAPTER 2: MATERIALS

2.1 Solutions

Table 2.1.1 Buffers for Protein Expression and Purification

Buffer	**Composition**	**Source**
Resuspension Buffer (T300)	50mM Tris, 300mM NaCl, 0.001% NaN_3 (w/v), pH 7.4	Biorad
Wash Buffer	50mM Tris, 300mM NaCl, 0.001% NaN_3 (w/v), pH 7.4	Biorad
Nickel column Imidazole Wash Buffer	10mM imidazole, 49.5mM Tris, 297mM NaCl, 0.001% NaN_3 (w/v), pH 7.4	Biorad
Nickel column Elution Buffer	500mM imidazole, 25mM Tris, 150mM NaCl, 0.0001% NaN_3 (w/v), pH 7.4	Biorad
GST column Elution Buffer	20mM Glutathione, pH 7.4	Biorad

Table 2.1.2 Buffers for Experimental Techniques

Buffer	**Application**	**Composition**	**Source**
PBS	Anisotropy, DSF, DSC, ITC, BLI	137 mM NaCl, 2.7 mM KCl, 4.3 mM Na_2HPO, 1.47 mM KH_2PO, pH 7.4	Biorad
T300	DSF	50mM Tris, 300mM NaCl, 0.001% NaN_3 (w/v), pH 7.4	Biorad
P100	DSF	10mM NaP, 100mM NaCl, pH 7.4	Biorad
Tris pH 7	DSF	50mM Tris, 100mM NaCl, pH 7	Biorad
NaP pH 7.5	DSF	50mM NaP, 100mM NaCl, pH 7.5	Biorad

NaP pH 8	DSF	50mM NaP, 100mM NaCl, pH 8	Biorad
MOPS pH 7	DSF	50mM MOPS, 100mM NaCl, pH 7	Biorad
MOPS pH 8	DSF	50mM MOPS, 100mM NaCl, pH 8	Biorad
MES pH 5.5	DSF	50mM MES, 100mM NaCl, pH 5.5	Biorad
MES pH 6	DSF	50mM MES, 100mM NaCl, pH 6	Biorad
$Na_3C_6H_5O_7$ pH 6	DSF	50mM $Na_3C_6H_5O_7$, 100mM NaCl, pH 6	Biorad
$Na_3C_6H_5O_7$ pH 7	DSF	50mM $Na_3C_6H_5O_7$, 100mM NaCl, pH 7	Biorad
HEPES pH 7	SEC-MALS-SAXS	20mM HEPES, 100mM NaCl, pH 7	Biorad
Sodium Phosphate pH 7.4	CD	7.5mM Na_2HPO_4, 2.5mM NaH_2PO_4, pH 7.4	Fisher Reagents

2.2 Reagents

Table 2.2.1 Reagents for Bacterial Cloning

Application	**Name**	**Source**
GSTAPP	pD441-GST	ATUM
	Electra Enzyme Mix (SapI)	ATUM
	Electra Buffer Mix	ATUM
AIDA1b, Δ14AIDA1b, APP36	Pet28a	GeneUniversal
	pGEX-2T	GeneUniversal
Miscellaneous	Kanamycin	Biorad
	Ampicillin	Biorad

	LB	Biorad
	BL21(DE3) cells	Cryogenic stock
	iQ cells	Cryogenic stock
	100 bp DNA Ladder	Froggabio #DM001-R500
	PCR Mastermix	ThermoFisher #K0171

Table 2.2.2 Reagents for Protein Expression and Purification

Name	**Application**	**Source**
Isopropylthio-β-galactoside (IPTG)	Induction	ThermoFisher #BP1755-1
Precision Plus Protein Dual Color Standards	SDS-Page Protein Ladder	Biorad #1610374
Pierce™ Coomassie Plus (Bradford) Assay Reagent	Protein Quantification	ThermoFisher #23238

Table 2.2.3 Reagents for Experimental Techniques

Experimental Technique	**Name**	**Source**
Fluorescence Anisotropy	Fluorescein isothiocyanate amyeloid precursor protein (FITC APP)	Canpeptide
DSF	SYPRO™ Protein Gel Stains	Thermofisher #S6650
BLI	Ethanolamine	Thermofisher # 149582500
	N-hydroxysuccinimide (NHS)	Thermofisher #24500
	1-ethyl-3-(3-dimethylaminopropyl)carbodiimide (EDC)	Thermofisher #22981
	Octet AR2G Biosensors	Sartorius

2.3 Oligonucleotides and Gene Blocks

Table 2.3.1 Primes for Cloning

Name	Application	T_m (°C)	Source	Sequence
ATUMSEQ_F	GSTAPP	55.8	IDT	CTCGAAAATAATAAAAGGGAAAATCAG
ATUMSEQ_R	GSTAPP	53.0	IDT	TGGTAGTGTGGGGATC

Table 2.3.2 Gene Blocks

Name	Sequence	Plasmid	Source
AIDA1b	CATATGGGATCCGGTACCATAGACAAAATAATGAGTTCAATTGATGTAGGCATTAACAACGAGC TTAAGGAGATGAACGGCGAAACCACCCGTCCACGTTGTCCGGTCCAGACTGTAGGTCAATGGCT GGAGTCCATCGGTCTGCCGCAATACGAGAACCACCTGATGGCGAACGGTTTTGACATGTGCAAT TTATGGGTTCCAACGTGATGGAAGATCAGGACTTATTGGAGATCGGCATCCTGAATAGCGGTCA CCGTCAACGTATCCTGCAAGCGATTCAGCTGCTGCCGAAAATGCGTCCGATTGGCCACGATGGT TATCATCCGACCTCCGTGGCGGAATGGCTGGACAGCATCGAACTGGGCGACTACACCAAGGCGT TCCTGATCAACGGTTATACGAGCATGGATTTGCTGAAAAAGATTTGGGAAGTTGAATTGATCAA CGTCCTGAAGATCAACCTGATCGGCCACCGCAAGCGCATTTTGGCGTCGCTGGGCGATCGTTTG CATGATGACCCGCCACAGAAACCGCCGCGTAGCATTACCCTGCGTGAACCGTCCGGTAATCACA CCCCGCCGCAACTGAGCCCTAGTTTATCGCAGAGCACCTATACGACCGGCGGTTCCTTGGACGT TCCGCATATCATCATGCAGGGTGACGCTCGTAGACGCCGCAACGAAAACTATTTCGACGACATC CCGCGCAGCAAACTGGAACGTCAGATGGCCCAAACCGGTGACTGGGGTGAGCCGAGCATAACC CTGCGCCCACCGAATGAGGCCACCGCAAGCACGCCTGTTCAATACTGGCAGCATCATCCGGAGA AACTGATCTTTCAGTCTTGCGATTACAAGGCTTTCTATCTGGGGTCAATGCTGATCAAAGAGCTG CGCGGCACCGAAAGCACCCAGGATGCGTGCGCAAAAATGCGTGCAAATTGTCAGAAGTCTACT GAGCAGATGAAAAAGGTGCCGACAATTATCTTGTCTGTTAGCTATAAGGGTGTGAAATTCATTG ATGCGACCAATAAAAACATTATCGCCGAGCACGAAATTAGAAATATCAGCTGCGCTGCTCAAG ACCCGGAAGATTTAAGCACGTTTGCATACATTACCAAAGATCTCAAGTCTAACCACCACTACTG CCATGTTTTTACCGCGTTCGACGTGAATCTGGCGTACGAGATCATTTTGACCCTGGGCCAAGCGT TCGAGGTTGCGTACCAGTTGGCTCTGCAGGCACGTAAGTAACTCGAG	pET28a pGEX-4T	Gene Universal
Δ14AIDA1b	CATATGGGATCCGGTACCCCACGTTGTCCGGTCCAGACTGTAGGTCAATGGCTGGAGTCCATCG GTCTGCCGCAATACGAGAACCACCTGATGGCGAACGGTTTTGACAATGTGCAATTTATGGGTTC CAACGTGATGGAAGATCAGGACTTATTGGAGATCGGCATCCTGAATAGCGGTCACCGTCAACGT ATCCTGCAAGCGATTCAGCTGCTGCCGAAAATGCGTCCGATTGGCCACGATGGTTATCATCCGA CCTCCGTGGCGGAATGGCTGGACAGCATCGAACTGGGCGACTACACCAAGGCGTTCCTGATCAA CGGTTATACGAGCATGGATTTGCTGAAAAAGATTTGGGAAGTTGAATTGATCAACGTCCTGAAG ATCAACCTGATCGGCCACCGCAAGCGCATTTTGGCGTCGCTGGGCGATCGTTTGCATGATGACC CGCCACAGAAACCGCCGCGTAGCATTACCCTGCGTGAACCGTCCGGTAATCACACCCCGCCGCA ACTGAGCCCTAGTTTATCGCAGAGCACCTATACGACCGGCGGTTCCTTGGACGTTCCGCATATC ATCATGCAGGGTGACGCTCGTAGACGCCGCAACGAAAACTATTTCGACGACATCCCGCGCAGC AAACTGGAACGTCAGATGGCCCAAACCGGTGACTGGGGTGAGCCGAGCATAACCCTGCGCCCA CCGAATGAGGCCACCGCAAGCACGCCTGTTCAATACTGGCAGCATCATCCGGAGAAACTGATCT TTCAGTCTTGCGATTACAAGGCTTTCTATCTGGGGTCAATGCTGATCAAAGAGCTGCGCGGCAC CGAAAGCACCCAGGATGCGTGCGCAAAAATGCGTGCAAATTGTCAGAAGTCTACTGAGCAGAT GAAAAAGGTGCCGACAATTATCTTGTCTGTTAGCTATAAGGGTGTGAAATTCATTGATGCGACC AATAAAAACATTATCGCCGAGCACGAAATTAGAAATATCAGCTGCGCTGCTCAAGACCCGGAA GATTTAAGCACGTTTGCATACATTACCAAAGATCTCAAGTCTAACCACCACTACTGCCATGTTTT TACCGCGTTCGACGTGAATCTGGCGTACGAGATCATTTTGACCCTGGGCCAAGCGTTCGAGGTT GCGTACCAGTTGGCTCTGCAGGCACGTAAGTAACTCGAG	pET28a pGEX-4T	Gene Universal

APP36	CATATGGCGTGGAGCCACCCCCAGTTCGAGAAAGGCGGCGGGTCAGGCGGGGGCTCAGG CGGGTCAGCGTGGAGCCACCCCCAGTTCGAGAAAATGCAGATTTTTGTTAAGACGCTGACC GGTAAGACCATTACGCTTGAAGTTGAGCCGAGCGACACTATCGAAAACGTCAAGGCTAAA ATCCAAGACAAAGAGGGCATTCCGCCGGATCAGCAGCGCCTGATCTTTGCCGGTAAGCAAC TGGAAGATGGCCGTACCCTGTCTGACTACAATATCCAAAAAGAATCCACGCTGCATTTGG TCCTGCGTCTGCGTGGTCTGGTGCCGCGTGGTAGCTTGGAAGATGCAGCGGTGACCCCTGA GGAACGCCACCTGAGCAAAATGCAGCAGAACGGCTATGAGAACCCAACCTACAAATTCTT CGAGCAAATGCAGAATCGCAGCTAACTCGAG	pET28a	Gene Universal

2.4 Equipment & Software

Table 2.4.1 Equipment for Cloning

Application	**Name**	**Source**
Polymerase Chain Reaction	Techne TC-3000G PCR Thermal Cycler	GMI
Electroporation	BTX™ ECM™ 399 Exponential Decay Wave Electroporator	Fisher Scientific
	Electroporation Cuvettes Plus™	Fisher Scientific
Incubator/Shaker	Barnstead MaxQ 4000 A-Class Benchtop High	Thermo Scientific
	New Brunswick™ I26/I26R Stackable Incubator Shakers	Eppendorf
Heat shock	Isotemp 205 Digital Water Bath	Fisher Scientific
DNA quantification	NanoDrop 2000 spectrophotometer	Thermo Scientific

Table 2.4.2 Equipment for Protein Expression and Purification

Application	**Name**	**Source**
Sonication	Ultrasonic Liquid Processor XL-2000 Series	Misonix
IMAC Purification	Pump P-50	Amersham Biosciences
	PureCube 100 Ni-NTA Agarose	Cube BioTech

SEC Purification	ÄKTA pure™ chromatography system	GE
	HiPrep 16/60 Sephacryl S-100 HR	Cytvia
Concentration	5kDa MWCO centrifugal concentrator column	Fisher Scientific
Protein Quantification	Biomate 3 Spectrophotometer	Thermo Scientific
	BioPhotometer 6131	Eppendorf
Visualization	AlphaImager HP	Alpha Innotech

Table 2.4.3 Equipment for Experimental Techniques

Application	**Name**	**Source**
Fluorescence Anisotropy	Synergy H4 Hybrid microplate reader	Biotek
DSF	RotorGene Q qPCR	Qiagen
Mass Spectrometry	Orbitrap Elite	Thermo Fisher Scientific
	Savant DNA 120 SpeedVac Concentrator	Thermo Fisher Scientific
ITC	MicroCal VP-Isothermal Titration Calorimeter (ITC)	Malvern Panalytical
DSC	Differential Scanning Calorimeter	TA Instruments
SEC-MALS, SAXS	Superdex 200 10/300 Increase SEC column	Cytvia
	Infinity II HPLC	Agilent
CD	J-815 CD Spectrometer	Jasco
BLI	Octet R4	Sartorius

Table 2.4.4 Software

Application	**Name**	**Source**
Fluorescence Anisotropy	Prism	GraphPad
DSF	DSF World	Jason E. Gestwicki, PhD. (UCSF)
ITC	Microcal 7.0	Malvern Panalytical
DSC	Nanoscale	TA Instruments
SEC-MALS-SAXS	RAW, ASTRA	BioXTAS
CD	Spectra Manager	Jasco
BLI	Octet Analysis Studio	Sartorius

CHAPTER 3: METHODS

3.1 Cloning

3.1.1 Cloning of AIDA1, Δ14AIDA1b & APP36

Various clones (AIDA1, Δ14AIDA1b & APP36) were ordered from GeneUniversal. 2ng of respective DNA was added to 100 µL BL21(DE3) competent cells, and electroporated. The cells were rescued with 1000 µL LB, and subsequently incubated at 37 °C and 300 rpm for 1 hour. 100 µL was plated onto either LB/Kan plates and incubated at 37 °C overnight. Colonies were selected and incubated in 2 mL LB/Kan at 37°C and 300rpm overnight. Following, they were stored as cryogenic stocks (800 µL culture, 200 µL DMSO).

3.1.2 Cloning of GST-APP

Primers were designed using SnapGene and ordered from IDT. A gene fragment for APP was ordered from GeneUniversal with *SapI* restriction sites. An Electra reaction was set up with 10µL 125 ng APP gene fragment, 1 µL pD441-GST, 2 µL Electra buffer, 1 µL Electra enzyme mix (SapI) and 6 µL ddH_2O (ATUM). The reaction was incubated for 30 minutes at room temperature, after which 2 µL was added to iQ-competent cells. The cells were heat-shock transformed for 90 seconds at 42 °C, cooled on ice for 5 minutes, and incubated for 1 hour at 37°C and 300rpm after the addition of 1000 µL SOC. The cells were spread-plated on LB/Kan (50µg/mL) and incubated at 37°C for 14 hours. The resultant colonies were screened using water-colony PCR with the original primers (ATUMSEQ_F, ATUMSEQ_R). The PCR was as follows: 30 seconds of 94 °C, 45 seconds of 48 °C, and 1 minute of 72 °C for 30 cycles. Purified DNA was visualized on a 1.2 % agarose gel with EtBr. The positive colony was grown in LB/Kan at 37 °C and 300 rpm.

3.2 Protein Expression and Purification

3.2.1 Protein Expression

An initial 50 mL culture (LB/Kan) was grown overnight at 37 °C and 180 rpm and subsequently transferred to a 1 L culture. Once the 1 L culture was at mid-log phase (OD_{600nm} = 0.5 – 0.7), IPTG was added to a final concentration of 1 mM. The culture was then incubated overnight at 18 °C and 180 rpm. Following incubation, the culture was harvested at 5000xg for 15 minutes at 4 °C, and cell pellets were stored while the supernatant was discarded.

3.2.2 Protein Purification

The cell pellets were resuspended in lysis buffer (T300 - 50 mM Tris, 300 mM NaCl, 0.1% NaN_3, pH 7.4) and lysed using sonication with 10 second on, and 30 second off cycles for 5 minutes. The solution was spun at 16,000xg for 35 minutes at 4°C, the supernatant was diluted with loading buffer (T300 - 50mM Tris, 300mM NaCl, 0.1% NaN_3, pH 7.4) and the pellet was discarded.

An initial purification was performed by nickel affinity chromatography (Cube Bio). The column was washed with 100 mL wash buffer (T300 - 50 mM Tris, 300 mM NaCl, 0.1% NaN_3, pH 7.4), the lysate was pumped at a rate of 12.0 mL/min, after which the column was re-washed with 100 mL wash buffer. A second wash of 10 mM imidazole was run, and a 40 mL sample was eluted with 500 mM imidazole.

The eluted sample was concentrated to 5 mL using a 5 kDa MWCO centrifugal concentrator column and pumped into the ÄKTA pure™ chromatography system (GE) at 1mL/min for a secondary purification. The sample was desalted and buffer-exchanged into PBS (137 mM NaCl, 2.7 mM KCl, 4.3 mM Na_2HPO, 1.47 mM KH_2PO, pH 7.4) and eluted into

1.5mL fractions on a 96-well plate using a HiPrep 16/60 Sephacryl S-100 HR column (Cytvia). Fractions were pooled together and concentrated using a 5 kDa MWCO centrifugal concentrator column. Protease inhibitor phenylmethyl sulfonyl fluoride (PMSF) was added to a final concentration of 1 mM. A buffer exchange was achieved by repeated concentrations with a 5 kDa MWCO centrifugal concentrator column.

3.2.3 Visualization of Proteins

Sample preparation was done by aliquoting 10 µL protein and 10 µL 2x Laemelli Sample Buffer (Bio-rad). 18 µL of desired samples was loaded in succession onto a Mini-PROTEAN® TGX™ 4-20% Precast Gel (Bio-rad). InstantBlue® Coomassie Protein Stain (Abcam) was used to stain the gel. The gel was imaged on an AlphaImager HP (Alpha Innotech).

3.2.4 Protein Quantification

Protein quantification was done using two methods. An A_{280nm} reading was taken, and protein concentration was calculated using the Beer-Lambert law. Secondly, Pierce™ Coomassie Plus (Bradford) Assay Reagent was added to samples of interest, and A_{595nm} was used to estimate the protein concentration relative to a BSA standard curve.

3.3 Fluorescence Anisotropy

A FITC-labelled peptide for APP (FITC-APP) was ordered from CanPeptide (Quebec). AIDA1, Δ14AIDA1b and PTB samples were dialyzed to PBS using 5 kDa MWCO centrifugal concentrator columns. Samples were quantified to 100 µM using a Bradford assay and the Edelhoch method. A 10x serial dilution was conducted with samples of interest and PBS. A final

concentration of 50 nM of FITC-APP was added, with total reaction volume at 50 µL. Samples were transferred to a 96-well black microplate and incubated at room temperature in the dark for 30 minutes. Following, the plate was read on a BioTek Synergy H4 Hybrid Microplate Reader and results were analyzed using Prism 9 software (GraphPad).

3.4 Bio-layer Interferometry

AIDA1, Δ14AIDA1b, PTB, and APP36 samples were buffer exchanged to PBS using 5kDa MWCO centrifugal concentrator columns. Samples were diluted to 5 µM for AIDA1, Δ14AIDA1b, and PTB and a serial dilution of 5 µM, 10 µM, 25 µM and 50 µM for APP36. AR2G tips (Sartorius) were activated with 10 mM NHS and 20 mM EDC, loaded with either AIDA1, Δ14AIDA1b, or PTB and quenched with 1M ethanolamine. The tips were then washed with PSB, associated with APP36 in sequential concentrations from lowest to highest, and disassociated in PBS. The tips were regenerated using 3M GdHCl and neutralized in water. The assay protocol was as follows: equilibration – 60 seconds, activation – 300 seconds, immobilization – 600 seconds, quench – 300 seconds, baseline – 120 seconds, association – 300 seconds, dissociation – 300 seconds, regeneration – 6 seconds, neutralization – 30 seconds. The experiment was done using Octet BLI Discovery Software on an Octet R4 (Sartorius). The raw data was analyzed using Octet Analysis Studio Software (Sartorius) to obtain binding curves.

3.5 Dynamic Scanning Fluorimetry

AIDA1 and Δ14AIDA1b samples were concentrated using 5kDa MWCO centrifugal concentrator columns to 5mg/mL, quantified using a Bradford assay. SYPRO Orange dye (Life, ThermoFisher) was diluted from a 5000X stock to a final concentration of 10X in selected

buffers. 10 buffer conditions were tested, refer to 2.1.2 for specifications. Tubes were created with SYPRO Orange dye, buffer, and 1mg/mL final concentration of desired protein in a total of 50µL. The RotorGene Q qPCR (Qiagen) was used to set fluorescence output at 470nm, detection at 610nm, and gain of 5. The samples were heated from 25°C to 99°C at a 1°C/min rate. Controls of 1mg/mL lysozyme in PBS (positive), 1mg/mL protein in PBS (negative), and 10X final concentration SYPRO Orange dye in PBS (negative). The results were analyzed using DSF World (Jason E. Gestwicki, UCSF) and Prism 9 software (GraphPad).

3.6 Circular Dichroism

AIDA1 and Δ14AIDA1b were buffer exchanged to 10mM sodium phosphate pH 7.4 (7.5 mM Na_2HPO_4 and 2.4 mM NaH_2PO_4) using a 25 kDa MWCO dialysis membrane overnight. Samples were diluted and quantified to 3.5 µM and the molar ellipticity (mdeg) was measured over wavelengths 200-260 nm. The spectra of the solvent (7.5 mM Na_2HPO_4, 2.5 mM NaH_2PO_4, pH 7.4) was subtracted from the sample spectra. Samples were run at a rate of 100 nm/min, with measurements every 0.1 nm at 22°C. Thermal denaturation experiments were monitored at 208 nm and 222 nm during a temperature period of 40 °C - 90 °C, at a rate of 1 °C/min. All experiments were conducted on a J-815 CD Spectrometer (Jasco) using a quartz cuvette, optical path length of 0.1cm, and analyzed on Spectra Manager (Jasco).

3.7 Differential Scanning Calorimetry

AIDA1 and Δ14AIDA1b samples were dialyzed to PBS using 5 kDa MWCO centrifugal concentrator columns and quantified to 100 µM. 1 mL of the sample was loaded into a DSC 250 (TA Instruments). The samples were heated from 5 °C to 85 °C at a rate of 1 °C/min, and cooled

from 85 °C to 5 °C at a rate of 1 °C/min. The heating/cooling cycle was repeated five times at 3 atm. Data was analyzed using Nanoscale (TA Instruments).

3.8 SEC-MALS-SAXS

AIDA1 and Δ14AIDA1b samples were dialyzed to SEC-MALS SAXS buffer (20 mM HEPES, 100 mM NaCl, pH 7) using a 25 kDa MWCO dialysis membrane, and further dialyzed using a 5 kDa MWCO centrifugal concentrator column. Samples were quantified to 5 mg/mL for AIDA1 and 5.5 mg/mL for Δ14AIDA1b using a Bradford assay. 300µL of each sample was injected onto a Superdex 200 10/300 Increase SEC column (Cytvia) on an Agilent Infinity II HPLC. Then, samples were sent through Wyatt DAWN Heleos II MALS, a Wyatt Optilab T-rEX direct refractive index (dRI) detector and targeted by a SAXS synchrotron beamline. RAW and ATSAS was used to analyze the data. The DAMMIF tool was used to create bead models. The bead models were then aligned to the Alphafold predicted structure used the cifsup extension in RAW, with the bead model being averaged and refined from fifteen structural predictions.

CHAPTER 4: RESULTS

4.1 Expression and Purification of Studied Proteins

4.1.1 Expression and purification of AIDA1

The main proteins of interest for this project consisted of a 47.4 kDa fragment of AIDA1b extending from Exon 14 to Exon 20 (AIDA1b) and Δ14AIDA1b, a deletion mutant of Exon 14. Expression trials were conducted on AIDA1b (Figure 4.1) after transformation of a pre-ordered, ligated plasmid (pET28a) that contained the respective gene sequence. Transformations were tested by plating on LB/Kan plates and LB/Amp plates, to verify no cross-contamination. Following, the protein was expressed/induced at 18 °C, because prior trials at 37 °C yielded minimal protein yield. The lysate was purified by affinity chromatography, followed by size exclusion chromatography. The protein was stable for at least one week, with some degradation occurring thereafter as monitored by SDS-PAG. Repeated freeze/thawing cycles of AIDA1b is not advised as some precipitate was observed.

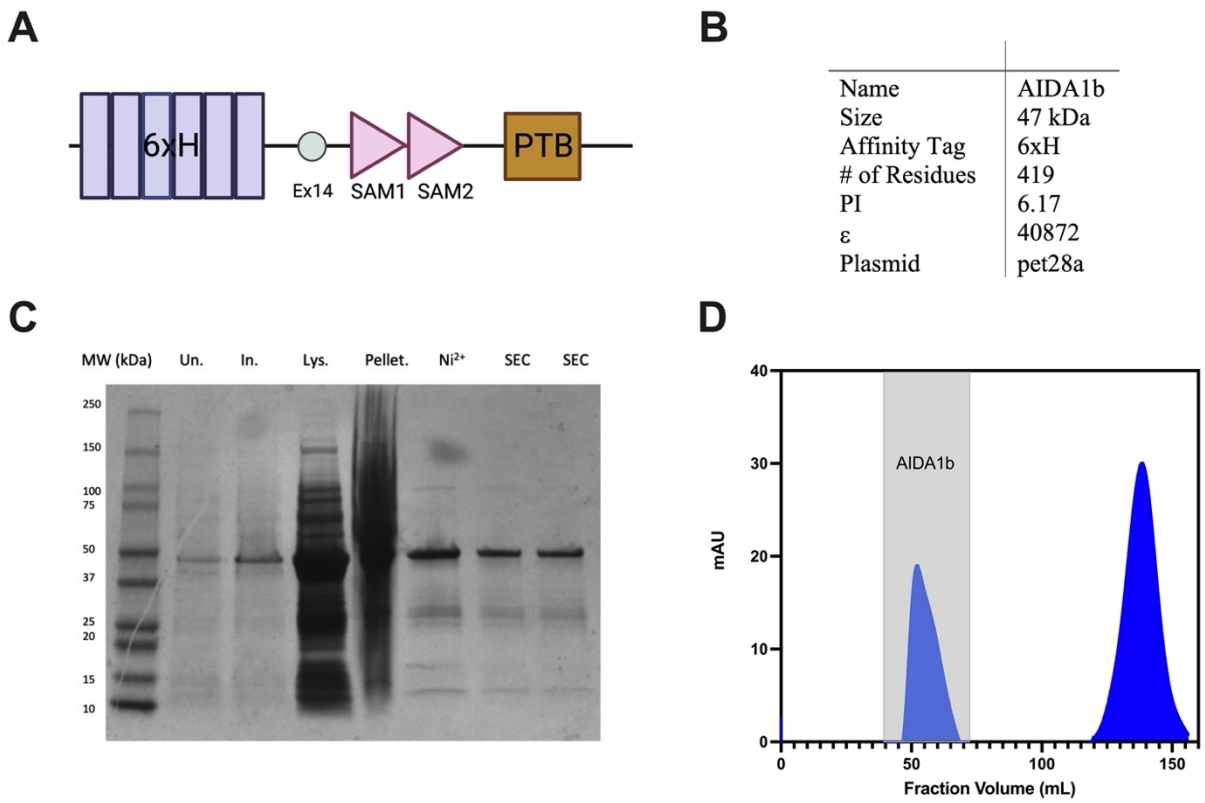

Figure 4.1 Expression and purification of AIDA1b. (A) A visual representation of AIDA1b structure with a 6xH affinity tag and notable domains Sam1Sam2 and PTB. Created using BioRender. **(B)** Table with structural and chemical properties of AIDA1b. **(C)** The purification scheme was performed on BL21 (DE3) transformed cells with the AIDA1b gene block in pet28a (GeneUniversal). An SDS-Page visualization where: "Un" = uninduced culture, "In" = induced culture for 18 hours at 18°C, "Lys" = lysate post-sonication and centrifugation, "Pellet" = pellet post-lysis and centrifugation, "Ni^{2+}" = post IMAC nickel column eluted with 500mM imidazole, "SEC" = post SEC, buffer exchanged into PBS). AIDA1b is 47kDa. **(D)** SEC elution profile from ÄKTA pure™ (GE), whereby AIDA1b eluted between 40-70mL, at fractions A4-C8.

4.1.2 Expression and purification of Δ14AIDA1b

I hypothesized that the lack of Exon 14 in Δ14AIDA1b would relieve autoinhibition of the PTB domain. Δ14AIDA1b is 44.6kDa and showed similar low MW impurities which were removed using a 30kDa MWCO centrifugal concentrator column. Again, similar to AIDA1b, these bands often reappeared post 7+ day storage at 4°C and was incapable of being stored at -20°C due to significant precipitation. This represents similar instability of both AIDA1b and Δ14AIDA1b in terms of temperature sensitivity and storage capabilities.

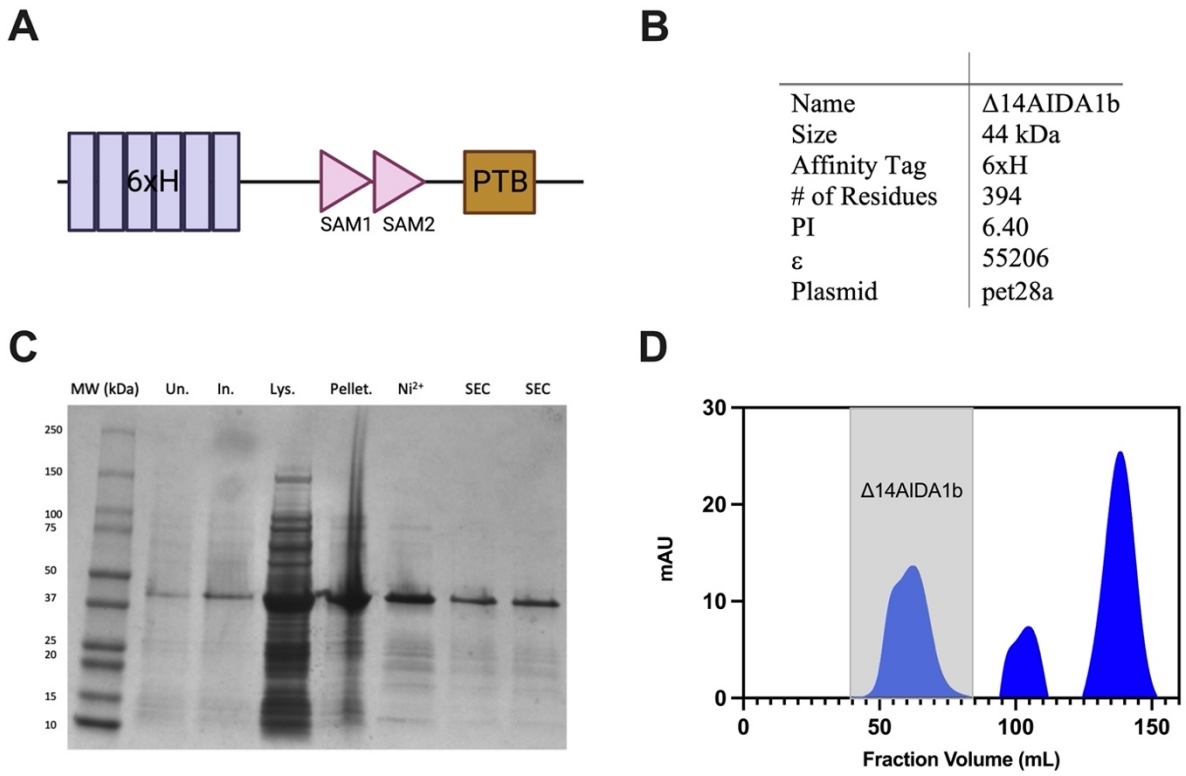

Figure 4.2. Expression and purification of Δ14AIDA1b. (A) Visual representation of Δ14AIDA1b structure with a 6xH affinity tag, and notable domains Sam1Sam2, PTB. Created in BioRender. **(B)** Table containing chemical and structural properties of Δ14AIDA1b. **(C)** The purification scheme was performed on BL21 (DE3) transformed cells with the Δ14AIDA1b gene block in pet28a (GeneUniversal). SDS-Page visualization where: "Un" = uninduced culture, "In" = induced culture for 18 hours at 18°C, "Lys" = lysate post-lysis and centrifugation, "Pellet" = pellet post-lysis and centrifugation, "Ni^{2+}" = post IMAC nickel column eluted with 500mM imidazole, "SEC" = post SEC, buffer exchanged into PBS. Ni^{2+} IMAC was done using a Pharmacia Biotech Chromatographie column XK50/60 (Pharmacia Biosciences) and SEC was done on a ÄKTA pure™ chromatography system (GE). Δ14AIDA1b is 45kDa. **(D)** SEC elution profile from ÄKTA pure™ (GE), whereby Δ14AIDA1b eluted between 50-70mL, at fractions A6-C9.

4.1.3 Expression and purification of PTB

The PTB domain alone has been previously solved by NMR methods in the Donaldson laboratory (Smirnova et al, 2012). This PTB domain used here and for the structure was solubility enhanced, containing five aromatic/aliphatic substitutions. An established purification protocol was followed with Ni^{2+} IMAC purification, followed by size exclusion chromatography.

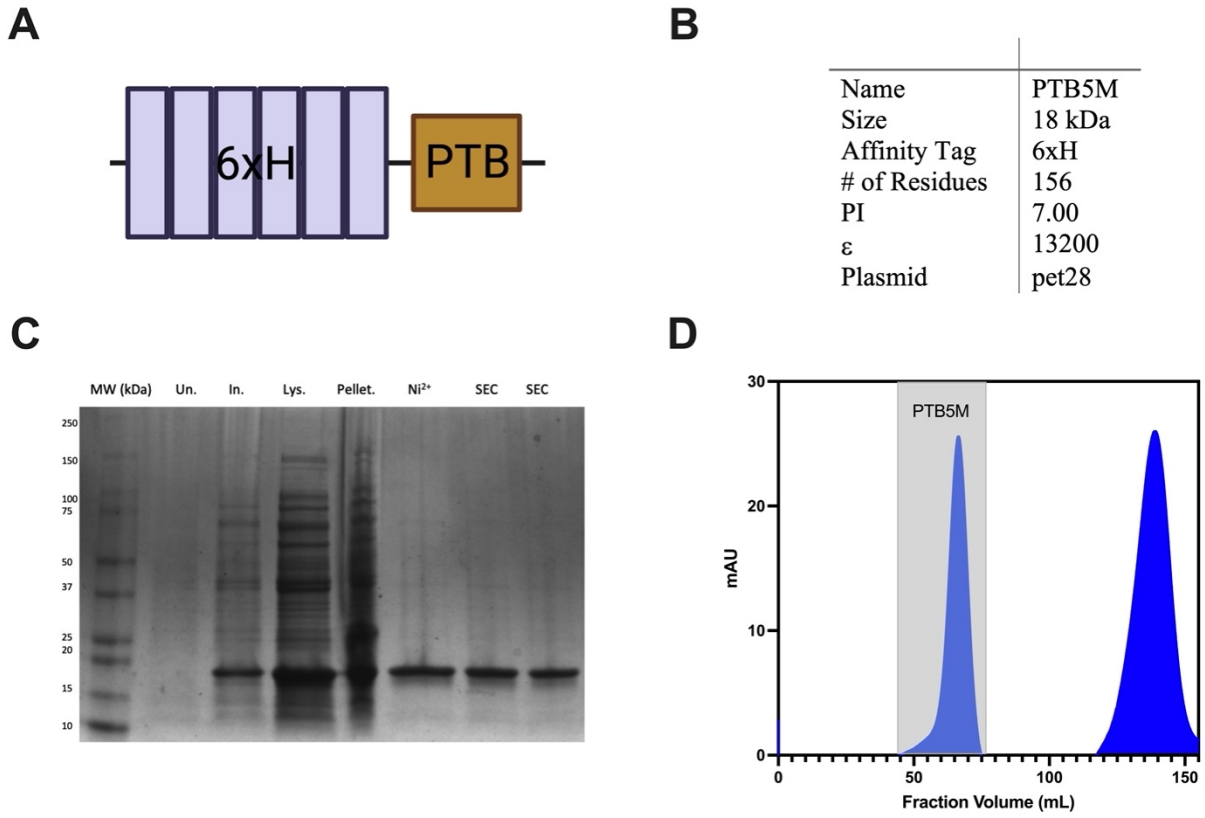

Figure 4.3. Expression and purification of PTB5M. (A) Visual representation of PTB5M structure, with a 6xH affinity tag. Created in BioRender. **(B)** Table listing chemical and structural properties of PTB5M. **(C)** A prior lab freezer stock was used for the expression of PTB5M. SDS-Page visualization where: "Un" = uninduced culture, "In" = induced culture for 18 hours at 18°C, "Lys" = lysate post-lysis and centrifugation, "Pellet" = pellet post-lysis and centrifugation, "Ni^{2+}" = post IMAC nickel column eluted with 500 mM imidazole, "SEC" = post SEC, buffer exchanged into PBS. PTB5M is 18.7kDa. **(D)** SEC elution profile from ÄKTA pure™ (GE), whereby PTB5M eluted between 60-75mL, at fractions A5-B7.

4.1.4 Expression and purification of APP36

There are two clones of the APP AICD that were used, that of APP36 (Figure 4.4) and GST-APP (Figure 4.5). Both APP were affinity tagged with 6xHis (APP36) or GST (GST-APP), which allowed for a diverse profile of assays and studies to be conducted. APP36 was expressed at 18°C for a better protein yield. The expected molecular weight of APP36 is 16.3kDa.

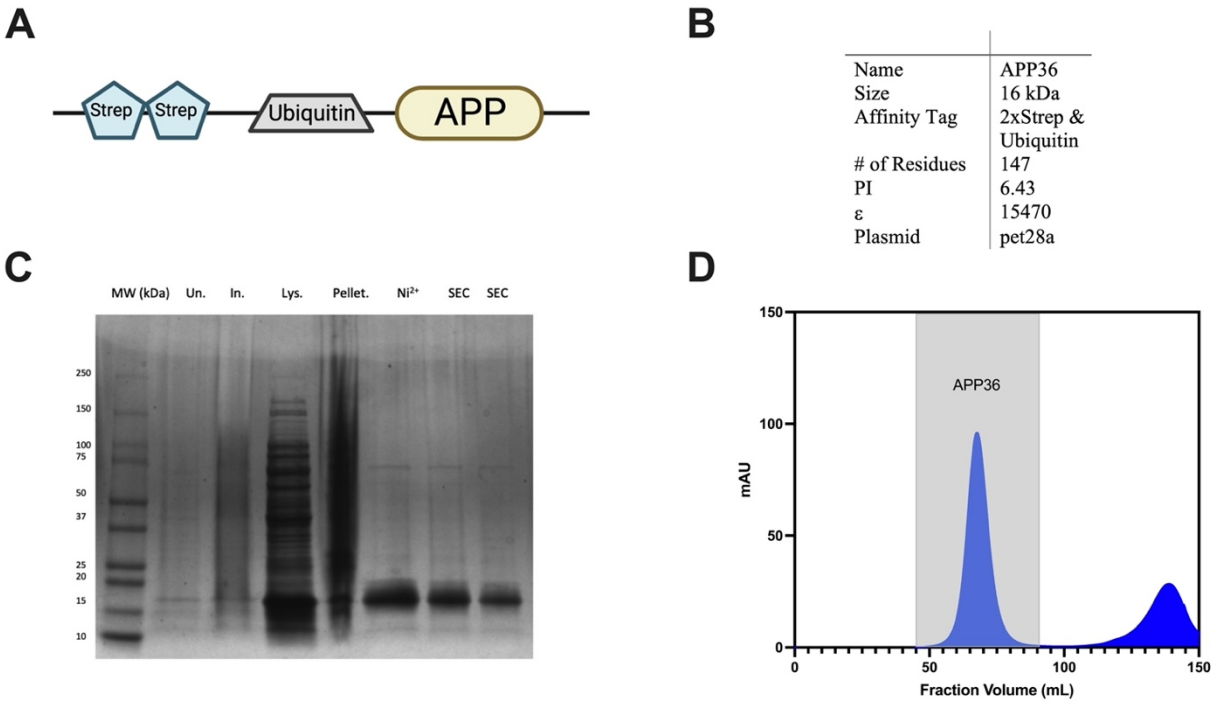

Figure 4.4 Expression and purification of APP36. (A) Visual representation of APP36 structure, with a 2xStreptactin tag and Ubiquitin tag. Created in BioRender. **(B)** Table listing chemical and structural properties of APP36. **(C)** The purification scheme was performed on BL21 (DE3) transformed cells with the APP36 gene block in pet28a (GeneUniversal). SDS-Page visualization where: "Un" = uninduced culture, "In" = induced culture for 18 hours at 18°C, "Lys" = lysate post-lysis and centrifugation, "Pellet" = pellet post-lysis and centrifugation, "Ni^{2+}" = post IMAC nickel column eluted with 500mM imidazole, "SEC" = post SEC, buffer exchanged into PBS. Ni^2. APP36 is 16.4kDa. **(D)** SEC elution profile from ÄKTA pure™ (GE), whereby APP36 eluted between 55-80mL, at fractions C6-D12.

4.1.5 Expression and purification of GST-APP

The next protein, GST-APP, was cloned using Electra protocols, where SapI was the restriction enzyme used to insert the APP gene of interest into a pD441-GST plasmid. As seen in Figure 4.4B, colony 3 produced the correct sized insert, 946 bp. Following, the glycerol stock was used to do expression trials, and similar to above, the 18°C expression produced a higher quantity of protein, although the overall expression was still lower compared to other clones. The protein eluted in the expected fractions post-SEC, however, upon storage at 4°C for 7+ days, there was often a second band on an SDS-PAGE at 26kDa. This may represent possible cleavage or degradation of the GST-APP protein since the APP peptide was only 4kDa. Degradation was mitigated by adding the protease inhibitor, PMSF.

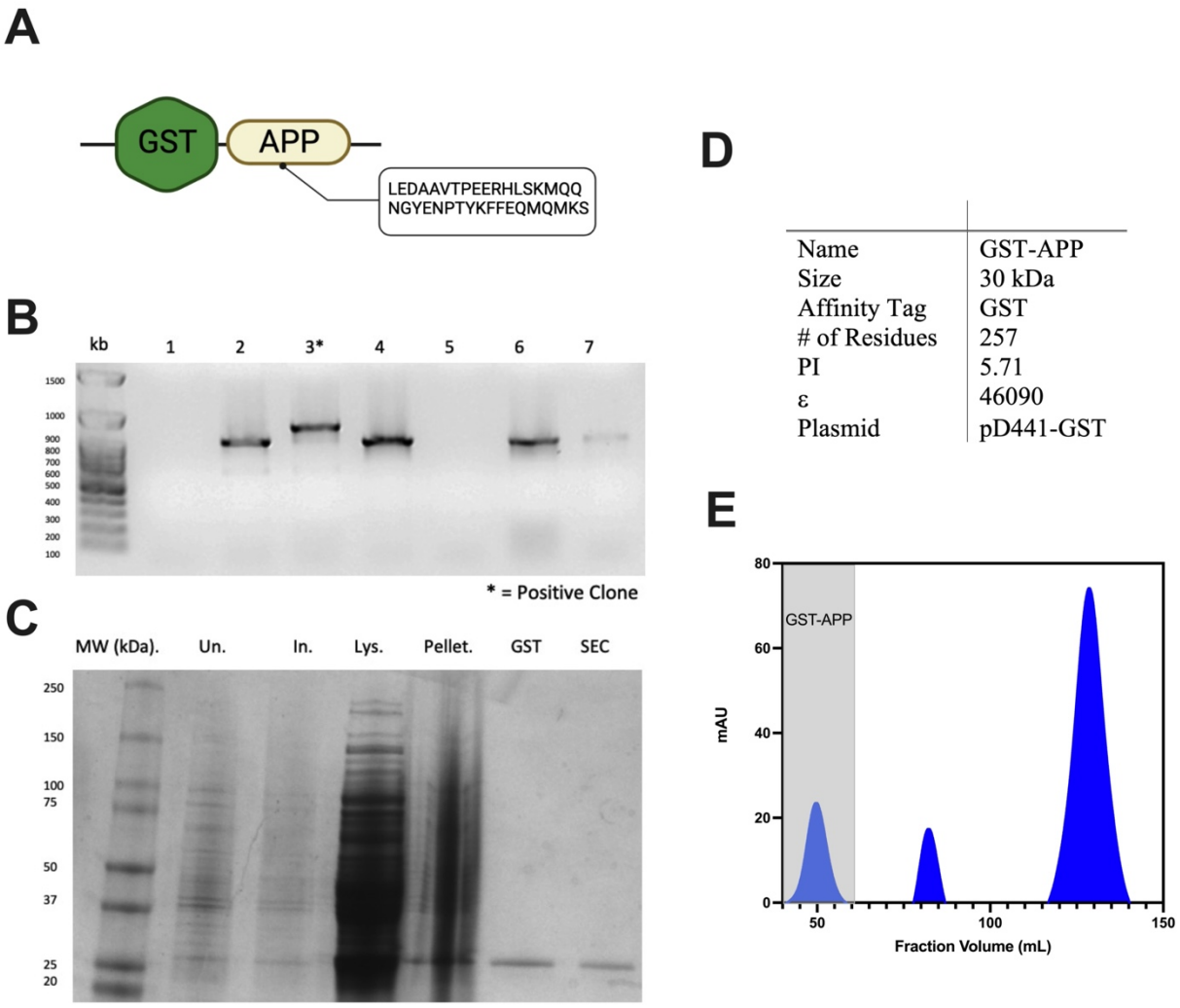

Figure 4.5. Expression and purification of GST-APP. (A) Visual representation of GST-APP structure, with a GST affinity tag. Created in BioRender. **(B)** 1.25% agarose gel electrophoresis to confirm successful ligation of desired insert (APP = 946 bp) into plasmid (pD441-GST) following the Electra method (ATUM). **(C)** SDS-Page visualization where: "Un" = uninduced culture, "In" = induced culture for 18 hours at 18°C, "Lys" = lysate post-lysis and centrifugation, "Pellet" = pellet post-lysis and centrifugation, "GST" = post IMAC GST column eluted with 20mM glutathione (pH 7.4), "SEC" = post SEC, buffer exchanged into PBS. GST IMAC was done using a Pharmacia Biotech Chromatographie column XK50/60 (Pharmacia Biosciences) and SEC was done on a ÄKTA pure™ chromatography system (GE). GST-APP is 27kDa. **(D)** Table listing structural and chemical properties of GST-APP. **(E)** SEC elution profile from ÄKTA pure™ (GE), whereb GST-APP eluted between 40-60mL, at fractions A2-B6.

4.2 Binding studies show Exon 14 participates in the auto-inhibition of AIDA1b

4.5.1 Fluorescence anisotropy studies between AIDA1, Δ14AIDA1b and APP

The first binding assay done to measure the binding capacity of AIDA1b and Δ14AIDA1b used a fluorescent peptide (FITC-labelled APP17) ordered from CanPEPTIDE (Figure 4.6). As a positive control, PTB5M was used to compare with previous research done by lab members, but also understand how the K_d can potentially change between the domain alone vs the wild-type protein. For the positive control (PTB5M = blue), a K_d of 7.5 μM was obtained, with a clean curve, and all measured values falling along the fit. The scatter plots were fit with a one-site binding analysis on GraphPad PRISM. The titration for AIDA1b (green) with FITC-labelled APP17 showed no binding, as evident in Figure 4.6D since there is no evident trend or curved relationship. Lastly, the titration for Δ14AIDA1b (red) with FITC-labelled APP17 also showed binding, albeit not as strong as PTB5M alone. The K_d found for this specific titration is 12.5 μM, showing lower binding affinity, but also a higher margin of error since the data points are not well aligned with the predicted curve. A blank well of FITC-labelled APP in PBS buffer was subtracted from the anisotropy values to normalize the data.

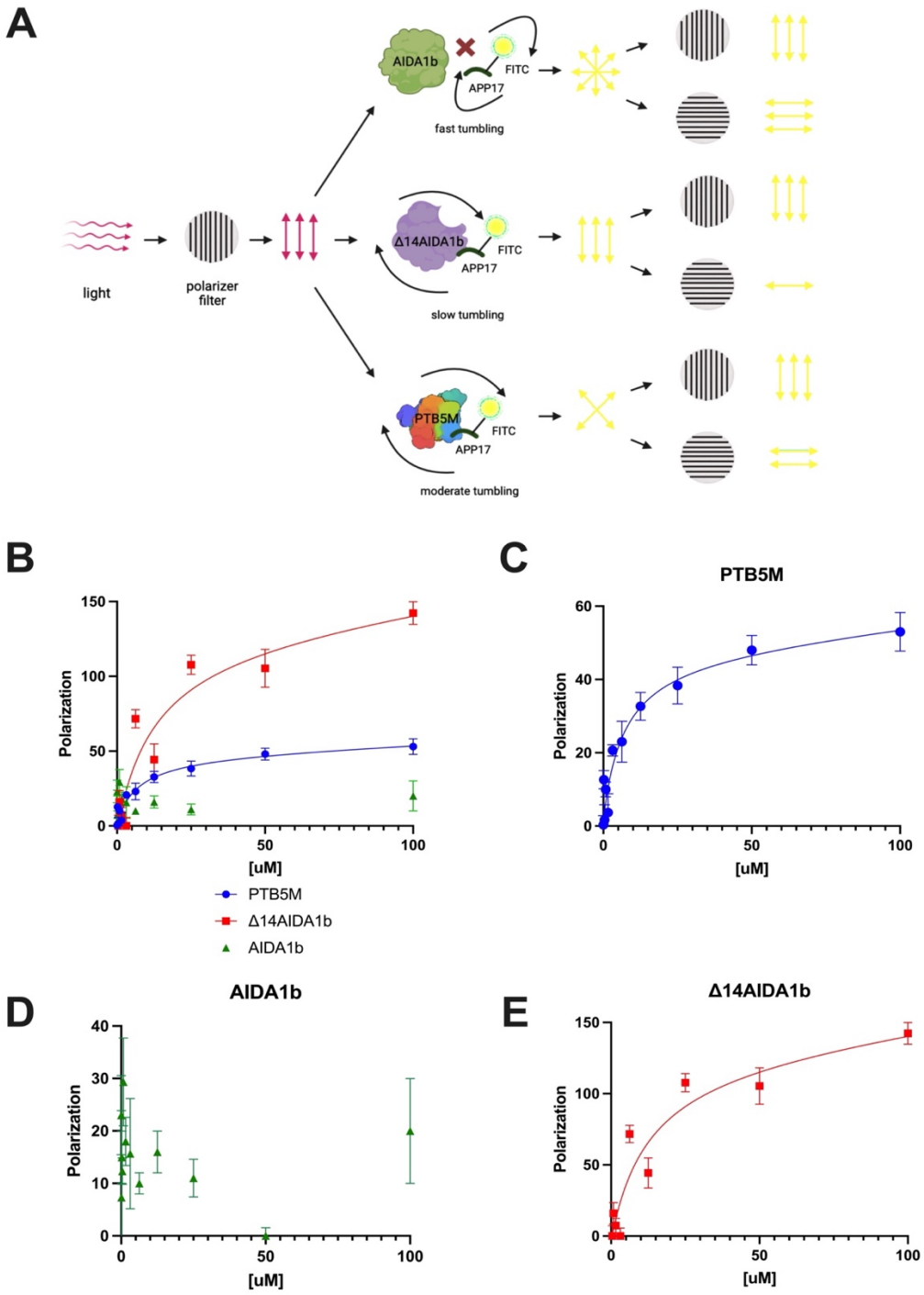

Figure 4.6 Fluorescence anisotropy binding assay for PTB, AIDA1b and Δ14AIDA1b with APP. (A) Scientific theory behind fluorescence anisotropy. Created in BioRender. Binding studies were carried out for **(B)** PTB (blue), AIDA1b (green) and Δ14AIDA1b (red) with FITC-APP. **(C)** 100µM of PTB was incubated for 30 minutes with 50nM FITC-APP in the dark at 23°C and displayed a K_d = 7.5 µM (R^2 = 0.9190) **(D)** Similar conditions were used to test Δ14AIDA1b showing a K_d = 12.5 µM (R^2 = 0.8808) and **(E)** AIDA1b with no binding. Results were analyzed and graphed using GraphPad PRISM.

4.5.2 BLI studies between AIDA1, Δ14AIDA1b and APP

Next, BLI was used as a complementary method to fluorescence anisotropy. The experiment was done with PBS as the kinetic buffer, however, to account for non-specific binding, 1% BSA, sucrose and detergent was added (Dubrow et al., 2022). AR2G tips were used due to their versality, whereby activation with EDC/NHS allowed for association of any protein, in this case PTB, AIDA1b and Δ14AIDA1b. The analysis of the raw data (Figure 4.7B) for PTB (green) revealed a K_d of 5.8 ± 0.90 μM, with an $R^2 = 0.9988$, showing a strong fit. This is similar to the results of the fluorescence anisotropy presented here, as well as in previous literature. Moving forward, AIDA1b (blue) displayed some unusual results, since the association stage showed binding to APP. However, upon analysis of the results, it was concluded that this was most likely non-specific binding, since the response calculated for each consecutive concentration was the same value. Theoretically, as the concentration of the ligand increases, the response should as well, since there is a greater amount of product attaching to the sensor, and later being removed when the tip is dipped into buffer. This is most likely because of the nature of AR2G tips, and despite accounting for nonspecific binding, it was still present. Lastly, Δ14AIDA1b (red) raw data analysis also showed a moderately well-fit binding curve (R^2 = 0.5623), whereby the K_d obtained was 7.8μM ± 6.1μM. These results are again, similar to the FA in that the fit is less strong, and the affinity for APP is reduced, perhaps due to some other inhibitory factor.

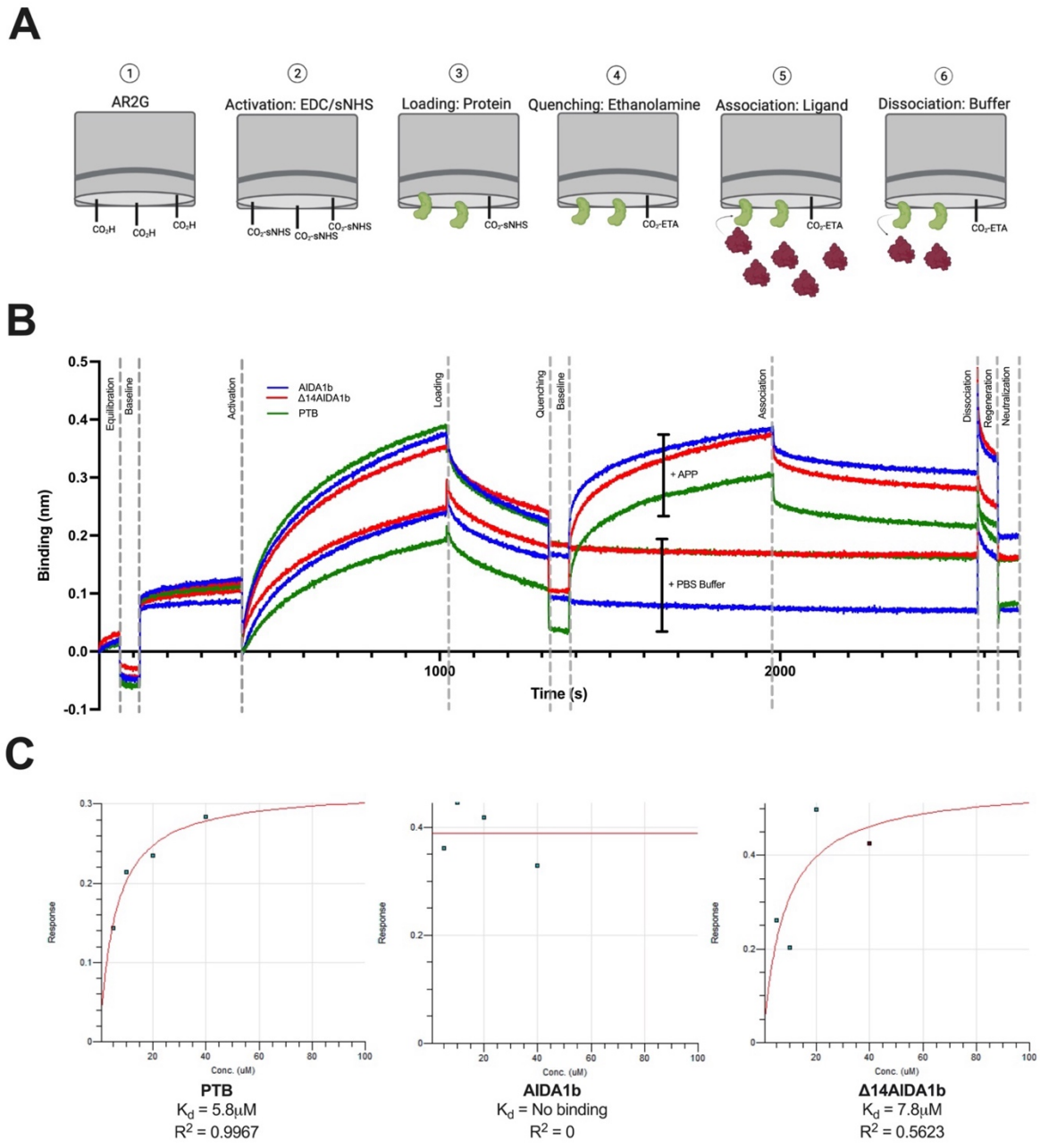

Figure 4.7. Biolayer interferometry binding analysis for PTB, AIDA1b and Δ14AIDA1b with APP. (A) Schematic visualizing the method of AR2G tips. Adapted from Sartorius and created in BioRender. **(B)** Raw data results from BLI assay between AIDA1b (blue), Δ14AIDA1b (red) and PTB (green), with the addition of APP or buffer in the association stage labelled. AR2G tips were equilibrated in water, activated with 10mM EDC/20mM s-NHS, loading with each respective protein, quenched with 1M ethanolamine, associated with 5 μM, 10 μM, 20 μM or 40 μM APP. Only 10 μM or PBS buffer is shown. All experiments were done in PBS on an Octet R4 (Sartorius). **(C)** Kinetic analysis of raw data revealed no binding for AIDA1b, a K_d of 5.8 μM with $R^2 = 0.9967$ for PTB, and a K_d of 7.8 μM with an $R^2 = 0.5623$ for Δ14AIDA1b. Data was analyzed on Octet Analysis Studio (Sartorius).

4.3 Exon 14 does not impact the thermal stability of AIDA1b

4.2.1 AIDA1b and Δ14AIDA1b display similar melting temperatures but varying ideal buffer conditions

I examined the chemical and structural properties of AIDA1b and Δ14AIDA1b using differential scanning fluorimetry (DSF), circular dichroism (CD), and differential scanning calorimetry (DSC). Firstly, the DSF or thermofluor assay, as shown in Figure 4.8, tested the stability of both proteins in various buffers, along with measuring its unfolding as a function of time to determine its melting point (T_m). The raw data for AIDA1b (Figure 4.8A) and Δ14AIDA1b (Figure 4.8B) displays a few notable similar trends. There is a significant difference in the unfolding of both AIDA1b and Δ14AIDA1b in 50 mM MES, 100 mM NaCl and pH 5.5 compared to the other buffer conditions. Since there is another condition with 50 mM MES but high pH (pH 6), the data suggests that below pH 6 the proteins are much more unstable, with a T_m of 48.2 °C and 48.5°C for AIDA1b and Δ14AIDA1b respectively. Although pH 5.5 is close the proteins predicted pI of 6.4 for AIDA1b and 6.2 for Δ14AIDA1b, it is possible that the structure does not favour stability in low pH, perhaps due to other interactions with the buffer. Another similarity between the data for both proteins is that neither unfolded or aggregating prior to the gradient temperature increase, and would suggest that at room temperature, the buffer conditions would not make a significant impact on how the protein behaves.

For AIDA1b, the most stable condition was 50 mM MOPS, 100 mM NaCl, pH 8 with a T_m = 60.2 °C whereas for Δ14AIDA1b it was phosphate-buffered saline, with a T_m = 64.4 °C. In Figure 4.8C, each buffer condition was tested for significance with an unlinked t-test between AIDA1b and Δ14AIDA1b with the results and significance shown in Figure 4.8D. The buffer conditions that caused significant differences in the melting temperature of both proteins, in

order of decreasing *p*-value were: *(i)* 50 mM Tris, 100 mM NaCl, pH 8 *(ii)* 50 mM MOPS, 100 mM NaCl, pH 8, *(iii)* 50 mM sodium citrate, 100 mM NaCl, pH 7, *(iv)* 50mM sodium citrate, 100 mM NaCl, pH 8 , and *(v)* PBS.

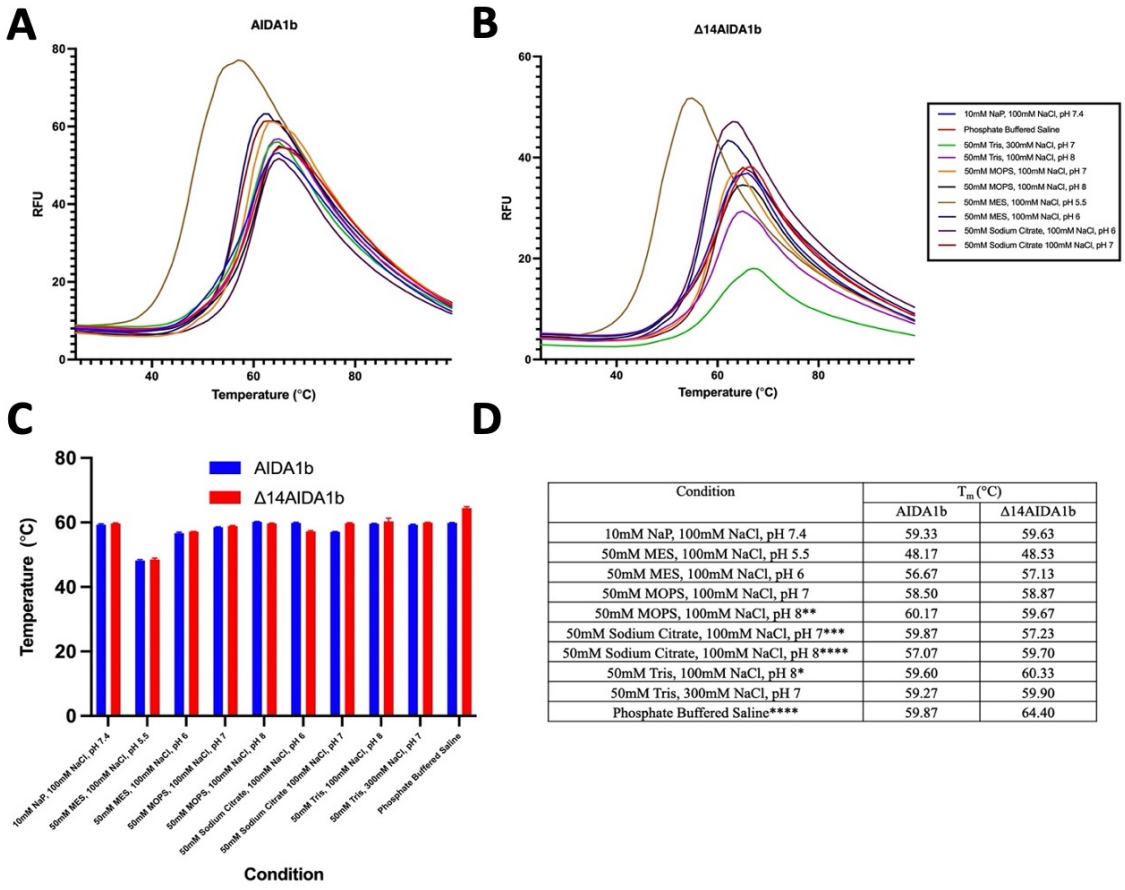

Condition	T_m (°C)	
	AIDA1b	Δ14AIDA1b
10mM NaP, 100mM NaCl, pH 7.4	59.33	59.63
50mM MES, 100mM NaCl, pH 5.5	48.17	48.53
50mM MES, 100mM NaCl, pH 6	56.67	57.13
50mM MOPS, 100mM NaCl, pH 7	58.50	58.87
50mM MOPS, 100mM NaCl, pH 8**	60.17	59.67
50mM Sodium Citrate, 100mM NaCl, pH 7***	59.87	57.23
50mM Sodium Citrate, 100mM NaCl, pH 8****	57.07	59.70
50mM Tris, 100mM NaCl, pH 8*	59.60	60.33
50mM Tris, 300mM NaCl, pH 7	59.27	59.90
Phosphate Buffered Saline****	59.87	64.40

Figure 4.8. Differential scanning fluorimetry of AIDA1b and Δ14AIDA1b to test buffer sensitivity and melting temperature. Temperature dependent unfolding was measured for **(A)** AIDA1b and **(B)** Δ14AIDA1b using SYPRO orange in various buffer conditions, (seen in the legend to the right of B). The raw data was entered into DSFWorld, and the **(C)** mean melting temperatures of AIDA1b (blue) and Δ14AIDA1b (red) were plotted as a bar graph using GraphPad PRISM with error bars. **(D)** Mean melting temperature of each buffer condition with tests of significance using GraphPad PRISM. * = $p < 0.05$, ** = $p < 0.01$, *** = $p < 0.001$, **** = $p < 0.0001$.

4.2.2 CD thermal denaturation confirms limited influence of Exon 14 in AIDA1b thermal stability

A CD spectroscopy-based assay was performed to compare thermal denaturation with the results from DSF. Both AIDA1b and Δ14AIDA1b were subject to a gradual temperature increase from 40°C to 90°C. A monitoring wavelength of 208 nm characteristic of alpha helices was selected (Figure 4.12). The first derivative of the raw data for AIDA1b reveals a T_m of 58.0°C (Figure 4.9B), and a reverse temperature scan also showed no renaturation, with white precipitate evident in the cuvettes. Similar to AIDA1b, the first derivate of the raw data for Δ14AIDA1b reveals a T_m of 58.0°C, with no successful renaturation. The similar behaviour of these proteins can be attributed to the buffer (7.5 mM Na_2HPO_4, 2.4 mM NaH_2PO_4, pH 7.4), whereby both samples had identical stability. Superimposition of both the raw data and first derivative graphs for AIDA1b and Δ14AIDA1b reveal near identical plots.

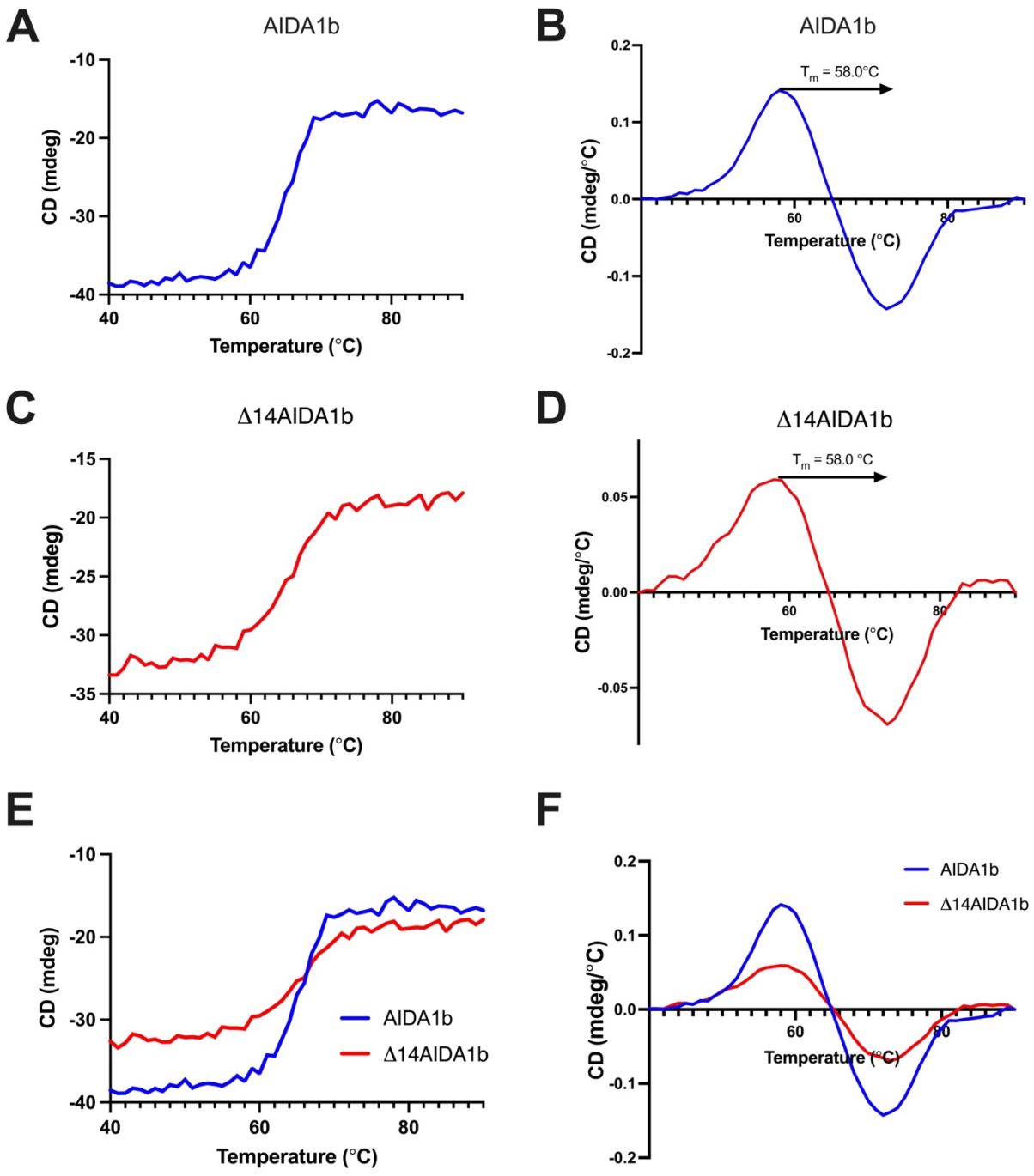

Figure 4.9. Thermal denaturation of AIDA1b and Δ14AIDA1b using circular dichroism to measure melting temperature. (A) The raw thermal denaturation profile for 3.5 µM AIDA1b measured at 208 nm over 40 – 90°C. **(B)** First derivative graphical representation of AIDA1b thermal melt, with a melting temperature of 58°C, done using Spectra Manager (Jasco). **(C)** The raw thermal denaturation profile for 3.5 µM Δ14AIDA1b measured at 208 nm over 40 – 90°C. **(D)** First derivative representation of Δ14AIDA1b thermal melt, with a melting temperature of 58°C. **(E)** Superimposition of AIDA1b (blue) and Δ14AIDA1b (red) raw thermal denaturation profile. **(F)** Superimposition of AIDA1b (blue) and Δ14AIDA1b (red) thermal melt first

derivative graphical representation. All experiments were done in 10mM sodium phosphate (7.5 mM Na_2HPO_4 and 2.4 mM NaH_2PO_4) on a J-815 CD Spectrometer (Jasco).

4.2.3 The loss of Exon 14 causes higher free energy, enthalpy and entropy in AIDA1b

DSC was used to determine thermal transition temperatures and obtain thermodynamic parameters including enthalpy, entropy and free energy. For AIDA1b, as shown in Figure 4.10, the melting temperature was found to be 57.8 ± 0.300°C, representing the maxima of three trials averaged. Furthermore, after ten sequential thermal melts (Figure 4.10A), following by cooling cycles, the protein did not refold. This confirms the results from the CD study that AIDA1b is not stable enough to refold when subject to a reducing temperature gradient. By integrating the area from each peak, it was possible to determine the enthalpy of the reaction, 399.8 ± 41.90 kJ. This value represents the energy required to complete the endothermic reaction of melting AIDA1b. The other two values obtained from this experiment are the entropy of protein unfolding and Gibbs free energy. The entropy, found to be 6.91 ± 0.0800 kJ/K, represents the increase in disorder upon the protein losing bonds and interactions that contributed to conformational stability. Lastly, the Gibbs free energy represents the change in energy between the folded and unfolded states of AIDA1b, in this case 330.6 ± 5.900 kJ. However, since AIDA1b does not refold, the Gibbs free energy does not represent a reversible reaction. All experiments were done in PBS buffer at a concentration of 100 μM based on recommend protocols.

Next, the same experiment was repeated on Δ14AIDA1b in identical buffer and concentration conditions to allow for comparison. An average of three thermal denaturation's gave a melting temperature of 59.4°C ± 0.0700 °C, which is similar to what was shown on the DSF assay in PBS buffer. Furthermore, the change in enthalpy for the Δ14AIDA1b unfolding reaction was 486.1 ± 41.30 kJ. The entropy and Gibbs free energy was found to be 8.2 ± 0.70

kJ/K and 404.2 ± 34.90 kJ respectively. Similar to AIDA1b, Δ14AIDA1b was unable to refold when subject to a cooling temperature gradient (Figure 4.11B).

Overall, the curves for AIDA1b and Δ14AIDA1b display a similar trend in the minimal and maximal values of molar heat capacity measured for the duration of the reaction. However, the T_m for Δ14AIDA1b was higher, supporting the DSF assay results, perhaps showing that it is the more stable mutant when compared to AIDA1b. Moreover, the change in enthalpy was higher for Δ14AIDA1b and differs by at least a magnitude of 2 SD. In addition, since Δ14AIDA1b is the smaller protein, it is reasonable to predict that this value also supports the theory of AIDA1b being more stable upon removal of Exon 14.

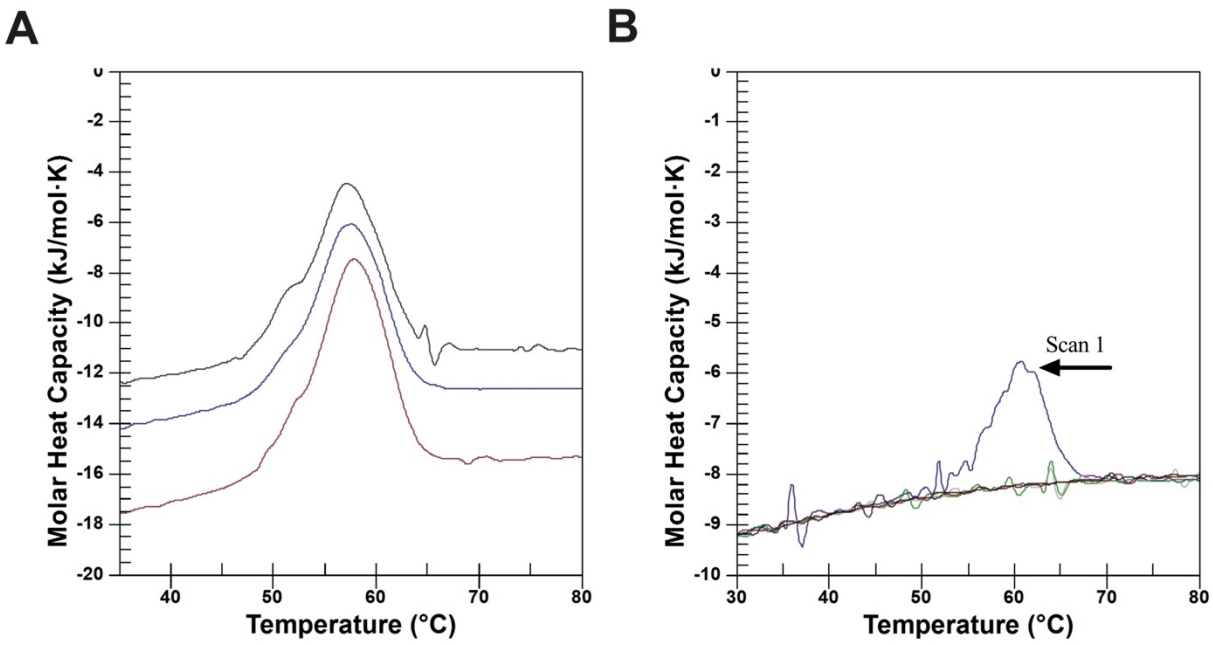

C

AIDA1b	Average	St. Dev.
T_m (°C)	57.85	0.31
Enthalpy (ΔH) (kJ)	399.79	41.89
Entropy (ΔS) (kJ/K)	6.91	0.08
Gibbs Free Energy (ΔG) (kJ)	330.63	5.94

Figure 4.10. DSC molar heat capacity profiles for AIDA1. (A) Superimposition of three thermal denaturation scans for 100 µM AIDA1b in PBS. Molar heat capacity was measured by heating a 1mL sample from 5°C to 85°C at a rate of 1°C/min. **(B)** Molar heat capacity profiles for ten sequential thermal denaturation's of AIDA1b, measured from 5°C to 85°C at a rate of 1°C/min. The first scan is marked by the black arrow (blue curve). **(C)** Chemical properties derived from analysis of raw data using Nanoscale (TA Instruments). The melting temperature was 57.85°C ± 0.31°C, enthalpy of 399.79 kJ ± 6.74 kJ, entropy of 6.91 kJ/K ± 0.08 kJ/K, and Delta G (ΔG) of 330.63 kJ ± 5.94 kJ.

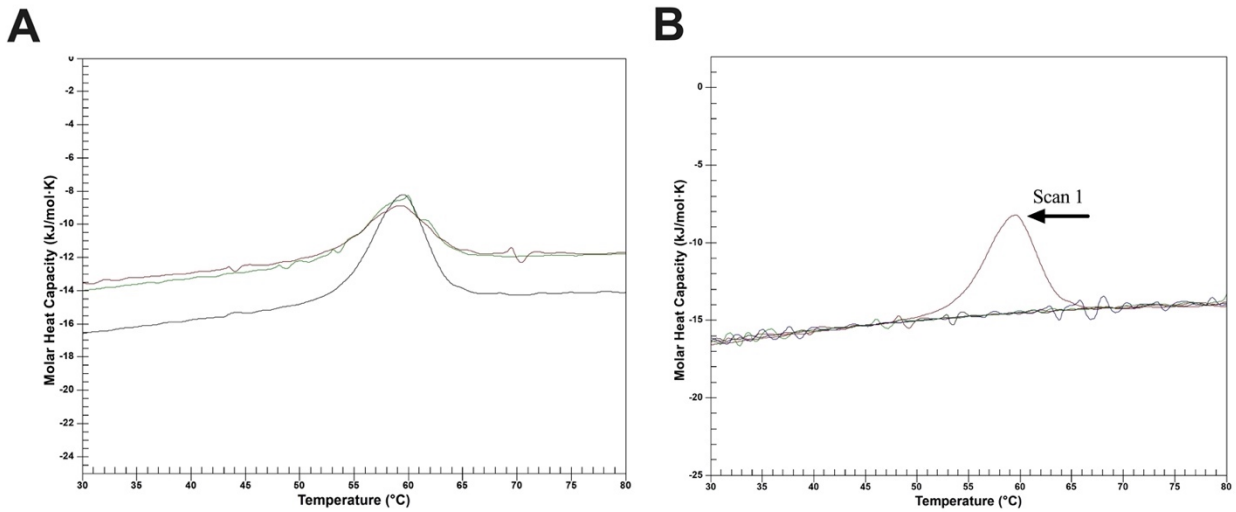

C

Δ14AIDA1b	Average	St. Dev.
T_m (°C)	59.36	0.07
Enthalpy (ΔH) (kJ)	486.10	41.89
Entropy (ΔS) (kJ/K)	8.18	0.69
Gibbs Free Energy (ΔG) (kJ)	404.21	34.93

Figure 4.11. DSC molar heat capacity profiles for Δ14AIDA1b. (A) Superimposition of three thermal denaturation scans for 100 µM Δ14AIDA1b in PBS. Molar heat capacity was measured by heating 1mL sample from 5°C to 85°C at a rate of 1°C/min. **(B)** Molar heat capacity profiles for ten sequential thermal denaturation's of Δ14AIDA1b, measured from 5°C to 85°C at a rate of 1°C/min. The first scan is marked by the black arrow (blue curve). **(C)** Chemical properties derived from analysis of raw data using Nanoscale (TA Instruments). The melting temperature was 59.36°C ± 0.07°C, enthalpy of 486.10 kJ ± 41.29 kJ, entropy of 8.19 kJ/K ± 0.69 kJ/K, and Delta G (ΔG) of 404.21 kJ ± 34.93 kJ.

4.4 Exon 14 contributes a secondary structure in AIDA1b

Secondary structure analysis was also done at 25°C to measure the molar ellipticity and investigate differences between AIDA1b and Δ14AIDA1b. Several buffer and concentration trials revealed optimal conditions to be 3.5 μM protein and 10mM sodium phosphate. As seen in Figure 4.12A, AIDA1b (blue) shows a dip at 208 nm characteristic of alpha helices. A similar result was seen for Δ14AIDA1b (red); however, the spectra was less defined and clean, even with identical concentrations. In the superimposition of both spectra's, seen in Figure 4.12C, AIDA1b displays lower mdeg values and more defined peaks however the overall trends, dips and peaks are highly similar.

Analysis of the raw results using BeStSel, presented a more definite picture of the potential secondary structures present in both proteins. AIDA1b, as seen in the raw CD spectra, is primarily composed of 53.7% α-helices. The other secondary structures shown in the BeStSel deconvolution was 34.4% right-twisted anti-parallel beta sheets, 3.2% parallel beta-sheets and 19.8% turns. These values are consistent with the AlphaFold predicted structure of AIDA1b. An identical deconvolution was done on the raw secondary structure analysis of Δ14AIDA1b, which differed from AIDA1b, since the secondary structure was largely composed by regions that were undetectable by CD. These regions classified as other can also include 3_{10} and π helices, or irregular loops/structures (Micsonai et al., 2018). However, it still has all the structures present in AIDA1b, 13.5% regular helix, 10.5% distorted helix, 4.6% right-twisted anti-parallel beta sheet, 4.6% parallel beta-sheet, and 8.5% turn. The new additions include 54% other and 4.3% relaxed anti-parallel beta-sheet.

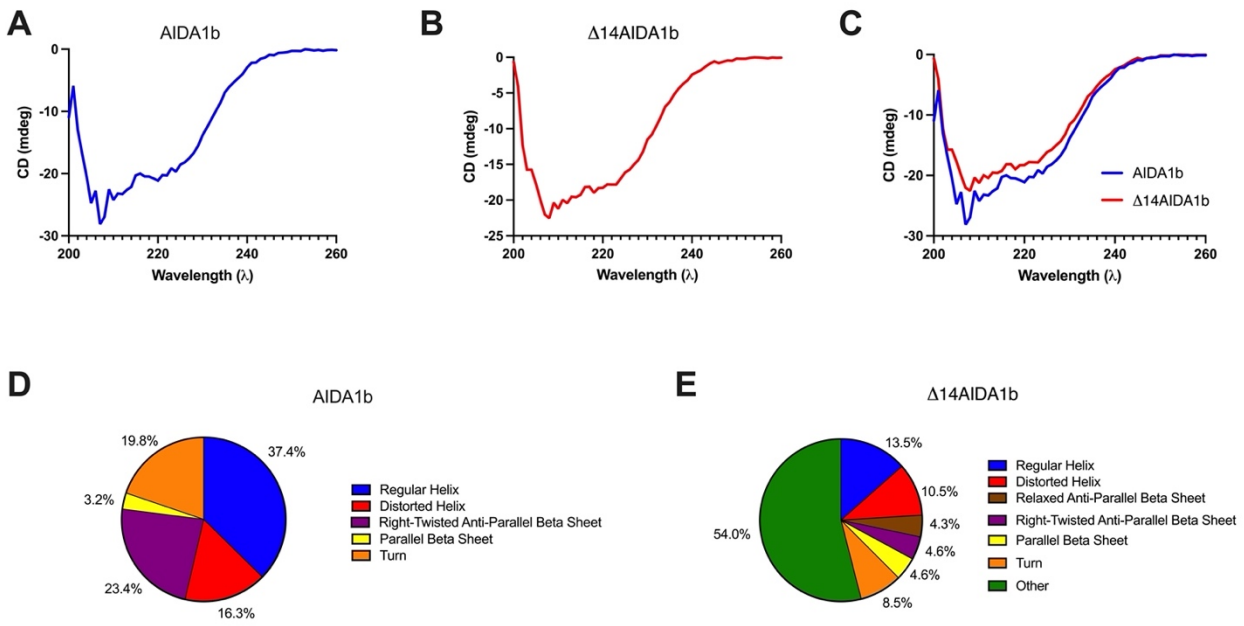

Figure 4.12. Analysis of AIDA1b and Δ14AIDA1b secondary structure using CD spectroscopy and BeStSel. (A) Secondary structure spectra for 3.5 µM AIDA1b with molar ellipticity measured over 200 – 260 nm at 22.0 °C. Results were normalized by subtracting the buffer (10 mM sodium phosphate – 7.5 mM Na_2HPO_4 and 2.4 mM NaH_2PO_4) spectrum. **(B)** Secondary structure spectra for 3.5 µM Δ14AIDA1b with molar ellipticity measured over 200 – 260 nm at 22.0 °C. Results were normalized by subtracting the buffer (10 mM sodium phosphate – 7.5 mM Na_2HPO_4 and 2.459mM NaH_2PO_4) spectrum. **(C)** Superimposition of AIDA1b and Δ14AIDA1b secondary structure spectra. All experiments were done on a J-815 CD Spectrometer (Jasco). **(D)** Data deconvolution using BeStSel analysis to identify key secondary structures present for AIDA1b, shown in percentages using a pie graph. Results confirmed primarily α-helices, with equal amounts of β-sheets and turns. **(E)** Data deconvolution using BeStSel analysis to identify key secondary structures present for Δ14AIDA1b, shown in percentages using a pie graph.

4.5 SEC-MALS-SAXS reveals similar 3D structures for AIDA1b and Δ14AIDA1b

4.5.1 SEC-SAXS models for AIDA1b

SEC-MALS-SAXS was done on AIDA1b and Δ14AIDA1b to determine a bead model for both proteins. The analysis for AIDA1b (Figure 4.13F) reveals an elongated protein, with a small extended region on either the N- or C-terminus. Further, the Guinier plot (Figure 4.13A) reveals an excellent r^2 (close to 1.00), along with an even distribution of points along the line. The radius of gyration, R_g, is the average scattering distance from the proteins centre-of-mass, which in this case, is 34.3 Å. The normalized residual plot (Figure 4.13B) is localized around 0,

which means possible aggregation or small MW contaminants, such as imidazole, are unlikely. The pairwise distribution function, P(r), illustrates the paired electron distances found in the sample. The function is bell-shaped (Figure 4.13C), indicating a globular protein, and the plot gradually reaches 0 at 145, which will be the D_{max}. The D_{max} is the maximum distance between an electron pair in the sample, essentially, the maximum "width" of the protein. A Kratky plot is used to determine the degree of folding in a sample. For AIDA1b, the Kratky plot (Figure 4.13D) reveals a folded structure due to the bell curve nature of the plot. Upon looking at the Chi^2 value, 0.82 and controlling the R_g provided by the P(r) and Guinier functions to be near identical, the software indicated a reasonable structure solution would be provided. Furthermore, with an ambiguity score of 0.69, the 3D reconstruction will likely be unique. This, combined with a predicted MW of 46.2kDa, reveals that the bead model will ideally be an accurate representation.

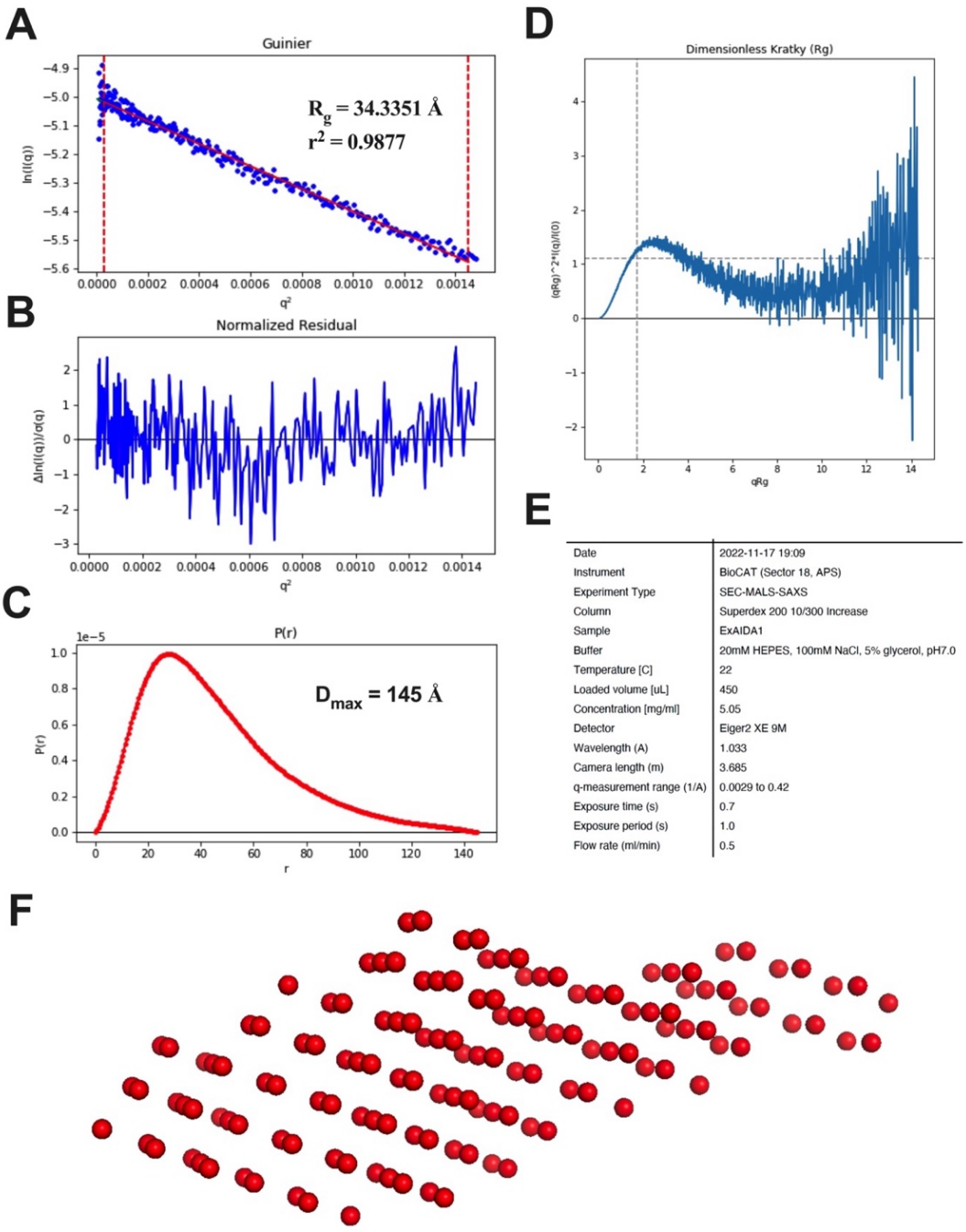

Figure 4.13. SEC-MALS-SAXS analysis on AIDA1b. (A) Linear Guinier model to display scattering intensity, with a r^2 of 0.98 and Rg = 34.33 Å. **(B)** Normalized residual from Guinier model shows random localization around 0 in a linear fashion, with slight upward curve, indicating potential aggregation. **(C)** Pairwise distribution function, P(r), plot showing a gradual approach to 0 at D_{max} = 1145 Å. **(D)** Kratky plot showing folded nature of sample due to bell curve shape. **(E)** Experimental parameters. **(F)** A bead model of AIDA1b constructed using DAMFF/N in RAW and displayed in pyMOL. The predicted MW was 46.2kDa. Figure created in GraphPad PRISM.

4.5.2 SEC-SAXS models for Δ14AIDA1b

Identical experimental parameters were used for Δ14AIDA1b. To begin, the Guinier plot (Figure 4.14A) reveals a better r^2 than AIDA1b, 0.9953, along with a closer distribution of data points to the line of best fit. The radius of gyration, R_g, is 29.423 Å, and since this protein is 2.5kDa smaller than AIDA1b, it is plausible that the average distance from the centre of mass will also be slightly reduced. Moreover, the normalized residual plot (Figure 4.14B) is again localized around 0. The P(r) function (Figure 4.13C) is bell-shaped, again indicating a globular protein, and the plot gradually reaches 0 at 124, the D_{max}. Similar to above, since Δ14AIDA1b is missing 25 residues, the maximum "width" of the protein is also possibly reduced, since it might be missing a key aspect of its 3D structure. The Kratky plot (Figure 4.14D) Δ14AIDA1b confirms a folded structure due to the bell curve nature of the plot. Upon looking at the Chi^2 value, 0.8345 and controlling the R_g provided by the P(r) and Guinier functions to be near identical, the software indicated a reasonable structure solution would be provided. Furthermore, with an ambiguity score of 1.568, the 3D reconstruction will potentially be unique. This, combined with a predicted MW of 44.4kDa, reveals that the bead model will ideally be an accurate representation.

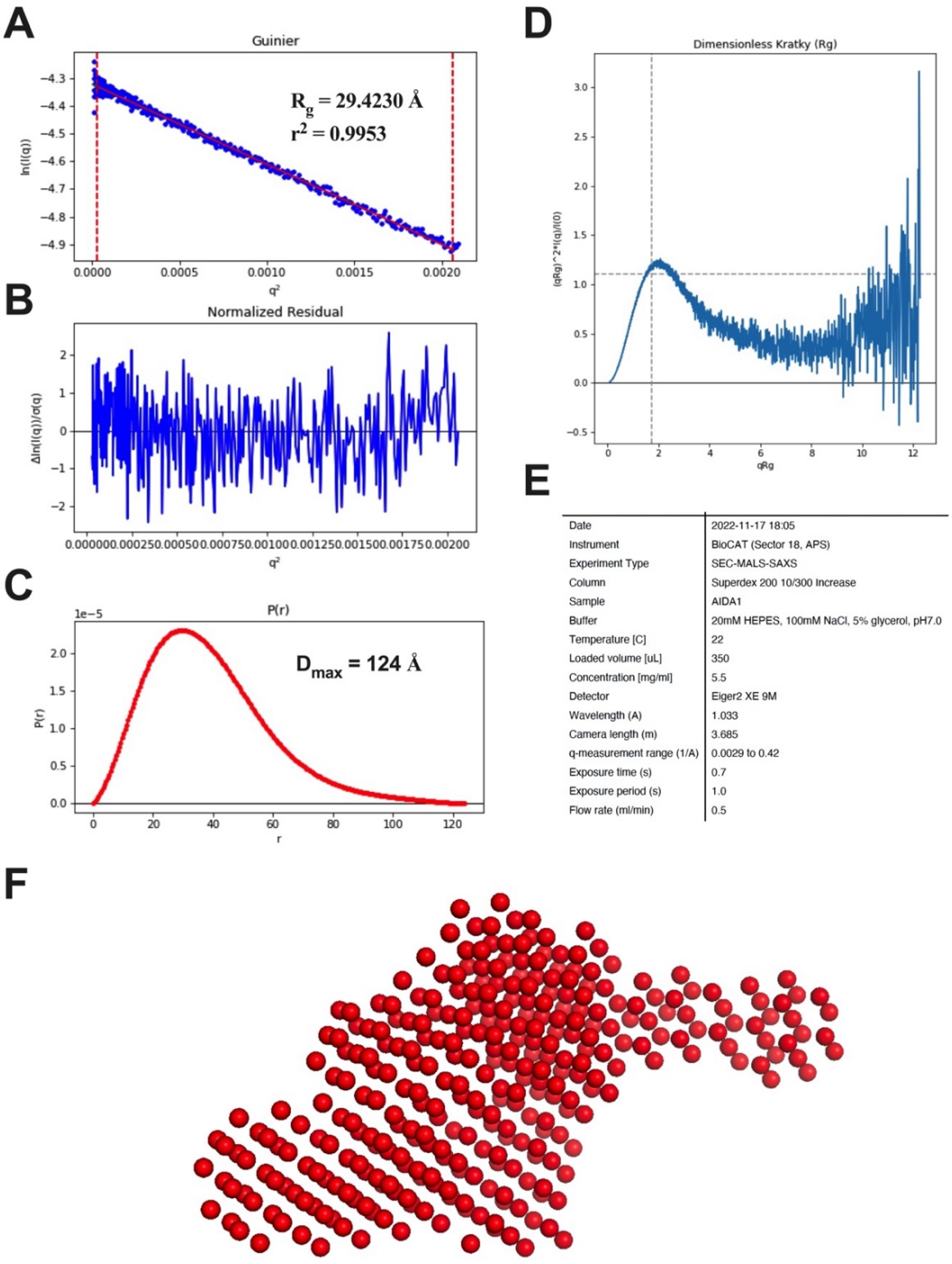

Figure 4.14. SEC-MALS-SAXS analysis on Δ14AIDA1b. (A) Linear Guinier model to display scattering intensity, with a r^2 of 0.995 and Rg = 29.4 Å. **(B)** Normalized residual from Guinier model shows random localization around 0 in a linear fashion. **(C)** Pairwise distribution function, P(*r*), plot showing a gradual approach to 0 at D_{max} = 124 Å. **(D)** Kratky plot showing folded nature of sample due to bell curve shape. **(E)** Experimental parameters. **(F)** A bead model of Δ14AIDA1b constructed using DAMFF/N in RAW and displayed in PyMOL. The predicted MW was 44.4kDa. Figure created in GraphPad PRISM.

4.5.3 Alignment of AIDA1b bead model to previously solved structures

To assess the accuracy of the bead model, and get a better overall structure, it was aligned to the AlphaFold predicted structure and previously solved domains. The predicted AlphaFold structure, using Uniprot Q7Z6G8, has Exon 14 as an α-helix, attached to the SAM domain tandem using an unstructured loop. This leads into the PTB domain using another unstructured loop. Using the CIFSUP tool in RAW, the bead model was reconstructed with alignment to the AlphaFold predicted structure, shown in Figure 4.15A. The resolved model showed a slightly compact model where the ridges follow the two domains, apart from the unstructured loop between the SAM domain tandem and PTB domain. The bead model was also fit with the PDB solution structures for the PTB domain (PDB: 2M38) and SAM1SAM2 domain tandem (PDB: 2KIV) in pyMOL. Although the orientation for the alignment was different than the AlphaFold alignment, they still fit reasonably well in the 3D model. The N-terminal end did not have any structures fitted; however, this is likely because it would contain Exon 14.

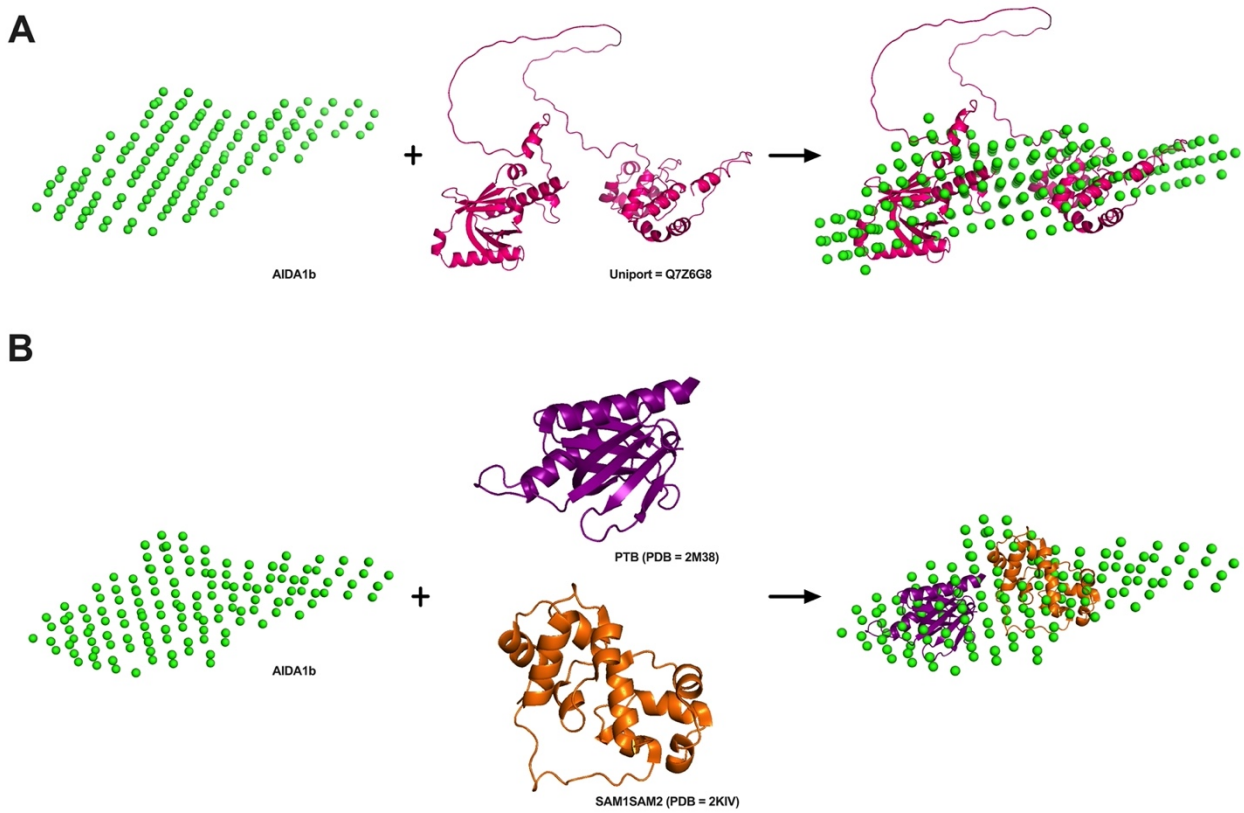

Figure 4.15. Alignment of AIDA1b bead model to AlphaFold and PDB structures. (A) Refinement of AIDA1b bead model, green, using alignment to AlphaFold predicted structure, pink. The DAMFF/N tool in RAW was used. Uniprot: Q7Z6G8. **(B)** Manual alignment of AIDA1b bead model, green, using previously solved PTB (PDB: 2M38), purple, and SAM1SAM2 (PDB: 2KIV), orange, domain solution structures. PyMOL was used to overlay the structures. Figure created in GraphPad PRISM.

4.5.4 Alignment of Δ14AIDA1b bead model to previously solved structures

Similar to above, the bead model for Δ14AIDA1b was aligned to the AlphaFold predicted structure and previously solved domains to acquire a more accurate output. The predicted AlphaFold structure, using Uniprot ID Q7Z6G8, is missing the unstructured loop and Exon 14 α-helix at the N-terminus. However, the SAM domain tandem, connected to the PTB domain using an unstructured region is conserved in both predicted constructions. Using the DAMMIF/N tool in RAW, the bead model was reconstructed with alignment to the AlphaFold predicted structure, shown in Figure 4.15A. The resolved model showed a slightly compact model where the ridges follow the two domains, apart from the unstructured loop between the

SAM domain tandem and PTB domain. The bead model was also manually fit with the PDB solution structures for the PTB domain (PDB: 2M38) and SAM1SAM2 domain tandem (PDB: 2KIV) in PyMOL. Although the orientation for the alignment was different than the AlphaFold alignment, they still fit reasonably well in the 3D model. Similar to AIDA1b, the N-terminal end has a slight extension which is not accounted for by manual superimposition. However, that extension is eliminated in Figure 4.16A, after alignment with the predicted AlphaFold structure.

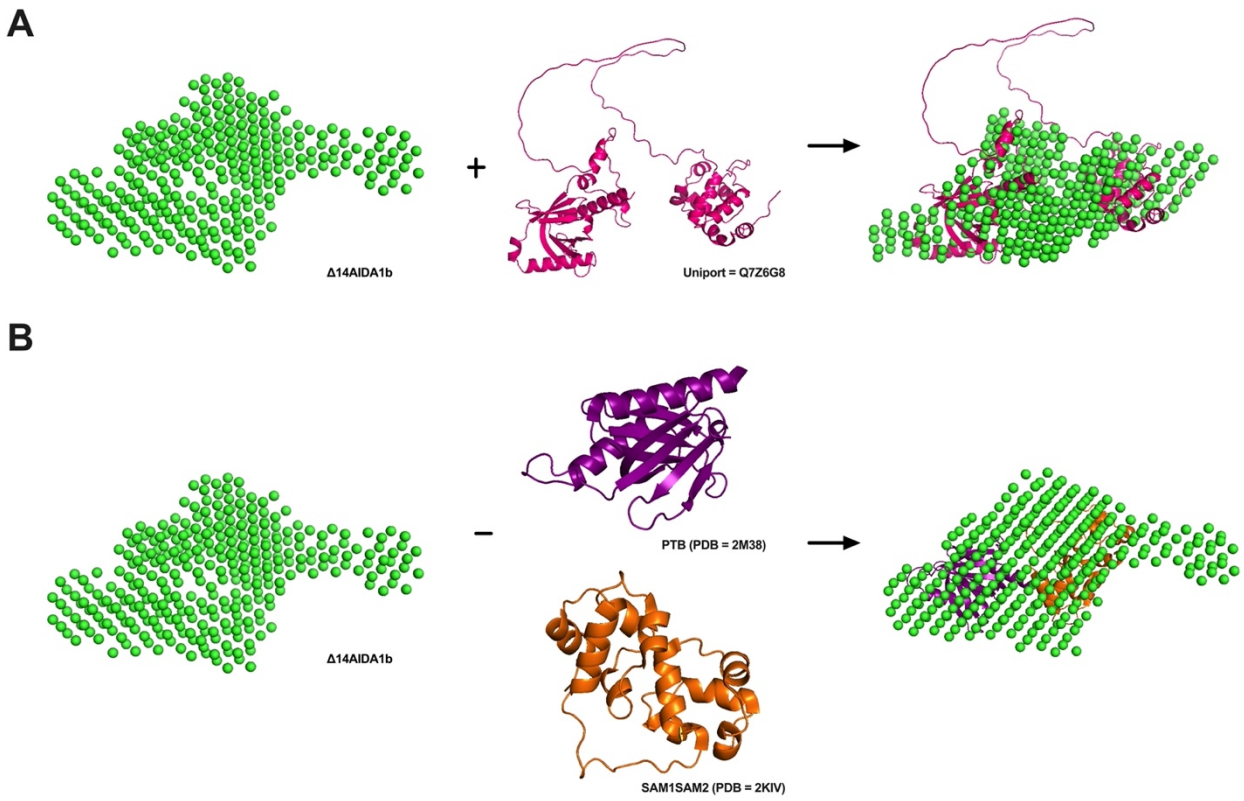

Figure 4.16. Alignment of Δ14AIDA1b bead model to AlphaFold and PDB structures. (A) Refinement of Δ14AIDA1b bead model, green, using alignment to AlphaFold predicted structure, pink. The DAMFF/N tool in RAW was used. Uniprot: Q7Z6G8. **(B)** Manual alignment of Δ14AIDA1b bead model, green, using previously solved PTB (PDB: 2M38), purple, and SAM1SAM2 (PDB: 2KIV), orange, domain solution structures. PyMOL was used to overlay the structures. Figure created in GraphPad PRISM.

4.5.5 Superimposition of AIDA1b and Δ14AIDA1b bead models

To compare the structure of both proteins, the CIFSUP ASTRA extension was used to superimpose the bead models (Figure 4.17C and Figure 4.17D). Figure 4.17C shows the raw beads models superimposed, whereas Figure 4.17D is superimposition after alignment with the predicted AlphaFold structures. The result showed a very similar structure for both proteins in a 3D space, with the key difference being a small extended region on AIDA1b. This can be explained by structural due to presence of Exon 14. A direct explanation would be that Exon 14 is present at the N-terminus of this protein, and thus, that portion is now missing from the mutant, causing it to be slightly smaller.

An SDS-PAGE gel to verify the protein size in relation to each other is shown in Figure 4.15B. Δ14AIDA1b, lane 3, is 2.8kDa smaller than AIDA1b, lane 2, which is visible when comparing to the ladder, lane 1. The protein sequence for AIDA1b, Figure 4.17A, is composed of 420 residues, including the 25 amino acid sequence for Exon 14. The Exon 14 sequence, shown in red (Figure 4.15C), is primarily amphipathic, with an equal number of hydrophilic and hydrophobic residues.

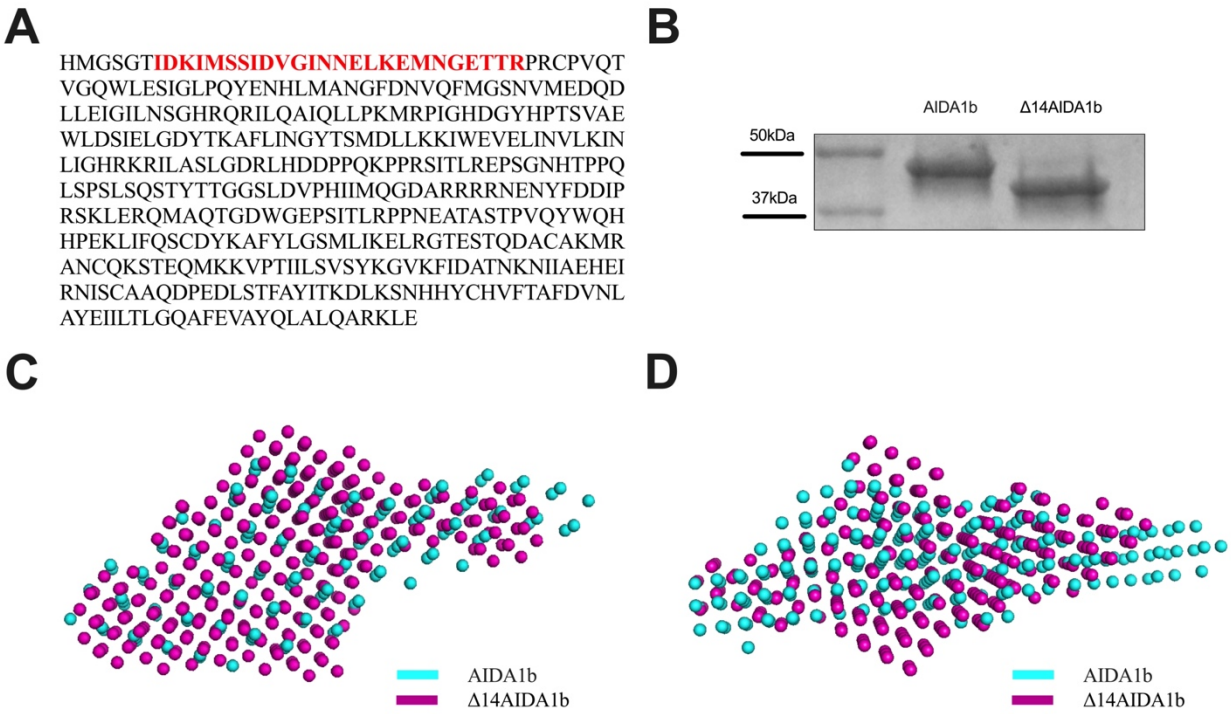

Figure 4.17 Superimposition of AIDA1b bead models. (A) Amino acid sequence for AIDA1b, with Exon 14 coloured in red. Exon 14 is deleted in Δ14AIDA1b. **(B)** SDS-PAGE for size comparison of AIDA1b, 47.5 kDa, and Δ14AIDA1b, 44.7 kDa. **(C)** Superimposition of AIDA1b, blue, and Δ14AIDA1b, pink, using cifsup ASTRA extension. **(D)** Superimposition of refined AIDA1b, blue, and Δ14AIDA1b, pink, bead models after alignment with AlphaFold predicted structures.

4.5.6 SEC-MALS analysis for AIDA1b and Δ14AIDA1b

The SEC-MALS data was analyzed concurrently with the SAXS data to provide an accurate model of AIDA1b structure and oligomerization using ASTRA 7 software. The results revealed that AIDA1b was predicted to have a molecular weight (MW) of 47.25kDa ± 0.02300%, which is near the MW predicted by Expasy, 47.4kDa. The $R^2 = 0.4266$, likely lower because of small MW aggregates at earlier time frames and the inherent inaccuracy of small angle diffractors. The hydrodynamic radius was 4.03nm ± 0.0600nm, with a higher $R^2 = 0.9981$. On the other hand, Δ14AIDA1b was shown to have a MW of 42.02kDa ± 0.01200%, which is slightly lower than the Expasy predicted of 44.6kDa. However, the hydrodynamic radius for both proteins was quite similar because Δ14AIDA1b's was 4.01nm ± 0.0600nm. This reaffirms the accuracy of both models since a deletion of 25 amino acids should not cause an astronomical change in MW or hydrodynamic radius. In addition, this confirms that AIDA1b likely exists in monomeric form.

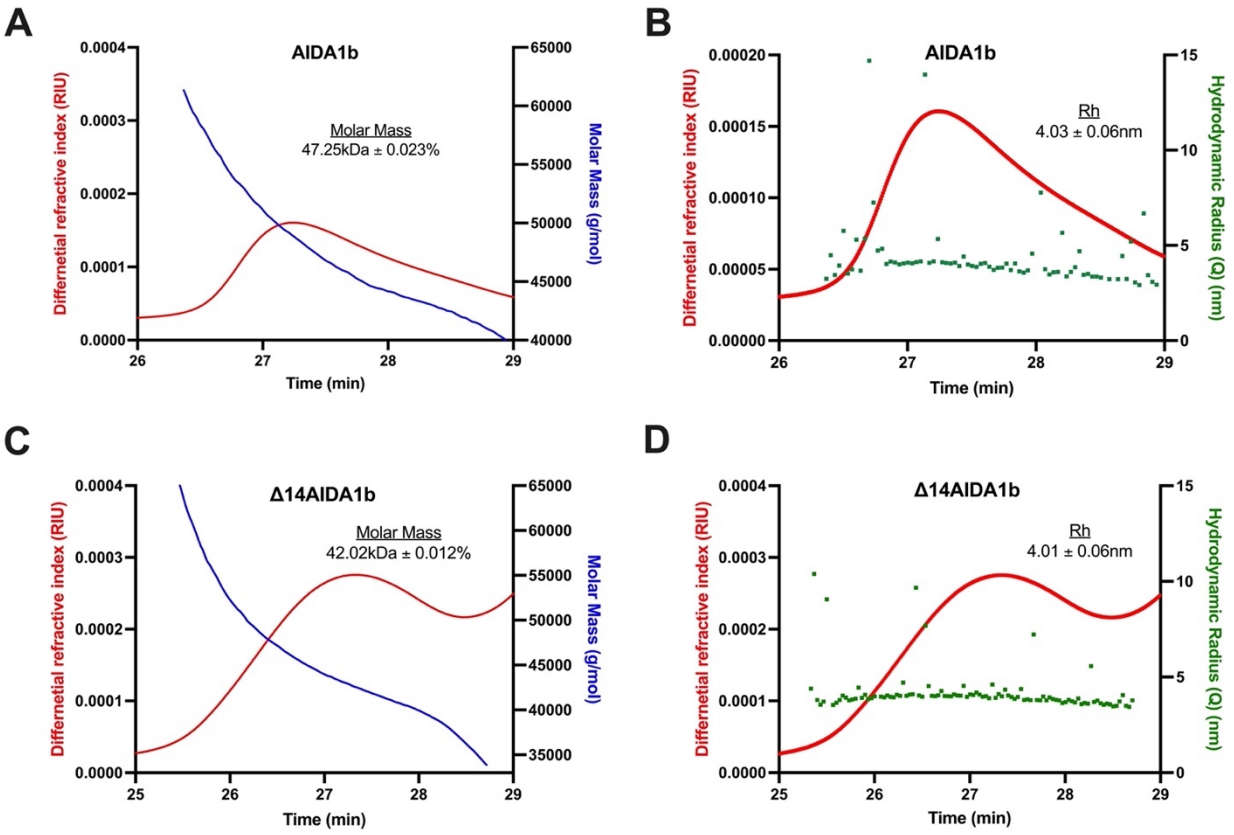

Figure 4.18 SEC-MALS determination of AIDA1b and Δ14AIDA1b structural parameters. **(A)** Molar mass determination reveals a predicted molecular weight of 47.25kDa ± 0.023% for AIDA1b upon plotting of differential refractive index (RIU), red, and derived molar mass (g/mol), blue. **(B)** The hydrodynamic radius was solved to be 4.03nm ± 0.06nm, upon plotting of differential refractive index (RIU), red, and derived molar mass (g/mol), green for AIDA1b. **(C)** The molar mass of Δ14AIDA1b was experimentally determined to be 42.02kDa ± 0.012%, with the plot showing differential refractive index (RIU), red, and derived molar mass (g/mol), blue. **(D)** Hydrodynamic radius of Δ14AIDA1b was 4.01nm ± 0.06nm after plotting of differential refractive index (RIU), red, and derived molar mass (g/mol), green. Experimental data was analyzed in ASTRA 7 (Wyatt) and plotted using GraphPad PRISM.

CHAPTER 5: DISCUSSION

5.1 AIDA1b is autoinhibited by Exon 14

There are several hypotheses that have been presented since the discovery of AD to explain its progression, development, and origin. These include: the amyloid hypothesis, cholinergic hypothesis, Tau propagation hypothesis, mitochondrial cascade hypothesis, neurovascular hypothesis, etc (Liu et al., 2019). Although no hypothesis has been proven to be the sole initiator of AD, there have been promising results shown in clinical trials. AIDA1, although not directly implicated with AD, has been shown to interact with APP, apart from one isoform – AIDA1b. For example, AIDA1a has been highly found in the nucleus, however, upon transfection with AICD of APP it colocalizes to the cytoplasm (Ghersi et al., 2004). In a similar sense, understanding AIDA1b's lack of interaction with APP can be vital to AD hypotheses. As a result, this thesis used fluorescence anisotropy and biolayer interferometry to investigate autoinhibitory properties of Exon 14 against the PTB domain.

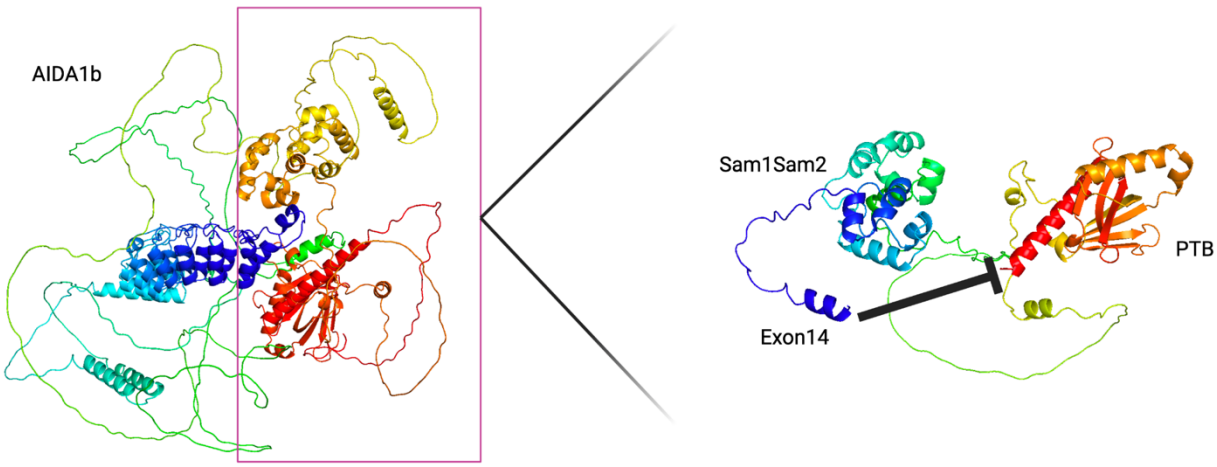

Figure 5.1 Schematic of AIDA1b auto-inhibition. Enlarged structural image of AIDA1b (Uniprot #Q7Z6G8), to show hypothesized structural inhibition of PTB domain using Exon 14. Structures visualized in pyMOL using a rainbow colour scheme (blue = N-Terminus, red = C-terminus), and figure created in BioRender.

The FA and BLI provided a preliminary confirmation that Exon 14 was directly causing, or at least involved in, the inability of AIDA1b to bind APP using its PTB domain. Previous work by the Donaldson laboratory showed that Exon 14 peptides, fusions of Exon 14 to the adjacent SAM domains and fusions of Exon 14 directly to the PTB domain were insufficient to inhibit the PTB domain. In the latter case, a comparison of PTB ^{1}H-^{15}N HSQC spectra with Exon 14-PTB domain spectra did show some minor chemical shift changes suggesting that Exon 14 on its own may weakly contact the PTB domain. In AIDA1b's primary structure, Exon 14 is present at the N-terminus of the SAM1SAM2 domain tandem, however, it is predicted that in the tertiary/quaternary structure, Exon 14 can interact with or block the PTB interaction site. Using the folded proteins, the PTB domain independently bound APP peptides with a K_d of 7.5 μM using FA and 5.8 μM using BLI. Although this is not as strong as some widely known protein-protein interactions, it can be considered moderate affinity. Like the PTB domain alone, Δ14AIDA1b also showed binding to APP, with a K_d = 12.5 μM for FA and 7.8 μM for the BLI.

Exon 14 encodes a 25 amino acid sequence, IDKIMSSIDVGINNELKEMNGETTR, with 12 hydrophobic and 13 hydrophilic residues. The amphipathic nature of this region can make it hard to predict how it may interact with PTB, however, surface exposed and buried residues can be predicted. It is also possible that Exon 14 does not directly engage with the PTB, meaning that there is no binding interaction happening, rather, the 3-dimensional folding of AIDA1b lends it to blocking the PTB active site. For example, the X11/Mint1 adaptor proteins are also binders of APP, as discussed in the introduction (Matos et al., 2012). However, they can also be autoinhibited from partaking in APP binding due to an C-terminal α-helical linker that folds back into the PTB domain (Matos et al., 2012).

APP has a YENPTY sequence that is used to interact with PTB, and such residues are missing from Exon 14. In experimentally determined PTB-APP complexes and AlphaFold models of the AIDA1b PTB-APP complex, the APP ligand adopts a β-strand configuration to complement the β-sheet in the PTB domain. In contrast, the first ten amino acids of Exon 14 are predicted to form an amphipathic α-helix.

Some AlphaFold models position a helical Exon 14 in the same position as a canonical YENPTY ligand possibly due to the way AlphaFold was trained on sequences. Contacts between the helical Exon 14 segment and the PTB domain in the model are not as extensive as a YENPTY ligand suggesting that other sequences in Exon 19 for example, may also contribute to a steric blocking of the APP binding cleft.

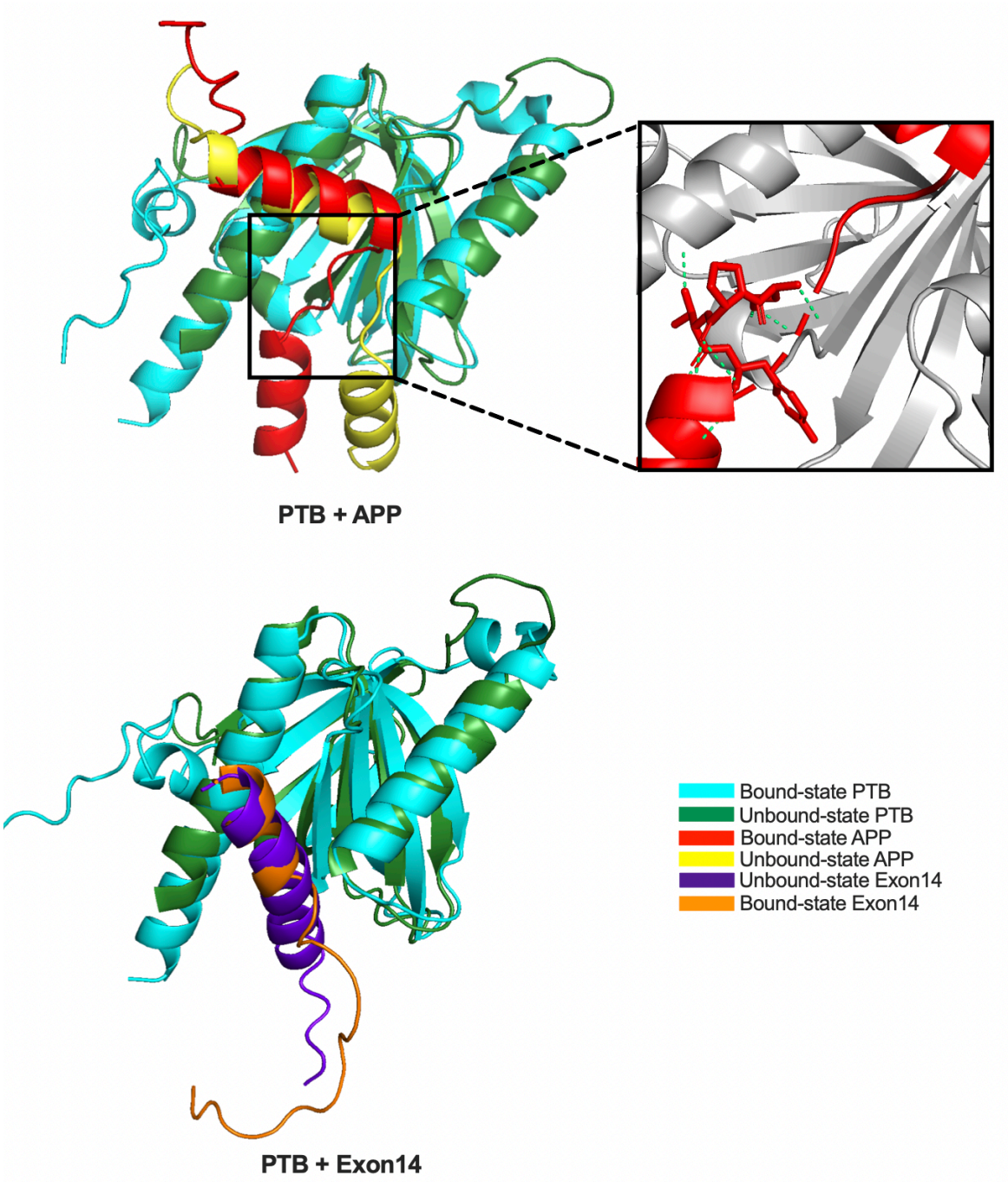

Figure 5.2. Predicted complex formation of the PTB domain with APP and Exon 14. AlphaFold Multimer was used to computationally predict the binding complex of PTB with APP, and PTB with Exon 14, with unbound structures superimposed. An enlarged image of the NPTY motif, vital for PTB-APP binding, is shown in stick form with hydrogen bonds shown in lime green. No polar or nonpolar contacts were found for the Exon 14 and PTB complex. A legend is provided in the bottom right. PTB (PDB: 2M38), APP (Uniprot: P05067), and Exon 14 (Uniprot: Q7Z6G8). Structures were visualized in pyMOL, and figure was created in GraphPad Prism.

5.2 The stability of AIDA1b is not significantly impacted by Exon 14

The thermostability of AIDA1b protein fragments was assayed using DSF, CD, and DSC. On average, the T_m across all buffer species was ~59 – 60 °C, with the exception being [50 mM MES, 100 mM NaCl, pH 5.5]. Since another buffer condition already had 50mM MES and 100 mM NaCl, it is reasonable to conclude that the pH was the largest impact factor in reducing AIDA1b and Δ14AIDA1b stability. As the T_m was about 8 °C less than its counterpart with pH 6, a plausible explanation is that a pH of 5.5 is almost a 10^1-decrease compared to the respective pI's of AIDA1b, 6.17, and Δ14AIDA1b, 6.40. The >1 unit decrease in buffer pH likely caused the protein to be charged, rather than neutral. The overall positive charge can influence ionizable groups, implicating key bonding interactions that aid in protein tertiary and quaternary structure (Russell & Warshel, 1985). The buffers with notable differences between AIDA1b and Δ14AIDA1b T_m were [50mM MOPS, pH 7], [50mM sodium citrate, pH 7], [50mM sodium citrate, pH 8], [50mM Tris, pH 8] and PBS, with all buffers having 100mM NaCl. The most notable difference between AIDA1b and Δ14AIDA1b, where there is a ~4°C increased T_m for Δ14AIDA1b ($p < 0.0001$) is PBS. The key addition to PBS would be phosphates, which the other buffer conditions lack. The presence of phosphate is believed to reduce unfavourable interactions between like-charges, which essentially allows for increased number of surface-exposed residue conformations (Fayos et al., 2005). By optimizing charge distribution, it allows for improved solvation of the protein (Fayos et al., 2005). The addition of all buffers that were pH 8 again reinforces the impact of pH on the stability of AIDA1b. A pH of 8 is >1 unit higher than the predicted pI's of these proteins, which would render them negatively charged and potentially cause unfavourable interactions between charged residues. Overall, there is no significant change in the thermostability AIDA1b after Exon 14 deletion because no protein is

consistently higher in each buffer condition. Rather, each protein has its own ideal buffer condition, and there is no pattern for which protein is found to be higher in T_m. This would suggest that the 25-residue sequence does not engage in interactions or structures that play a prominent role in the thermostability of AIDA1b.

The results of the CD study showed an identical melting point for both proteins, again, reinforcing the conclusion that Exon 14 does no play a significant role in the thermostability of AIDA1b. The DSC study concurred with the CD study with a T_m of 57.85 ± 0.31°C for AIDA1b and 59.36°C ± 0.07°C for Δ14AIDA1b. Although the difference in T_m with and without Exon 14 is significant in PBS, the DSF results have shown this trend is not conserved across buffer conditions, thus, it would be inaccurate to conclude that Exon 14 significantly decreases the thermostability of AIDA1b. The enthalpy changes in the AIDA1b unfolding reaction was 399.79 kJ ± 6.74 kJ with Exon 14 and 486.10 kJ ± 41.29 kJ without Exon 14. The enthalpy change, ΔH, refers to quantifying the heat change in the endothermic process of breaking non-covalent bonds in the protein (Gill et al., 2010). It is known that a larger protein will typically have a greater enthalpy change due to having more bonds, however, it is also possible that a protein is partially unfolding before its denaturation is measured (Gill et al., 2010). As such, it is plausible that Δ14AIDA1b is more stable since it is a smaller protein but, requires a greater amount of energy to unfold. Similarly, the entropy, ΔS, and ΔG are both higher for Δ14AIDA1b, which represents a greater number of conformations available due to higher disorder of the protein in PBS (Bigman & Levy, 2020). These results combined can conclude that the removal of Exon 14 makes AIDA1b more thermodynamically stable, however, it is exclusive to PBS buffer.

5.3 AIDA1b structure is largely conserved regardless of Exon 14 presence or absence

Another application of CD is acquiring data that resolves the secondary structure of a protein. In this case, AIDA1b and Δ14AIDA1b molar ellipticity was measured across the far UV spectral range. To get a better understanding of the secondary structure, the raw data was deconvoluted in BeStSel. The provided spectra showed a 53.7% total composition of α-helices, which is consistent with the AlphaFold structural prediction of AIDA1b. Furthermore, there is a small percentage of β-sheets, 26.6%, which, again, is consistent with the predicted and solved AIDA1b domain structures of the PTB domain and SAM1SAM2 domain tandem. This would also confirm that the AlphaFold prediction can be improved due to the several disordered regions shown, whereas the CD analysis shows measurable structures in the whole protein. On the other hand, the secondary structure of Δ14AIDA1b still showed a dominant percentage of α-helices, albeit half of that compared to AIDA1b. Moreover, the percentage of β-sheets is nearly identical, but there is a novel addition of "other". The other in this case can refer to irregular loops, 3_{10} helix, bends, π-helix, and β-bridges (Micsonai et al., 2018). These structures refer to regions that are possibly not detectable or resolvable by CD (Micsonai et al., 2018). Overall, the CD spectra suggest that the secondary structures of AIDA1b and Δ14AIDA1b are similar since there is only 25 amino acids difference between the two proteins. Exon 14 may contribute a helix, but it does not appear to contribute to any major global secondary structural changes.

SEC-MALS-SAXS was used to determine a low resolution 3D structure for AIDA1b and Δ14AIDA1b. SEC, refers to size-exclusion chromatography that is performed before small-angle x-ray scattering (SAXS) (Ogawa & Hirokawa, 2018). MALS (multi-angle light scattering) provides an independent assessment of the protein molecular weight and potential oligomerization (Ogawa & Hirokawa, 2018). A Guinier fit of the SAXS dataset provides

information about the quality of the data and the radius of gyration, R_g. With a qR_g of ~1.3, AIDA1b and Δ14AIDA1b are both predicted to have globular characteristics. The derived normalized residuals, although localized around 0, appear to show a slight upward turn which is indicative of aggregation. This compliments the previous conclusion about AIDA1b being unstable, and easily aggregating in non-optimal conditions. There was no downward curve in the Guinier fit and normalized residuals that would indicate interparticle interactions and repulsions. The bell-shaped curve of the P(r) function and Kratky plot indicate AIDA1b was folded and globular during data collection. The bead model shows a slightly elongated model, with a slight protrusion at the predicted N-terminus. After alignment to the AlphaFold predicted structure, Figure 4.16A, the two domains, PTB and SAM1SAM2 tandem, fit reasonably well, apart from the unstructured linker region. Thus, it is plausible that since the linker region is unsolved, AlphaFold is unable to make an accurate prediction about its structure due to a lack of homologs. Instead, the PTB and SAM tandem structures were modeled into the SAXS determined volume.. Since SEC-MALS-SAXS is done in solution, the protein is rotating, and thus, some extensions seen in the bead model, may be representative of the dynamic protein.

From the SAXS analysis of Δ14AIDA1b, the normalized residuals show no upward or downward trend, eliminating risk of aggregation or interparticle repulsion. Similar to the R_g, the D_{max} is also smaller, only 124 Å, which would be supported by the fact that Exon 14 is deleted at the N-terminus and may be an extended/disordered region. Since the P(r) and Kratky plots confirm a folded and globular sample, the bead model is likely an accurate representation of Δ14AIDA1b in solution. Manual fitting with the solution structures of the PTB domain and SAM domain tandem was not achieved possibly due to the dynamic linkers found between these domains.

The variation between the AIDA1b and Δ14AIDA1b bead models can also possibly be due to alterations in three-dimensional folding caused by the presence or absence of Exon 14. For example, the absence of Exon 14 may be causing alterations in intramolecular bonding, which changes how the PTB domain and SAM1SAM2 domain tandem are folded relative to each other. A detailed structural analysis would provide insight to whether variations in folding truly exist, and how it possibly impacts the autoinhibition of AIDA1b.

CHAPTER 6: CONCLUSIONS AND FUTURE WORK

AIDA1 is present in the cerebral cortex and hippocampus, suggesting a role in the development of memory, and learning systems (Carbonell et al., 2019). Most notably, AIDA1 is known to interact with the AICD peptide of APP, a protein hypothesized to be the foundation for AD development. Since AIDA1b is the lone isoform unable to interact with APP, it can provide insight into perhaps regulating abnormal APP cleavage. This suggests that molecular studies of AIDA1 are necessary to fill knowledge gaps in our understanding of neurodegenerative disease.

This thesis investigated the structural and functional properties of AIDA1b, the only isoform that retains Exon 14. The use of fluorescence anisotropy and biolayer interferometry provided detailed insight to the role of Exon 14 in the auto-inhibition of AIDA1b. Since APP is a protein partner, AIDA1b can plausibly be involved in the amyloid precursor hypothesis of AD. Furthermore, the use of CD, DSC, and DSF aided in concluding that although Exon 14 provides an important functional role, it does not play a role in the thermal or chemical stability of AIDA1b. A follow up SAXS study also supports this conclusion, in a structural context.

This thesis work may be extended by further deletion analysis to determine if the SAM domains and the sequence encoded by Exon 19 partner with Exon 14 to achieve inhibition of the PTB domain. By identifying the minimal number of determinants for the inhibition of the PTB domain, the possibility of determining a high-resolution structure by NMR or X-ray methods increases. Exon 14 may be subjected to a substitution analysis to determine which amino acids contribute to inhibition. Since the way in which Exon 14 contributes to PTB domain inhibition is novel, a high-resolution structure will have significant impact on the structural biology field.

CHAPTER 7: REFERENCES

Aasland, R., Abrams, C., Ampe, C., Ball, L. J., Bedford, M. T., Cesareni, G., Gimona, M., Hurley, J. H., Jarchau, T., Lehto, V.-P., Lemmon, M. A., Linding, R., Mayer, B. J., Nagai, M., Sudol, M., Walter, U., & Winder, S. J. (2002). Normalization of nomenclature for peptide motifs as ligands of modular protein domains. *FEBS Letters*, *513*(1), 141–144. https://doi.org/10.1016/S0014-5793(01)03295-1

Ando, K., Iijima, K., Elliott, J. I., Kirino, Y., & Suzuki, T. (2001). Phosphorylation-dependent Regulation of the Interaction of Amyloid Precursor Protein with Fe65 Affects the Production of β-Amyloid. *Journal of Biological Chemistry*, *276*(43), 40353–40361. https://doi.org/10.1074/jbc.M104059200

Armstrong, D. M., Ikonomovic, M. D., Sheffield, R., & Wenthold, R. J. (1994). AMPA-selective glutamate receptor subtype immunoreactivity in the entorhinal cortex of non-demented elderly and patients with Alzheimer's disease. *Brain Research*, *639*(2), 207–216. https://doi.org/10.1016/0006-8993(94)91732-9

Aviv, T., Lin, Z., Lau, S., Rendl, L. M., Sicheri, F., & Smibert, C. A. (2003). The RNA-binding SAM domain of Smaug defines a new family of post-transcriptional regulators. *Nature Structural & Molecular Biology*, *10*(8), 614–621. https://doi.org/10.1038/nsb956

Bar-Sagi, D., Rotin, D., Batzer, A., Mandiyan, V., & Schlessinger, J. (1993). SH3 domains direct cellular localization of signaling molecules. *Cell*, *74*(1), 83–91. https://doi.org/10.1016/0092-8674(93)90296-3

Beer, S., Simins, A. B., Schuster, A., & Holzmann, B. (2001). Molecular cloning and characterization of a novel SH3 protein (SLY) preferentially expressed in lymphoid cells. *Biochimica et Biophysica Acta (BBA) - Gene Structure and Expression*, *1520*(1), 89–93. https://doi.org/10.1016/S0167-4781(01)00242-1

Biederer, T., Cao, X., Südhof, T. C., & Liu, X. (2002). Regulation of APP-Dependent Transcription Complexes by Mint/X11s: Differential Functions of Mint Isoforms. *The Journal of Neuroscience*, *22*(17), 7340–7351. https://doi.org/10.1523/JNEUROSCI.22-17-07340.2002

Bigman, L. S., & Levy, Y. (2020). Entropic Contributions to Protein Stability. *Israel Journal of Chemistry*, *60*(7), 705–712. https://doi.org/10.1002/ijch.202000032

BioRender (2020). Progression of Parkinson's Disease in the Substantia Nigra.

BioRender (2022). Cleavage of Amyloid Precursor Protein (APP)

Blaikie, P., Immanuel, D., Wu, J., Li, N., Yajnik, V., & Margolis, B. (1994). A region in Shc distinct from the SH2 domain can bind tyrosine-phosphorylated growth factor receptors. *The Journal of Biological Chemistry*, *269*(51), 32031–32034.

Blennow, K., De Leon, M. J., & Zetterberg, H. (2006). Alzheimer's disease. *The Lancet*, *368*(9533), 387–403. https://doi.org/10.1016/S0140-6736(06)69113-7

Blin, J., Baron, J. C., Dubois, B., Crouzel, C., Fiorelli, M., Attar-Lévy, D., Pillon, B., Fournier, D., Vidailhet, M., & Agid, Y. (1993). Loss of brain 5-HT $_2$ receptors in Alzheimer's disease: *In vivo* assessment with positron emission tomography and (^{18})setoperone. *Brain*, *116*(3), 497–510. https://doi.org/10.1093/brain/116.3.497

Blomberg, F., Cohen, R., & Siekevitz, P. (1977). The structure of postsynaptic densities isolated from dog cerebral cortex: II. characterization and arrangement of some of the major proteins within the structure. *Journal of Cell Biology*, *74*(1), 204–225. https://doi.org/10.1083/jcb.74.1.204

Boeckers, T. M. (2006). The postsynaptic density. *Cell and Tissue Research*, *326*(2), 409–422. https://doi.org/10.1007/s00441-006-0274-5

Bongirwar, V., & Mokhade, A. S. (2022). Different methods, techniques and their limitations in protein structure prediction: A review. *Progress in Biophysics and Molecular Biology*, *173*, 72–82. https://doi.org/10.1016/j.pbiomolbio.2022.05.002

Borg, J.-P., Ooi, J., Levy, E., & Margolis, B. (1996). The Phosphotyrosine Interaction Domains of X11 and FE65 Bind to Distinct Sites on the YENPTY Motif of Amyloid Precursor Protein. *Molecular and Cellular Biology*, *16*(11), 6229–6241. https://doi.org/10.1128/MCB.16.11.6229

Breeden, L., & Nasmyth, K. (1987). Similarity between cell-cycle genes of budding yeast and fission yeast and the Notch gene of Drosophila. *Nature*, *329*(6140), 651–654. https://doi.org/10.1038/329651a0

Brown, J. H., Bihoreau, M.-T. G. A., Hoffmann, S., Kra[Combining Diaeresis]nzlin, B., Tychinskaya, I., Obermu[Combining Diaeresis]ller, N., Podlich, D., Boehn, S. N., Kaisaki, P. J., Megel, N., Danoy, P., Copley, R. R., Broxholme, J., Witzgall, R., Lathrop, M., Gretz, N., & Gauguier, D. (2005). Missense Mutation in Sterile α Motif of Novel Protein SamCystin is Associated with Polycystic Kidney Disease in (cy/+) Rat. *Journal of the American Society of Nephrology*, *16*(12), 3517–3526. https://doi.org/10.1681/ASN.2005060601

Carbonell, A. U., Cho, C. H., Tindi, J. O., Counts, P. A., Bates, J. C., Erdjument-Bromage, H., Cvejic, S., Iaboni, A., Kvint, I., Rosensaft, J., Banne, E., Anagnostou, E., Neubert, T. A., Scherer, S. W., Molholm, S., & Jordan, B. A. (2019). Haploinsufficiency in the ANKS1B gene encoding AIDA-1 leads to a neurodevelopmental syndrome. *Nature Communications*, *10*(1), 3529. https://doi.org/10.1038/s41467-019-11437-w

Carlin, R. K., Grab, D. J., Cohen, R. S., & Siekevitz, P. (1980). Isolation and characterization of postsynaptic densities from various brain regions: Enrichment of different types of postsynaptic densities. *Journal of Cell Biology*, *86*(3), 831–845. https://doi.org/10.1083/jcb.86.3.831

Chan, C. P., & Rainer, T. H. (2013). Pathophysiological Roles and Clinical Importance of Biomarkers in Acute Coronary Syndrome. In *Advances in Clinical Chemistry* (Vol. 59, pp. 23–63). Elsevier. https://doi.org/10.1016/B978-0-12-405211-6.00002-4

Clifton, N. E., Thomas, K. L., Wilkinson, L. S., Hall, J., & Trent, S. (2020). FMRP and CYFIP1 at the Synapse and Their Role in Psychiatric Vulnerability. *Complex Psychiatry*, *6*(1–2), 5–19. https://doi.org/10.1159/000506858

Cohen, R., Blomberg, F., Berzins, K., & Siekevitz, P. (1977). The structure of postsynaptic densities isolated from dog cerebral cortex: I. overall morphology and protein composition. *Journal of Cell Biology*, *74*(1), 181–203. https://doi.org/10.1083/jcb.74.1.181

Coleman, P. (2003). Synaptic slaughter in Alzheimer's disease. *Neurobiology of Aging*, *24*(8), 1023–1027. https://doi.org/10.1016/j.neurobiolaging.2003.09.001

Collins, M. O., Husi, H., Yu, L., Brandon, J. M., Anderson, C. N. G., Blackstock, W. P., Choudhary, J. S., & Grant, S. G. N. (2006). Molecular characterization and comparison of the components and multiprotein complexes in the postsynaptic proteome. *Journal of Neurochemistry*, *97*, 16–23. https://doi.org/10.1111/j.1471-4159.2005.03507.x

Cooper, M. A., Son, A. I., Komlos, D., Sun, Y., Kleiman, N. J., & Zhou, R. (2008). Loss of ephrin-A5 function disrupts lens fiber cell packing and leads to cataract. *Proceedings of the National Academy of Sciences*, *105*(43), 16620–16625. https://doi.org/10.1073/pnas.0808987105

Cornec-Le Gall, E., Alam, A., & Perrone, R. D. (2019). Autosomal dominant polycystic kidney disease. *The Lancet*, *393*(10174), 919–935. https://doi.org/10.1016/S0140-6736(18)32782-X

Cotman, C. W., Banker, G., Churchill, L., & Taylor, D. (1974). ISOLATION OF POSTSYNAPTIC DENSITIES FROM RAT BRAIN. *Journal of Cell Biology*, *63*(2), 441–455. https://doi.org/10.1083/jcb.63.2.441

Crupi, R., Impellizzeri, D., & Cuzzocrea, S. (2019). Role of Metabotropic Glutamate Receptors in Neurological Disorders. *Frontiers in Molecular Neuroscience*, *12*, 20. https://doi.org/10.3389/fnmol.2019.00020

Davis, G. A., & Bloom, F. E. (1973). Isolation of synaptic junctional complexes from rat brain. *Brain Research*, *62*(1), 135–153. https://doi.org/10.1016/0006-8993(73)90624-0

Davis, J. Q., & Bennett, V. (1990). The anion exchanger and Na+K(+)-ATPase interact with distinct sites on ankyrin in in vitro assays. *The Journal of Biological Chemistry*, *265*(28), 17252–17256.

Diederich, R. J., Matsuno, K., Hing, H., & Artavanis-Tsakonas, S. (1994). Cytosolic interaction between deltex and Notch ankyrin repeats implicates deltex in the Notch signaling pathway. *Development*, *120*(3), 473–481. https://doi.org/10.1242/dev.120.3.473

Dinitto, J., & Lambright, D. (2006). Membrane and juxtamembrane targeting by PH and PTB domains. *Biochimica et Biophysica Acta (BBA) - Molecular and Cell Biology of Lipids*, *1761*(8), 850–867. https://doi.org/10.1016/j.bbalip.2006.04.008

Doolittle, R. (1995). The Multipicity of Domains in Proteins. *Annual Review of Biochemistry*, *64*(1), 287–314.

Dosemeci, A., Tao-Cheng, J.-H., Vinade, L., Winters, C. A., Pozzo-Miller, L., & Reese, T. S. (2001). Glutamate-induced transient modification of the postsynaptic density. *Proceedings of the National Academy of Sciences*, *98*(18), 10428–10432. https://doi.org/10.1073/pnas.181336998

Dosemeci, A., Toy, D., Reese, T. S., & Tao-Cheng, J.-H. (2015). AIDA-1 Moves out of the Postsynaptic Density Core under Excitatory Conditions. *PLOS ONE*, *10*(9), e0137216. https://doi.org/10.1371/journal.pone.0137216

Dosemeci, A., Weinberg, R. J., Reese, T. S., & Tao-Cheng, J.-H. (2016). The Postsynaptic Density: There Is More than Meets the Eye. *Frontiers in Synaptic Neuroscience*, *8*. https://doi.org/10.3389/fnsyn.2016.00023

Dubrow, A., Zuniga, B., Topo, E., & Cho, J.-H. (2022). Suppressing Nonspecific Binding in Biolayer Interferometry Experiments for Weak Ligand–Analyte Interactions. *ACS Omega*, *7*(11), 9206–9211. https://doi.org/10.1021/acsomega.1c05659

Eckel-Passow, J. E., Serie, D. J., Bot, B. M., Joseph, R. W., Cheville, J. C., & Parker, A. S. (2014). ANKS1B is a smoking-related molecular alteration in clear cell renal cell carcinoma. *BMC Urology*, *14*(1), 14. https://doi.org/10.1186/1471-2490-14-14

Enga, R. M., Rice, A. C., Weller, P., Subler, M. A., Lee, D., Hall, C. P., Windle, J. J., Beardsley, P. M., Van Den Oord, E. J., & McClay, J. L. (2017). Initial characterization of behavior and ketamine response in a mouse knockout of the post-synaptic effector gene Anks1b. *Neuroscience Letters*, *641*, 26–32. https://doi.org/10.1016/j.neulet.2017.01.044

Erondu, N., & Kennedy, M. (1985). Regional distribution of type II Ca2+/calmodulin-dependent protein kinase in rat brain. *The Journal of Neuroscience*, *5*(12), 3270–3277. https://doi.org/10.1523/JNEUROSCI.05-12-03270.1985

Fayos, R., Pons, M., & Millet, O. (2005). On the Origin of the Thermostabilization of Proteins Induced by Sodium Phosphate. *Journal of the American Chemical Society*, *127*(27), 9690–9691. https://doi.org/10.1021/ja051352e

Feilen, L. P., Haubrich, K., Strecker, P., Probst, S., Eggert, S., Stier, G., Sinning, I., Konietzko, U., Kins, S., Simon, B., & Wild, K. (2017). Fe65-PTB2 Dimerization Mimics Fe65-APP Interaction. *Frontiers in Molecular Neuroscience*, *10*, 140. https://doi.org/10.3389/fnmol.2017.00140

Feng, W., & Zhang, M. (2009). Organization and dynamics of PDZ-domain-related supramodules in the postsynaptic density. *Nature Reviews Neuroscience*, *10*(2), 87–99. https://doi.org/10.1038/nrn2540

Forrer, P., Binz, H. K., Stumpp, M. T., & Plückthun, A. (2004). Consensus Design of Repeat Proteins. *ChemBioChem*, *5*(2), 183–189. https://doi.org/10.1002/cbic.200300762

Franke, D., & Svergun, D. I. (2009). *DAMMIF* , a program for rapid *ab-initio* shape determination in small-angle scattering. *Journal of Applied Crystallography*, *42*(2), 342–346. https://doi.org/10.1107/S0021889809000338

Gasparini, L., & Dityatev, A. (2008). β-amyloid and glutamate receptors. *Experimental Neurology*, *212*(1), 1–4. https://doi.org/10.1016/j.expneurol.2008.03.005

Gasteiger, E., Hoogland, C., Gattiker, A., Duvaud, S., Wilkins, M. R., Appel, R. D., & Bairoch, A. (2005). Protein Identification and Analysis Tools on the ExPASy Server. In J. M. Walker (Ed.), *The Proteomics Protocols Handbook* (pp. 571–607). Humana Press. https://doi.org/10.1385/1-59259-890-0:571

Ghersi, E., Noviello, C., & D'Adamio, L. (2004). Amyloid-β Protein Precursor (AβPP) Intracellular Domain-associated Protein-1 Proteins Bind to AβPP and Modulate Its Processing in an Isoform-specific Manner. *Journal of Biological Chemistry*, *279*(47), 49105–49112. https://doi.org/10.1074/jbc.M405329200

Ghersi, E., Vito, P., Lopez, P., Abdallah, M., & D'Adamio, L. (2004). The intracellular localization of amyloid β protein precursor (AβPP) intracellular domain associated protein-1 (AIDA-1) is regulated by AβPP and alternative splicing. *Journal of Alzheimer's Disease*, *6*(1), 67–78. https://doi.org/10.3233/JAD-2004-6108

Gill, P., Moghadam, T. T., & Ranjbar, B. (2010). Differential scanning calorimetry techniques: Applications in biology and nanoscience. *Journal of Biomolecular Techniques: JBT*, *21*(4), 167–193.

Glenner, G. G., & Wong, C. W. (1984). Alzheimer's disease: Initial report of the purification and characterization of a novel cerebrovascular amyloid protein. *Biochemical and Biophysical Research Communications*, *120*(3), 885–890. https://doi.org/10.1016/S0006-291X(84)80190-4

Goksoy, E., Ma, Y.-Q., Wang, X., Kong, X., Perera, D., Plow, E. F., & Qin, J. (2008). Structural basis for the autoinhibition of talin in regulating integrin activation. *Molecular Cell*, *31*(1), 124–133. https://doi.org/10.1016/j.molcel.2008.06.011

Gordon, W. R., Arnett, K. L., & Blacklow, S. C. (2008). The molecular logic of Notch signaling—A structural and biochemical perspective. *Journal of Cell Science*, *121*(Pt 19), 3109–3119. https://doi.org/10.1242/jcs.035683

Gorina, S., & Pavletich, N. P. (1996). Structure of the p53 Tumor Suppressor Bound to the Ankyrin and SH3 Domains of 53BP2. *Science*, *274*(5289), 1001–1005. https://doi.org/10.1126/science.274.5289.1001

Graves, B. J., Gillespie, M. E., & Mclntosh, L. P. (1996). DNA binding by the ETS domain. *Nature*, *384*(6607), 322–322. https://doi.org/10.1038/384322a0

Greenfield, N. J. (2006). Using circular dichroism spectra to estimate protein secondary structure. *Nature Protocols*, *1*(6), 2876–2890. https://doi.org/10.1038/nprot.2006.202

Grundke-Iqbal, I., Iqbal, K., Tung, Y. C., Quinlan, M., Wisniewski, H. M., & Binder, L. I. (1986). Abnormal phosphorylation of the microtubule-associated protein tau (tau) in Alzheimer cytoskeletal pathology. *Proceedings of the National Academy of Sciences*, *83*(13), 4913–4917. https://doi.org/10.1073/pnas.83.13.4913

Gu, Z., Liu, W., & Yan, Z. (2009). β-Amyloid Impairs AMPA Receptor Trafficking and Function by Reducing Ca2+/Calmodulin-dependent Protein Kinase II Synaptic Distribution. *Journal of Biological Chemistry*, *284*(16), 10639–10649. https://doi.org/10.1074/jbc.M806508200

Guo, M., Jan, L. Y., & Jan, Y. N. (1996). Control of Daughter Cell Fates during Asymmetric Division: Interaction of Numb and Notch. *Neuron*, *17*(1), 27–41. https://doi.org/10.1016/S0896-6273(00)80278-0

Hajszan, T., MacLusky, N. J., & Leranth, C. (2005). Short-term treatment with the antidepressant fluoxetine triggers pyramidal dendritic spine synapse formation in rat hippocampus. *European Journal of Neuroscience*, *21*(5), 1299–1303. https://doi.org/10.1111/j.1460-9568.2005.03968.x

Herberich, S. E., Klose, R., Moll, I., Yang, W.-J., Wüstehube-Lausch, J., & Fischer, A. (2015). ANKS1B Interacts with the Cerebral Cavernous Malformation Protein-1 and Controls Endothelial Permeability but Not Sprouting Angiogenesis. *PLOS ONE*, *10*(12), e0145304. https://doi.org/10.1371/journal.pone.0145304

Hering, H., & Sheng, M. (2001). Dentritic spines: Structure, dynamics and regulation. *Nature Reviews Neuroscience*, *2*(12), 880–888. https://doi.org/10.1038/35104061

Hervé, D., & Chabriat, H. (2010). CADASIL. *Journal of Geriatric Psychiatry and Neurology*, *23*(4), 269–276. https://doi.org/10.1177/0891988710383570

Hopkins, J. B., Gillilan, R. E., & Skou, S. (2017). *BioXTAS RAW*: Improvements to a free open-source program for small-angle X-ray scattering data reduction and analysis. *Journal of Applied Crystallography*, *50*(5), 1545–1553. https://doi.org/10.1107/S1600576717011438

Husi, H. (2004). NMDA Receptors, Neural Pathways, and Protein Interaction Databases. In *International Review of Neurobiology* (Vol. 61, pp. 49–77). Elsevier. https://doi.org/10.1016/S0074-7742(04)61003-8

Islam, M. M., Kobayashi, K., Kidokoro, S., & Kuroda, Y. (2019). Hydrophobic surface residues can stabilize a protein through improved water–protein interactions. *The FEBS Journal*, *286*(20), 4122–4134. https://doi.org/10.1111/febs.14941

Jacob, A. L., Jordan, B. A., & Weinberg, R. J. (2010). Organization of amyloid-β protein precursor intracellular domain-associated protein-1 in the rat brain. *The Journal of Comparative Neurology*, *518*(16), 3221–3236. https://doi.org/10.1002/cne.22394

Jacobs, M. D., & Harrison, S. C. (1998). Structure of an IκBα/NF-κB Complex. *Cell*, *95*(6), 749–758. https://doi.org/10.1016/S0092-8674(00)81698-0

Janzen, V., Forkert, R., Fleming, H. E., Saito, Y., Waring, M. T., Dombkowski, D. M., Cheng, T., DePinho, R. A., Sharpless, N. E., & Scadden, D. T. (2006). Stem-cell ageing modified by the cyclin-dependent kinase inhibitor p16INK4a. *Nature*, *443*(7110), 421–426. https://doi.org/10.1038/nature05159

Jordan, B. A., Fernholz, B. D., Khatri, L., & Ziff, E. B. (2007). Activity-dependent AIDA-1 nuclear signaling regulates nucleolar numbers and protein synthesis in neurons. *Nature Neuroscience*, *10*(4), 427–435. https://doi.org/10.1038/nn1867

Joutel, A., Corpechot, C., Ducros, A., Vahedi, K., Chabriat, H., Mouton, P., Alamowitch, S., Domenga, V., Cécillion, M., Maréchal, E., Maciazek, J., Vayssière, C., Cruaud, C., Cabanis, E.-A., Ruchoux, M. M., Weissenbach, J., Bach, J. F., Bousser, M. G., & Tournier-Lasserve, E. (1996). Notch3 mutations in CADASIL, a hereditary adult-onset condition causing stroke and dementia. *Nature*, *383*(6602), 707–710. https://doi.org/10.1038/383707a0

Jumper, J., Evans, R., Pritzel, A., Green, T., Figurnov, M., Ronneberger, O., Tunyasuvunakool, K., Bates, R., Žídek, A., Potapenko, A., Bridgland, A., Meyer, C., Kohl, S. A. A., Ballard, A. J., Cowie, A., Romera-Paredes, B., Nikolov, S., Jain, R., Adler, J., … Hassabis, D. (2021). Highly accurate protein structure prediction with AlphaFold. *Nature*, *596*(7873), 583–589. https://doi.org/10.1038/s41586-021-03819-2

Kaizuka, T., & Takumi, T. (2018). Postsynaptic density proteins and their involvement in neurodevelopmental disorders. *The Journal of Biochemistry*, *163*(6), 447–455. https://doi.org/10.1093/jb/mvy022

Kaneko, T., Joshi, R., Feller, S. M., & Li, S. S. (2012). Phosphotyrosine recognition domains: The typical, the atypical and the versatile. *Cell Communication and Signaling: CCS*, *10*(1), 32. https://doi.org/10.1186/1478-811X-10-32

Kasai, H., Matsuzaki, M., Noguchi, J., Yasumatsu, N., & Nakahara, H. (2003). Structure–stability–function relationships of dendritic spines. *Trends in Neurosciences*, *26*(7), 360–368. https://doi.org/10.1016/S0166-2236(03)00162-0

Keith, D. (2008). Excitation control: Balancing PSD-95 function at the synapse. *Frontiers in Molecular Neuroscience*, *1*. https://doi.org/10.3389/neuro.02.004.2008

Kennedy, M. B. (1997). The postsynaptic density at glutamatergic synapses. *Trends in Neurosciences*, *20*(6), 264–268. https://doi.org/10.1016/S0166-2236(96)01033-8

Kennedy, M. B. (2000). Signal-Processing Machines at the Postsynaptic Density. *Science*, *290*(5492), 750–754. https://doi.org/10.1126/science.290.5492.750

Kennedy, M. J., Davison, I. G., Robinson, C. G., & Ehlers, M. D. (2010). Syntaxin-4 Defines a Domain for Activity-Dependent Exocytosis in Dendritic Spines. *Cell*, *141*(3), 524–535. https://doi.org/10.1016/j.cell.2010.02.042

Kim, C. (2003). SAM domains: Uniform structure, diversity of function. *Trends in Biochemical Sciences*, *28*(12), 625–628. https://doi.org/10.1016/j.tibs.2003.11.001

Klauck, T. M., & Scott, J. D. (1995). The postsynaptic density: A subcellular anchor for signal transduction enzymes. *Cellular Signalling*, *7*(8), 747–757. https://doi.org/10.1016/0898-6568(95)02003-9

Knight, M. J., Leettola, C., Gingery, M., Li, H., & Bowie, J. U. (2011). A human sterile alpha motif domain polymerizome. *Protein Science: A Publication of the Protein Society*, *20*(10), 1697–1706. https://doi.org/10.1002/pro.703

Kobe, B., & Kajava, A. V. (2000). When protein folding is simplified to protein coiling: The continuum of solenoid protein structures. *Trends in Biochemical Sciences*, *25*(10), 509–515. https://doi.org/10.1016/S0968-0004(00)01667-4

Kohl, A., Binz, H. K., Forrer, P., Stumpp, M. T., Plückthun, A., & Grütter, M. G. (2003). Designed to be stable: Crystal structure of a consensus ankyrin repeat protein. *Proceedings of the National Academy of Sciences*, *100*(4), 1700–1705. https://doi.org/10.1073/pnas.0337680100

Kruse, A., & Dinjus, E. (2007). Hot compressed water as reaction medium and reactant. *The Journal of Supercritical Fluids*, *39*(3), 362–380. https://doi.org/10.1016/j.supflu.2006.03.016

Kukuk, L., Dingley, A. J., Granzin, J., Nagel-Steger, L., Thiagarajan-Rosenkranz, P., Ciupka, D., Hänel, K., Batra-Safferling, R., Pacheco, V., Stoldt, M., Pfeffer, K., Beer-Hammer, S., Willbold, D., & Koenig, B. W. (2019). Structure of the SLy1 SAM homodimer reveals a new interface for SAM domain self-association. *Scientific Reports*, *9*(1), 54. https://doi.org/10.1038/s41598-018-37185-3

Kurabi, A., Brener, S., Mobli, M., Kwan, J. J., & Donaldson, L. W. (2009). A Nuclear Localization Signal at the SAM–SAM Domain Interface of AIDA-1 Suggests a Requirement for Domain Uncoupling Prior to Nuclear Import. *Journal of Molecular Biology*, *392*(5), 1168–1177. https://doi.org/10.1016/j.jmb.2009.08.004

Kurochkina, N., & Guha, U. (2013). SH3 domains: Modules of protein–protein interactions. *Biophysical Reviews*, *5*(1), 29–39. https://doi.org/10.1007/s12551-012-0081-z

Kwan, T. O. C., Kolek, S. A., Danson, A. E., Reis, R. I., Camacho, I. S., Shaw Stewart, P. D., & Moraes, I. (2022). Measuring Protein Aggregation and Stability Using High-Throughput Biophysical Approaches. *Frontiers in Molecular Biosciences*, *9*, 890862. https://doi.org/10.3389/fmolb.2022.890862

Leettola, C. N., Knight, M. J., Cascio, D., Hoffman, S., & Bowie, J. U. (2014). Characterization of the SAM domain of the PKD-related protein ANKS6 and its interaction with ANKS3. *BMC Structural Biology*, *14*(1), 17. https://doi.org/10.1186/1472-6807-14-17

Lesné, S., Ali, C., Gabriel, C., Croci, N., MacKenzie, E. T., Glabe, C. G., Plotkine, M., Marchand-Verrecchia, C., Vivien, D., & Buisson, A. (2005). NMDA Receptor Activation Inhibits α-Secretase and Promotes Neuronal Amyloid-β Production. *The Journal of Neuroscience*, *25*(41), 9367–9377. https://doi.org/10.1523/JNEUROSCI.0849-05.2005

Letunic, I. (2002). Recent improvements to the SMART domain-based sequence annotation resource. *Nucleic Acids Research*, *30*(1), 242–244. https://doi.org/10.1093/nar/30.1.242

Leysen, J. (2004). 5-HT2 Receptors. *Current Drug Target -CNS & Neurological Disorders*, *3*(1), 11–26. https://doi.org/10.2174/1568007043482598

Li, J., Mahajan, A., & Tsai, M.-D. (2006). Ankyrin Repeat: A Unique Motif Mediating Protein−Protein Interactions. *Biochemistry*, *45*(51), 15168–15178. https://doi.org/10.1021/bi062188q

Li, J., Poi, M. J., Qin, D., Selby, T. L., Byeon, I.-J., & Tsai, M.-D. (2000). Tumor Suppressor INK4: Quantitative Structure−Function Analyses of p18 ^{INK4C} as an Inhibitor of Cyclin-Dependent Kinase 4. *Biochemistry*, *39*(4), 649–657. https://doi.org/10.1021/bi991281u

Li, J., & Tsai, M.-D. (2002). Novel Insights into the INK4-CDK4/6-Rb Pathway: Counter Action of Gankyrin against INK4 Proteins Regulates the CDK4-Mediated Phosphorylation of Rb. *Biochemistry*, *41*(12), 3977–3983. https://doi.org/10.1021/bi011550s

Li, S.-C., Zwahlen, C., Vincent, S. J. F., McGlade, C. J., Kay, L. E., Pawson, T., & Forman-Kay, J. D. (1998). Structure of a Numb PTB domain–peptide complex suggests a basis for diverse binding specificity. *Nature Structural Biology*, *5*(12), 1075–1083. https://doi.org/10.1038/4185

Lim, S., Sala, C., Yoon, J., Park, S., Kuroda, S., Sheng, M., & Kim, E. (2001). Sharpin, a Novel Postsynaptic Density Protein That Directly Interacts with the Shank Family of Proteins. *Molecular and Cellular Neuroscience*, *17*(2), 385–397. https://doi.org/10.1006/mcne.2000.0940

Liu, P.-P., Xie, Y., Meng, X.-Y., & Kang, J.-S. (2019). History and progress of hypotheses and clinical trials for Alzheimer's disease. *Signal Transduction and Targeted Therapy*, *4*(1), 29. https://doi.org/10.1038/s41392-019-0063-8

Liu, W., Yu, C., Li, J., & Fang, J. (2022). The Roles of EphB2 in Cancer. *Frontiers in Cell and Developmental Biology*, *10*, 788587. https://doi.org/10.3389/fcell.2022.788587

Lu, J., Wu, T., Zhang, B., Liu, S., Song, W., Qiao, J., & Ruan, H. (2021). Types of nuclear localization signals and mechanisms of protein import into the nucleus. *Cell Communication and Signaling*, *19*(1), 60. https://doi.org/10.1186/s12964-021-00741-y

Lupberger, J., Zeisel, M. B., Xiao, F., Thumann, C., Fofana, I., Zona, L., Davis, C., Mee, C. J., Turek, M., Gorke, S., Royer, C., Fischer, B., Zahid, M. N., Lavillette, D., Fresquet, J., Cosset, F.-L., Rothenberg, S. M., Pietschmann, T., Patel, A. H., … Baumert, T. F. (2011). EGFR and EphA2 are host factors for hepatitis C virus entry and possible targets for antiviral therapy. *Nature Medicine*, *17*(5), 589–595. https://doi.org/10.1038/nm.2341

Lux, S. E., John, K. M., & Bennett, V. (1990). Analysis of cDNA for human erythrocyte ankyrin indicates a repeated structure with homology to tissue-differentiation and cell-cycle control proteins. *Nature*, *344*(6261), 36–42. https://doi.org/10.1038/344036a0

Matos, M. F., Xu, Y., Dulubova, I., Otwinowski, Z., Richardson, J. M., Tomchick, D. R., Rizo, J., & Ho, A. (2012). Autoinhibition of Mint1 adaptor protein regulates amyloid precursor protein binding and processing. *Proceedings of the National Academy of Sciences of the United States of America*, *109*(10), 3802–3807. https://doi.org/10.1073/pnas.1119075109

Mayer, B. J. (2001). SH3 domains: Complexity in moderation. *Journal of Cell Science*, *114*(7), 1253–1263. https://doi.org/10.1242/jcs.114.7.1253

McGirr, S., Venegas, C., & Swaminathan, A. (2020). Alzheimers Disease: A Brief Review. *Journal of Experimental Neurology*, *1*(3). https://doi.org/10.33696/Neurol.1.015

McGrath, J. A. (2001). Hay-Wells syndrome is caused by heterozygous missense mutations in the SAM domain of p63. *Human Molecular Genetics*, *10*(3), 221–229. https://doi.org/10.1093/hmg/10.3.221

Mercurio, F. A., Marasco, D., Pirone, L., Pedone, E. M., Pellecchia, M., & Leone, M. (2012). Solution Structure of the First Sam Domain of Odin and Binding Studies with the EphA2 Receptor. *Biochemistry*, *51*(10), 2136–2145. https://doi.org/10.1021/bi300141h

Mercurio, F., & Leone, M. (2016). The Sam Domain of EphA2 Receptor and its Relevance to Cancer: A Novel Challenge for Drug Discovery? *Current Medicinal Chemistry*, *23*(42), 4718–4734. https://doi.org/10.2174/0929867323666161101100722

Meruelo, A. D., & Bowie, J. U. (2009). Identifying polymer-forming SAM domains. *Proteins: Structure, Function, and Bioinformatics*, *74*(1), 1–5. https://doi.org/10.1002/prot.22232

Michaely, P. (2002). Crystal structure of a 12 ANK repeat stack from human ankyrinR. *The EMBO Journal*, *21*(23), 6387–6396. https://doi.org/10.1093/emboj/cdf651

Micsonai, A., Wien, F., Bulyáki, É., Kun, J., Moussong, É., Lee, Y.-H., Goto, Y., Réfrégiers, M., & Kardos, J. (2018). BeStSel: A web server for accurate protein secondary structure prediction and fold recognition from the circular dichroism spectra. *Nucleic Acids Research*, *46*(W1), W315–W322. https://doi.org/10.1093/nar/gky497

Miura, K. (2018). An Overview of Current Methods to Confirm Protein-Protein Interactions. *Protein and Peptide Letters*, *25*(8), 728–733. https://doi.org/10.2174/0929866525666180821122240

Mosavi, L. K., Cammett, T. J., Desrosiers, D. C., & Peng, Z. (2004). The ankyrin repeat as molecular architecture for protein recognition. *Protein Science*, *13*(6), 1435–1448. https://doi.org/10.1110/ps.03554604

Musacchio, A., Wilmanns, M., & Saraster, M. (1994). Structure and function of the SH3 domain. *Progress in Biophysics and Molecular Biology*, *61*(3), 283–297. https://doi.org/10.1016/0079-6107(94)90003-5

Newcomer, J. W., Farber, N. B., & Olney, J. W. (2000). NMDA receptor function, memory, and brain aging. *Dialogues in Clinical Neuroscience*, *2*(3), 219–232. https://doi.org/10.31887/DCNS.2000.2.3/jnewcomer

Niesen, F. H., Berglund, H., & Vedadi, M. (2007). The use of differential scanning fluorimetry to detect ligand interactions that promote protein stability. *Nature Protocols*, *2*(9), 2212–2221. https://doi.org/10.1038/nprot.2007.321

Ntelios, D., Berninger, B., & Tzimagiorgis, G. (2012). Numb and Alzheimer's disease: The current picture. *Frontiers in Neuroscience*, *6*, 145. https://doi.org/10.3389/fnins.2012.00145

Nurk, S., Koren, S., Rhie, A., Rautiainen, M., Bzikadze, A. V., Mikheenko, A., Vollger, M. R., Altemose, N., Uralsky, L., Gershman, A., Aganezov, S., Hoyt, S. J., Diekhans, M., Logsdon, G. A., Alonge, M., Antonarakis, S. E., Borchers, M., Bouffard, G. G., Brooks, S. Y., … Phillippy, A. M. (2022). The complete sequence of a human genome. *Science*, *376*(6588), 44–53. https://doi.org/10.1126/science.abj6987

Oberstrass, F. C., Lee, A., Stefl, R., Janis, M., Chanfreau, G., & Allain, F. H.-T. (2006). Shape-specific recognition in the structure of the Vts1p SAM domain with RNA. *Nature Structural & Molecular Biology*, *13*(2), 160–167. https://doi.org/10.1038/nsmb1038

Ogawa, T., & Hirokawa, N. (2018). Multiple analyses of protein dynamics in solution. *Biophysical Reviews*, *10*(2), 299–306. https://doi.org/10.1007/s12551-017-0354-7

Omkumar, R. V., Kiely, M. J., Rosenstein, A. J., Min, K.-T., & Kennedy, M. B. (1996). Identification of a Phosphorylation Site for Calcium/Calmodulindependent Protein Kinase II in the NR2B Subunit of the N-Methyl-D-aspartate Receptor. *Journal of Biological Chemistry*, *271*(49), 31670–31678. https://doi.org/10.1074/jbc.271.49.31670

Orengo, C. A., & Thornton, J. M. (2005). PROTEIN FAMILIES AND THEIR EVOLUTION—A STRUCTURAL PERSPECTIVE. *Annual Review of Biochemistry*, *74*(1), 867–900. https://doi.org/10.1146/annurev.biochem.74.082803.133029

P. Bagowski, C., Bruins, W., & J.W. Te Velthuis, A. (2010). The Nature of Protein Domain Evolution: Shaping the Interaction Network. *Current Genomics*, *11*(5), 368–376. https://doi.org/10.2174/138920210791616725

Padarti, A., Abou-Fadel, J., & Zhang, J. (2021). Resurgence of phosphotyrosine binding domains: Structural and functional properties essential for understanding disease pathogenesis. *Biochimica et Biophysica Acta (BBA) - General Subjects*, *1865*(11), 129977. https://doi.org/10.1016/j.bbagen.2021.129977

Palay, S. L. (1956). SYNAPSES IN THE CENTRAL NERVOUS SYSTEM. *The Journal of Biophysical and Biochemical Cytology*, *2*(4), 193–202. https://doi.org/10.1083/jcb.2.4.193

Park, J. E., Son, A. I., Hua, R., Wang, L., Zhang, X., & Zhou, R. (2012). Human Cataract Mutations in EPHA2 SAM Domain Alter Receptor Stability and Function. *PLoS ONE*, *7*(5), e36564. https://doi.org/10.1371/journal.pone.0036564

Peng, J., Kim, M. J., Cheng, D., Duong, D. M., Gygi, S. P., & Sheng, M. (2004). Semiquantitative Proteomic Analysis of Rat Forebrain Postsynaptic Density Fractions by Mass Spectrometry. *Journal of Biological Chemistry*, *279*(20), 21003–21011. https://doi.org/10.1074/jbc.M400103200

Petersen, J. D., Chen, X., Vinade, L., Dosemeci, A., Lisman, J. E., & Reese, T. S. (2003). Distribution of Postsynaptic Density (PSD)-95 and Ca^{2+} / Calmodulin-Dependent Protein Kinase II at the PSD. *The Journal of Neuroscience*, *23*(35), 11270–11278. https://doi.org/10.1523/JNEUROSCI.23-35-11270.2003

Petoukhov, M. V., & Svergun, D. I. (2015). Ambiguity assessment of small-angle scattering curves from monodisperse systems. *Acta Crystallographica Section D Biological Crystallography*, *71*(5), 1051–1058. https://doi.org/10.1107/S1399004715002576

Ponomarenko, E. A., Poverennaya, E. V., Ilgisonis, E. V., Pyatnitskiy, M. A., Kopylov, A. T., Zgoda, V. G., Lisitsa, A. V., & Archakov, A. I. (2016). The Size of the Human Proteome: The Width and Depth. *International Journal of Analytical Chemistry*, *2016*, 1–6. https://doi.org/10.1155/2016/7436849

Ponting, C. P. (1995). SAM: A novel motif in yeast sterile and *drosophila* polyhomeotic proteins. *Protein Science*, *4*(9), 1928–1930. https://doi.org/10.1002/pro.5560040927

Qiao, F., & Bowie, J. U. (2005). The Many Faces of SAM. *Science's STKE*, *2005*(286). https://doi.org/10.1126/stke.2862005re7

Rader, K., Orlando, R. A., Lou, X., & Farquhar, M. G. (2000). Characterization of ANKRA, a novel ankyrin repeat protein that interacts with the cytoplasmic domain of megalin. *Journal of the*

American Society of Nephrology: JASN, *11*(12), 2167–2178. https://doi.org/10.1681/ASN.V11122167

Rambo, R. P., & Tainer, J. A. (2013). Accurate assessment of mass, models and resolution by small-angle scattering. *Nature*, *496*(7446), 477–481. https://doi.org/10.1038/nature12070

Rogelj, B., Mitchell, J. C., Miller, C. C. J., & McLoughlin, D. M. (2006). The X11/Mint family of adaptor proteins. *Brain Research Reviews*, *52*(2), 305–315. https://doi.org/10.1016/j.brainresrev.2006.04.005

Roncarati, R., Šestan, N., Scheinfeld, M. H., Berechid, B. E., Lopez, P. A., Meucci, O., McGlade, J. C., Rakic, P., & D'Adamio, L. (2002). The γ-secretase-generated intracellular domain of β-amyloid precursor protein binds Numb and inhibits Notch signaling. *Proceedings of the National Academy of Sciences*, *99*(10), 7102–7107. https://doi.org/10.1073/pnas.102192599

Ruas, M., & Peters, G. (1998). The p16INK4a/CDKN2A tumor suppressor and its relatives. *Biochimica et Biophysica Acta (BBA) - Reviews on Cancer*, *1378*(2), F115–F177. https://doi.org/10.1016/S0304-419X(98)00017-1

Russell, S. T., & Warshel, A. (1985). Calculations of electrostatic energies in proteins. *Journal of Molecular Biology*, *185*(2), 389–404. https://doi.org/10.1016/0022-2836(85)90411-5

Russo, A. A., Tong, L., Lee, J.-O., Jeffrey, P. D., & Pavletich, N. P. (1998). Structural basis for inhibition of the cyclin-dependent kinase Cdk6 by the tumour suppressor p16INK4a. *Nature*, *395*(6699), 237–243. https://doi.org/10.1038/26155

Russo, T., Faraonio, R., Minopoli, G., De Candia, P., De Renzis, S., & Zambrano, N. (1998). Fe65 and the protein network centered around the cytosolic domain of the Alzheimer's β-amyloid precursor protein. *FEBS Letters*, *434*(1–2), 1–7. https://doi.org/10.1016/S0014-5793(98)00941-7

Sabo, S. L., Lanier, L. M., Ikin, A. F., Khorkova, O., Sahasrabudhe, S., Greengard, P., & Buxbaum, J. D. (1999). Regulation of β-Amyloid Secretion by FE65, an Amyloid Protein Precursor-binding Protein. *Journal of Biological Chemistry*, *274*(12), 7952–7957. https://doi.org/10.1074/jbc.274.12.7952

Sayers, E. W., Bolton, E. E., Brister, J. R., Canese, K., Chan, J., Comeau, D. C., Connor, R., Funk, K., Kelly, C., Kim, S., Madej, T., Marchler-Bauer, A., Lanczycki, C., Lathrop, S., Lu, Z., Thibaud-Nissen, F., Murphy, T., Phan, L., Skripchenko, Y., … Sherry, S. T. (2022). Database resources of the national center for biotechnology information. *Nucleic Acids Research*, *50*(D1), D20–D26. https://doi.org/10.1093/nar/gkab1112

Schrodinger, L. L. C. (2015). *The PyMOL molecular graphics system* (1.8).

Sedgwick, S. G., & Smerdon, S. J. (1999). The ankyrin repeat: A diversity of interactions on a common structural framework. *Trends in Biochemical Sciences*, *24*(8), 311–316. https://doi.org/10.1016/S0968-0004(99)01426-7

Seidel, J. J., & Graves, B. J. (2002). An ERK2 docking site in the Pointed domain distinguishes a subset of ETS transcription factors. *Genes & Development*, *16*(1), 127–137. https://doi.org/10.1101/gad.950902

Serrano, M., Hannon, G. J., & Beach, D. (1993). A new regulatory motif in cell-cycle control causing specific inhibition of cyclin D/CDK4. *Nature*, *366*(6456), 704–707. https://doi.org/10.1038/366704a0

Shankar, G. M., Bloodgood, B. L., Townsend, M., Walsh, D. M., Selkoe, D. J., & Sabatini, B. L. (2007). Natural Oligomers of the Alzheimer Amyloid-β Protein Induce Reversible Synapse Loss by Modulating an NMDA-Type Glutamate Receptor-Dependent Signaling Pathway. *The Journal of Neuroscience*, *27*(11), 2866–2875. https://doi.org/10.1523/JNEUROSCI.4970-06.2007

Sharrocks, A. D. (2001). The ETS-domain transcription factor family. *Nature Reviews Molecular Cell Biology*, *2*(11), 827–837. https://doi.org/10.1038/35099076
Sheng, M. (2001). Molecular organization of the postsynaptic specialization. *Proceedings of the National Academy of Sciences*, *98*(13), 7058–7061. https://doi.org/10.1073/pnas.111146298
Sheng, M., & Kim, E. (2000). The Shank family of scaffold proteins. *Journal of Cell Science*, *113*(11), 1851–1856. https://doi.org/10.1242/jcs.113.11.1851
Sheng, M., & Kim, E. (2011). The Postsynaptic Organization of Synapses. *Cold Spring Harbor Perspectives in Biology*, *3*(12), a005678–a005678. https://doi.org/10.1101/cshperspect.a005678
Siegmund, R. F., & Nasmyth, K. A. (1996). The Saccharomyces cerevisiae Start-specific transcription factor Swi4 interacts through the ankyrin repeats with the mitotic Clb2/Cdc28 kinase and through its conserved carboxy terminus with Swi6. *Molecular and Cellular Biology*, *16*(6), 2647–2655. https://doi.org/10.1128/MCB.16.6.2647
Siekevitz, P. (1985). The postsynaptic density: A possible role in long-lasting effects in the central nervous system. *Proceedings of the National Academy of Sciences*, *82*(10), 3494–3498. https://doi.org/10.1073/pnas.82.10.3494
Smirnova, E. (2017). *Structure-Function Studies of Scaffolding Proteins Involved in the Formation of Neuronal Connections: AIDA1 and CASKIN2*. York University.
Smirnova, E., Shanbhag, R., Kurabi, A., Mobli, M., Kwan, J. J., & Donaldson, L. W. (2013). Solution Structure and Peptide Binding of the PTB Domain from the AIDA1 Postsynaptic Signaling Scaffolding Protein. *PLoS ONE*, *8*(6), e65605. https://doi.org/10.1371/journal.pone.0065605
Smith, M. J., Hardy, W. R., Murphy, J. M., Jones, N., & Pawson, T. (2006). Screening for PTB domain binding partners and ligand specificity using proteome-derived NPXY peptide arrays. *Molecular and Cellular Biology*, *26*(22), 8461–8474. https://doi.org/10.1128/MCB.01491-06
Song, X., Yang, J., Hirbawi, J., Ye, S., Perera, H. D., Goksoy, E., Dwivedi, P., Plow, E. F., Zhang, R., & Qin, J. (2012). A novel membrane-dependent on/off switch mechanism of talin FERM domain at sites of cell adhesion. *Cell Research*, *22*(11), 1533–1545. https://doi.org/10.1038/cr.2012.97
Srinivasan, M., Edman, C. F., & Schulman, H. (1994). Alternative splicing introduces a nuclear localization signal that targets multifunctional CaM kinase to the nucleus. *Journal of Cell Biology*, *126*(4), 839–852. https://doi.org/10.1083/jcb.126.4.839
Stagner, E. E., Bouvrette, D. J., Cheng, J., & Bryda, E. C. (2009). The polycystic kidney disease-related proteins Bicc1 and SamCystin interact. *Biochemical and Biophysical Research Communications*, *383*(1), 16–21. https://doi.org/10.1016/j.bbrc.2009.03.113
Stelzer, G., Rosen, N., Plaschkes, I., Zimmerman, S., Twik, M., Fishilevich, S., Stein, T. I., Nudel, R., Lieder, I., Mazor, Y., Kaplan, S., Dahary, D., Warshawsky, D., Guan-Golan, Y., Kohn, A., Rappaport, N., Safran, M., & Lancet, D. (2016). The GeneCards Suite: From Gene Data Mining to Disease Genome Sequence Analyses. *Current Protocols in Bioinformatics*, *54*(1). https://doi.org/10.1002/cpbi.5
Stevens, S. R., & Rasband, M. N. (2021). Ankyrins and neurological disease. *Current Opinion in Neurobiology*, *69*, 51–57. https://doi.org/10.1016/j.conb.2021.01.002
Stolt, P. C., Jeon, H., Song, H. K., Herz, J., Eck, M. J., & Blacklow, S. C. (2003). Origins of Peptide Selectivity and Phosphoinositide Binding Revealed by Structures of Disabled-1 PTB Domain Complexes. *Structure*, *11*(5), 569–579. https://doi.org/10.1016/S0969-2126(03)00068-6
Sturgill, J. F., Steiner, P., Czervionke, B. L., & Sabatini, B. L. (2009). Distinct Domains within PSD-95 Mediate Synaptic Incorporation, Stabilization, and Activity-Dependent Trafficking. *The Journal of Neuroscience*, *29*(41), 12845–12854. https://doi.org/10.1523/JNEUROSCI.1841-09.2009

Thanos, C. D., Goodwill, K. E., & Bowie, J. U. (1999). Oligomeric Structure of the Human EphB2 Receptor SAM Domain. *Science*, *283*(5403), 833–836. https://doi.org/10.1126/science.283.5403.833

Tindi, J. O., Chavez, A. E., Cvejic, S., Calvo-Ochoa, E., Castillo, P. E., & Jordan, B. A. (2015). ANKS1B Gene Product AIDA-1 Controls Hippocampal Synaptic Transmission by Regulating GluN2B Subunit Localization. *Journal of Neuroscience*, *35*(24), 8986–8996. https://doi.org/10.1523/JNEUROSCI.4029-14.2015

Tran, H. H., Kim, C. A., Faham, S., Siddall, M.-C., & Bowie, J. U. (2002). Native interface of the SAM domain polymer of TEL. *BMC Structural Biology*, *2*(1), 5. https://doi.org/10.1186/1472-6807-2-5

Uhlik, M. T., Temple, B., Bencharit, S., Kimple, A. J., Siderovski, D. P., & Johnson, G. L. (2005). Structural and Evolutionary Division of Phosphotyrosine Binding (PTB) Domains. *Journal of Molecular Biology*, *345*(1), 1–20. https://doi.org/10.1016/j.jmb.2004.10.038

Valtschanoff, J. G., & Weinberg, R. J. (2001). Laminar Organization of the NMDA Receptor Complex within the Postsynaptic Density. *The Journal of Neuroscience*, *21*(4), 1211–1217. https://doi.org/10.1523/JNEUROSCI.21-04-01211.2001

Vanek, T., & Kohli, A. (2023). Biochemistry, Myoglobin. In *StatPearls*. StatPearls Publishing. http://www.ncbi.nlm.nih.gov/books/NBK544256/

Varadi, M., Anyango, S., Deshpande, M., Nair, S., Natassia, C., Yordanova, G., Yuan, D., Stroe, O., Wood, G., Laydon, A., Žídek, A., Green, T., Tunyasuvunakool, K., Petersen, S., Jumper, J., Clancy, E., Green, R., Vora, A., Lutfi, M., … Velankar, S. (2022). AlphaFold Protein Structure Database: Massively expanding the structural coverage of protein-sequence space with high-accuracy models. *Nucleic Acids Research*, *50*(D1), D439–D444. https://doi.org/10.1093/nar/gkab1061

Wagner, M. J., Stacey, M. M., Liu, B. A., & Pawson, T. (2013). Molecular Mechanisms of SH2- and PTB-Domain-Containing Proteins in Receptor Tyrosine Kinase Signaling. *Cold Spring Harbor Perspectives in Biology*, *5*(12), a008987–a008987. https://doi.org/10.1101/cshperspect.a008987

Walikonis, R. S., Jensen, O. N., Mann, M., Provance, D. W., Mercer, J. A., & Kennedy, M. B. (2000). Identification of Proteins in the Postsynaptic Density Fraction by Mass Spectrometry. *The Journal of Neuroscience*, *20*(11), 4069–4080. https://doi.org/10.1523/JNEUROSCI.20-11-04069.2000

Wang, Y., Shang, Y., Li, J., Chen, W., Li, G., Wan, J., Liu, W., & Zhang, M. (2018). Specific Eph receptor-cytoplasmic effector signaling mediated by SAM–SAM domain interactions. *ELife*, *7*, e35677. https://doi.org/10.7554/eLife.35677

Wegener, K. L., Partridge, A. W., Han, J., Pickford, A. R., Liddington, R. C., Ginsberg, M. H., & Campbell, I. D. (2007). Structural Basis of Integrin Activation by Talin. *Cell*, *128*(1), 171–182. https://doi.org/10.1016/j.cell.2006.10.048

Wilhelm, M., Schlegl, J., Hahne, H., Gholami, A. M., Lieberenz, M., Savitski, M. M., Ziegler, E., Butzmann, L., Gessulat, S., Marx, H., Mathieson, T., Lemeer, S., Schnatbaum, K., Reimer, U., Wenschuh, H., Mollenhauer, M., Slotta-Huspenina, J., Boese, J.-H., Bantscheff, M., … Kuster, B. (2014). Mass-spectrometry-based draft of the human proteome. *Nature*, *509*(7502), 582–587. https://doi.org/10.1038/nature13319

Wulczyn, F. G., Naumann, M., & Scheidereit, C. (1992). Candidate proto-oncogene bcl-3 encodes a subunit-specific inhibitor of transcription factor NF-kappa B. *Nature*, *358*(6387), 597–599. https://doi.org/10.1038/358597a0

Yan, K. S., Kuti, M., & Zhou, M.-M. (2002). PTB or not PTB - that is the question. *FEBS Letters*, *513*(1), 67–70. https://doi.org/10.1016/S0014-5793(01)03305-1

Yuan, C., Li, J., Mahajan, A., Poi, M. J., Byeon, I.-J. L., & Tsai, M.-D. (2004). Solution Structure of the Human Oncogenic Protein Gankyrin Containing Seven Ankyrin Repeats and Analysis of Its Structure−Function Relationship †. *Biochemistry*, *43*(38), 12152–12161. https://doi.org/10.1021/bi049116o

Yuesong Gong, & Lippa, C. F. (2010). Review: Disruption of the Postsynaptic Density in Alzheimer's Disease and Other Neurodegenerative Dementias. *American Journal of Alzheimer's Disease & Other Dementiasr*, *25*(7), 547–555. https://doi.org/10.1177/1533317510382893

Yun, M., Keshvara, L., Park, C.-G., Zhang, Y.-M., Dickerson, J. B., Zheng, J., Rock, C. O., Curran, T., & Park, H.-W. (2003). Crystal Structures of the Dab Homology Domains of Mouse Disabled 1 and 2. *Journal of Biological Chemistry*, *278*(38), 36572–36581. https://doi.org/10.1074/jbc.M304384200

Zeeb, M., Rösner, H., Zeslawski, W., Canet, D., Holak, T. A., & Balbach, J. (2002). Protein folding and stability of human CDK inhibitor p19INK4d. *Journal of Molecular Biology*, *315*(3), 447–457. https://doi.org/10.1006/jmbi.2001.5242

Zhou, M.-M., Huang, B., Olejniczak, E. T., Meadows, R. P., Shuker, S. B., Miyazaki, M., Trüb, T., Shoelson, S. E., & Fesik, S. W. (1996). Structural basis for IL-4 receptor phosphopeptide recognition by thelRS-1 PTB domain. *Nature Structural & Molecular Biology*, *3*(4), 388–393. https://doi.org/10.1038/nsb0496-388

Zhou, M.-M., Ravichandran, K. S., Olejniczak, E. T., Petros, A. M., Meadows, R. P., Sattler, M., Harlan, J. E., Wade, W. S., Burakoff, S. J., & Fesik, S. W. (1995). Structure and ligand recognition of the phosphotyrosine binding domain of Shc. *Nature*, *378*(6557), 584–592. https://doi.org/10.1038/378584a0

Zweifel, M. E., & Barrick, D. (2001). Studies of the Ankyrin Repeats of the *Drosophila melanogaster* Notch Receptor. 2. Solution Stability and Cooperativity of Unfolding. *Biochemistry*, *40*(48), 14357–14367. https://doi.org/10.1021/bi011436+

CHAPTER 8: APPENDICES

8.1 Appendix A – Amino acid sequences for studied proteins

8.1.1 AIDA1b

10	20	30	40	50
MGSGTIDKIM	SSIDVGINNE	LKEMNGETTR	PRCPVQTVGQ	WLESIGLPQY
60	70	80	90	100
ENHLMANGFD	NVQFMGSNVM	EDQDLLEIGI	LNSGHRQRIL	QAIQLLPKMR
110	120	130	140	150
PIGHDGYHPT	SVAEWLDSIE	LGDYTKAFLI	NGYTSMDLLK	KIWEVELINV
160	170	180	190	200
LKINLIGHRK	RILASLGDRL	HDDPPQKPPR	SITLREPSGN	HTPPQLSPSL
210	220	230	240	250
SQSTYTTGGS	LDVPHIIMQG	DARRRRNENY	FDDIPRSKLE	RQMAQTGDWG
260	270	280	290	300
EPSITLRPPN	EATASTPVQY	WQHHPEKLIF	QSCDYKAFYL	GSMLIKELRG
310	320	330	340	350
TESTQDACAK	MRANCQKSTE	QMKKVPTIIL	SVSYKGVKFI	DATNKNIIAE
360	370	380	390	400
HEIRNISCAA	QDPEDLSTFA	YITKDLKSNH	HYCHVFTAFD	VNLAYEIILT
410				
LGQAFEVAYQ	LALQARKLE			

Number of amino acids: 419
Molecular weight: 47350.92 Da
pI: 6.17

8.1.2 Δ14AIDA1b

10	20	30	40	50
GSGTPRCPV	QTVGQWLESI	GLPQYENHLM	ANGFDNVQFM	GSNVMEDQDL
60	70	80	90	100
LEIGILNSGH	RQRILQAIQL	LPKMRPIGHD	GYHPTSVAEW	LDSIELGDYT
110	120	130	140	150
KAFLINGYTS	MDLLKKIWEV	ELINVLKINL	IGHRKRILAS	LGDRLHDDPP
160	170	180	190	200
QKPPRSITLR	EPSGNHTPPQ	LSPSLSQSTY	TTGGSLDVPH	IIMQGDARRR
210	220	230	240	250
RNENYFDDIP	RSKLERQMAQ	TGDWGEPSIT	LRPPNEATAS	TPVQYWQHHP
260	270	280	290	300
EKLIFQSCDY	KAFYLGSMLI	KELRGTESTQ	DACAKMRANC	QKSTEQMKKV
310	320	330	340	350
PTIILSVSYK	GVKFIDATNK	NIIAEHEIRN	ISCAAQDPED	LSTFAYITKD
360	370	380	390	
LKSNHHYCHV	FTAFDVNLAY	EIILTLGQAF	EVAYQLALQA	RKLE

Number of amino acids: 394
Molecular weight: 44560.77 Da
pI: 6.40

8.1.3 PTB5M

10	20	30	40	50
MSTPVQAAQH	HPEKLIAQSC	DYKAFYLGSM	LIKELRGTES	TQDACAKMRA
60	70	80	90	100
NCQKSTEQMK	KVPTIILSVS	AKGVKFIDAT	NKNIIAEHEI	RNISCAAQDP
110	120	130	140	150
EDLSTFAYIT	KDLKSNHHYC	HVFTAFDVNL	AYEIILTLGQ	AFEVAYQLAL
QARKLE				

Number of amino acids: 156
Molecular weight: 17469.08Da
pI: 7.00

8.1.4 Ubiqutin-APP36

10	20	30	40	50
MAWSHPQFEK	GGGSGGGSGG	SAWSHPQFEK	MQIFVKTLTG	KTITLEVEPS
60	70	80	90	100
DTIENVKAKI	QDKEGIPPDQ	QRLIFAGKQL	EDGRTLSDYN	IQKESTLHLV
110	120	130	140	
LRLRGLVPRG	SLEDAAVTPE	ERHLSKMQQN	GYENPTYKFF	EQMQNRS

Number of amino acids: 147
Molecular weight: 16488.53 Da
pI: 6.43

8.1.5 GST-APP

10	20	30	40	50
MSPILGYWKI	KGLVQPTRLL	LEYLEEKYEE	HLYERDEGDK	WRNKKFELGL
60	70	80	90	100
EFPNLPYYID	GDVKLTQSMA	IIRYIADKHN	MLGGCPKERA	EISMLEGAVL
110	120	130	140	150
DIRYGVSRIA	YSKDFETLKV	DFLSKLPEML	KMFEDRLCHK	TYLNGDHVTH
160	170	180	190	200
PDFMLYDALD	VVLYMDPMCL	DAFPKLVCFK	KRIEAIPQID	KYLKSSKYIA
210	220	230	240	250
WPLQGWQATF	GGGDHPPKSD	MLEDAAVTPE	ERHLSKMQQN	GYENPTYKFF
EQMQNRS				

Number of amino acids: 257
Molecular weight: 30131.76 Da
pI: 5.71